Calculating 3D intramyocardial strain tensors in a single slice of myocardium using MRI

Prepared by:
Aaron Hess
Submitted to the University of Cape Town in partial fulfilment of the requirement for the degree of Master of Science in Medicine, in Biomedical Engineering.

Supervisor:
Dr E. Meintjes
Department of Human Biology
MRC/UCT Medical Imaging Research unit
University of Cape Town

Date: March 14, 2006

Acknowledgements

This project would not have been possible without the expertise, experience and support from several people. Their constant assistance and guidance has been priceless towards the process and completion of this project.

First and foremost, a big thank you goes to the supervisor of this project, Dr Ernesta Meintjes who provided many hours of academic expertise and support.

Bruce Spottiswoode, for providing guidance, experience and software tools for the project (such as CineDENSEanalysis3D).

Prof. Frederick Epstein, of the Radiology and Biomedical Engineering departments at the University of Virginia, for his expertise and support of this project.

Xiaodong Zhong, of the University of Virginia, for providing support and input in the sequence development aspects of the project.

Furthermore, the following organisations enabled the completion of this project and are hereby acknowledged:

The University of Virginia (USA) departments of Radiology and Biomedical Engineering, for providing the cine-DENSE sequence source code. The universities ready access and provision of resources such as the MRI scanners. (This was funded in part from their NIBIB grant RO1 EB 001763).

The University of Cape Town, department of Human Biology, for providing subsistence funding that financially aided full time work on this project and who provided a motivating academic environment.

The Division for Postgraduate Funding of the UCT University Research Committee, for firstly providing financial aid that enabled the visit to the University of Virginia (USA) which significantly contributed towards this project and secondly for financial assistance through a research associate merit award.

Abstract

Strain is a measure of cardiac deformation and provides information on the mechanical and functional properties of the heart. As this deformation occurs in three dimensions (3D), a 3D measure of strain is appropriate, however, currently the procedures for measuring 3D intramyocardial strain fields are limited to a handful of techniques. The only widely accepted method being the use of tagging in orthogonal image planes that requires the imaging of the entire myocardial volume, followed by lengthy and time consuming post processing. A method to combine cine displacement encoding with stimulated echoes (cine-DENSE) and cine strain encoded MRI (cine-SENC) for the formulation of the complete 3D strain tensor field for a single slice of myocardium is proposed. The method entails cine-DENSE acquisitions of two adjacent 8mm slices of myocardium, repeated for encodings applied in each of two orthogonal in plane directions, followed by a cine-SENC acquisition with a 16mm slice thickness encompassing both the cine-DENSE image planes. The cine-SENC acquisition provides a measure of through plane tag deformation. This technique yields a full 3D strain tensor field for a single plane of myocardium in five breathholds, one for each of the four cine-DENSE acquisitions and one for cine-SENC.

Simulations of this technique were performed to quantify the RMS error introduced into the strain tensor by myocardial position variability between breathholds and noise in the kinematic measurements obtained from both the cine-DENSE and cine-SENC images. These simulations demonstrate that the kinematic measurement error has the largest effect with the radial strain having the largest RMS error of all the components. These simulations also demonstrate that the longitudinal component of the normal strain does not suffer from a significant error as a result of through plane myocardial position variability between breathholds.

A cine-DENSE sequence was modified to acquire cine-SENC data. This sequence was tuned through iterative scanning of a phantom and human subjects to find the optimal imaging parameters. The same scanner was used to acquire images of four healthy volunteers using the full combined cine-DENSE and cine-SENC protocol. The 3D intramyocardial strain tensor fields were calculated for the imaged slices and visualised. Four different visualisation techniques were implemented and demonstrated. These were (i) colour maps to demonstrate each component of the tensor field over time, (ii) images depicting the three principal strain magnitudes and directions,

(iii) a new technique of visualising the deformation via deforming cubes, and (iv) the entire strain tensor and tensor field was visualized on images depicting fields of superquadratic glyphs.

The 3D strain fields correlate well with those previously reported with exception of the average end systolic longitudinal and radial normal strains being slightly lower than those reported in the literature. The radial strain has the greatest end systolic standard deviation, demonstrating the large error in this component, whereas the circumferential and longitudinal normal strain have end systolic standard deviations of only 7% and 3% strain, respectively.

Two other strain measurement techniques were investigated for the calculation of 2D and 3D strain using fields of myocardial Lagrangian motion trajectories calculated from cine-DENSE data. These techniques provide the ability to calculate the strain at any desired time point within the imaging window and display this result on a Lagrangian map of myocardium (the first cine frame). The 3D strain was calculated using two adjacent planes of 3D cine-DENSE motion trajectories. Longitudinal strain results are inaccurate primarily as a result of the small, 2.8mm, separation between the two imaging planes. The 2D strain was calculated using both 2D and 3D trajectories of motion, demonstrating that the extra accuracy afforded by 3D data results in a reduction in negative strain values and an increase in positive strain values.

Contents

List of Figures

List of Tables

Chapter 1

Introduction

1.1 Introduction

Strain quantifies myocardial deformation, providing a measure of myocardial function. Due to the vast array of cardiac pathology that affect the myocardium this information is invaluable. Seventeen percent of deaths in South Africa result from cardiovascular disease (A study of the year 2000 by Bradshaw *et al* 2003). Strain illuminates myocardial functional properties such as myofiber orientation, electronic activation pathways and the amount and directions of contraction. The aim of this project was to develop and demonstrate a method for calculating an intramural three dimensional (3D) strain tensor field for a single slice of myocardium. The calculation of true 3D strain is not a commonly performed task, typically requiring the registration of multiple imaging planes spanning the entire myocardial volume. Simplified 1D and 2D measures are less problematic and more common place. 3D strain is, however, required to fully quantify the three dimensional nature of myocardial deformation.

This is achieved for a 16mm slice using a combination of two MRI kinematic measurement techniques: displacement encoding with stimulated echoes (DENSE) and strain encoded (SENC) MRI. The proposed method acquires cine-DENSE images with encoding applied in each of two orthogonal in plane directions for each of two adjacent 8mm slices. A cine-SENC acquisition encompassing these two image planes measures the deformation of tag planes which are applied parallel to the image.

The first step was to investigate the feasibility of this method with regard

to kinematic measurement noise and the variability of myocardial position over multiple imaging breathholds by performing a series of mathematical simulations. Following this a cine-DENSE imaging sequence was adapted to achieve cine-SENC capability. Post processing software was developed and used to validate this technique in healthy volunteers.

This first chapter introduces the location and anatomy of the heart to provide insight into the cardiac imaging paradigm. Theories of Lagrangian and Eulerian strain calculation are presented and techniques available for visualising fields of such measures in the myocardium are examined. A review of current non-invasive myocardial kinematic measurement techniques is given as well as an overview of myocardial 3D strain patterns reported in two previous MRI studies that used tagging methodology.

The second chapter presents background MRI theory, introduces k-space, MRI image formation, and the considerations and techniques that are required in MRI cardiac imaging. The theory of MRI tagging, cine-DENSE, and cine-SENC are described and the chapter concludes with the theory of strain field visualisation using superquadratic glyphs.

The experimental apparatus and techniques are described in chapter three. Information is first provided on the MRI scanner used and study subjects. The cine-DENSE MRI sequence and how it was adapted to perform SENC measurements is presented next, giving details of the sequence development environment. Tuning of the cine-SENC sequence and choosing appropriate parameters is described, leading to a description of the imaging protocol used to determine 3D strain in human subjects. The methods used for image processing and strain calculation using the proposed technique is presented as well as two methods of calculating two dimensional (2D) and 3D strain using cine-DENSE motion trajectories. Following the strain calculation descriptions a series of simulations are presented for the quantification of errors introduced into the strain tensor. The chapter concludes with a description of the techniques used for visualising the 3D strain tensor fields for a single slice of myocardium.

The results obtained from these experiments are described in chapter four starting with the results of the the cine-SENC tuning process for both the phantom and human subjects, highlighting the appropriate cine-SENC imaging parameters. The results of the 3D Lagrangian strain calculation for a 16mm slice of myocardium in four volunteers are presented, demonstrating the four different strain visualisation techniques, namely colour maps,

principal strain maps, deforming cubes, and superquadratic glyphs. The results obtained using cine-DENSE motion trajectories to compute 2D and 3D Lagrangian strain fields are presented next. The chapter concludes with the results of the error quantification simulations.

The results are discussed in chapter five, with discussions of the error simulations performed, the two kinematic measurement techniques with emphasis on the cine-SENC method, a discussion of the strain calculation and display methods, including the 2D and 3D strain computed from cine-DENSE motion trajectories. Some conclusions are presented in chapter seven.

1.2 Anatomy of the Heart

Acting as a continuous pump, the four-chambered, muscular heart is situated in the thoracic cavity. It is bounded laterally by the lungs, anteriorly by the sternum and caudally by the diaphragm. The heart is surrounded by a tough, fibrous bag called the pericardium. This prevents overdistension of the heart and anchors the heart in position, being itself attached to the sternum and the diaphragm. Between the fibrous pericardium and the heart itself is a potential space called the pericardial cavity. The heart wall is made up of three layers: the epicardium that acts as a sac holding the heart suspended in a watery lubricant; the myocardium is the heart muscle responsible for the pumping action of the heart; and the endocardium, which is continuous with the endothelial lining of the entire circulatory system.

The four chambers of the heart are the left and right atria and the left and right ventricles. The atria collect blood through the cardiac cycle and pass it into the ventricles. The left ventricle (LV), which provides the greatest pumping force, pumps blood through the entire body (systemic circulation). As a result this chamber has the thickest myocardium and hence the thickest wall. The functioning of the left ventricle is most vital to human survival due to the fact that it is solely responsible for pumping blood the greatest distance around the body and as such the LV is the structure that is most commonly studied in diagnostic imaging of the heart.

The left ventricle is situated predominantly on the left side of the thoracic cavity with its cone shaped apex pointing down and to the left. The majority of the great vessels enter at the base of the heart, which is superior to the left ventricle. The position of the heart in the chest cavity is illustrated in

Figure 1.1. The left ventricular myocardium consists of muscle fibres which, upon electrical stimulation, contract, resulting in myocardial wall shortening parallel to the wall; and thickening perpendicular to the wall. This pumping action maintains a continuous cycle of contraction and relaxation. The time of contraction is called systole and relaxation is termed diastole.

In cardiac imaging, the imaged views of the heart predominantly relate to the heart's own axis, which is the axis that runs from the apex of the heart to the base, the long axis. The first common view is a short axis view, which is a slice perpendicular to the long axis cutting through both the left and right ventricles, with the left ventricle forming a closed circle. In a long axis view the left ventricle is imaged along the long axis with the ventricular myocardium forming a 'u' shape. These views are shown in Figure 1.2.

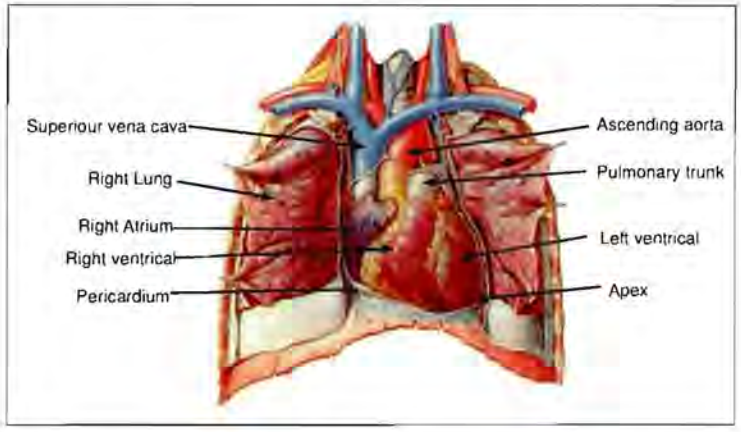

Figure 1.1: Anterior view of the heart in situe: note the pericardium has been removed to show heart surface features: Adapted from Netter (1998).

1.3 Strain Theory

When the myocardium contracts, it shortens along the muscle fibre directions and expands perpendicular to the same. Therefore a useful measure of myocardial function is the amount of shortening and expanding in these mentioned directions. Three-dimensional (3D) strain is ideal to fully quantify this action of the heart as it provides a measure independent of myocardial displacement and rotation by providing a means of calculating the principal directions of contraction and expansion.

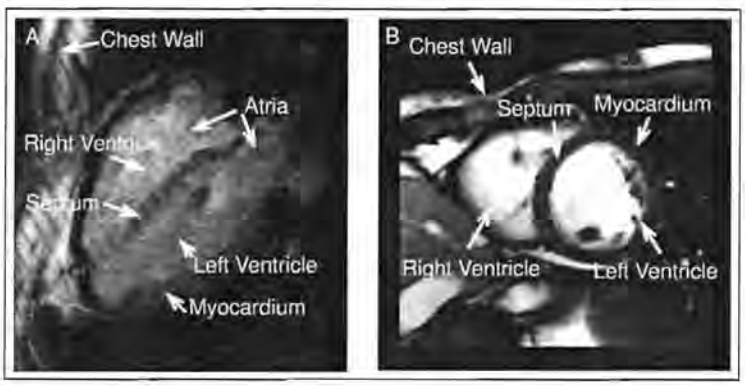

Figure 1.2: MRI images, demonstrating typical cardiac imaging views A) Long axis view of heart, B) Short axis view of the heart.

1.3.1 Calculation of strain

Strain is a measure of contraction or expansion at a point in time of a material relative to that material's state at another point in time. A Lagrangian approach is conventional in myocardial kinematics, which measures the deformation of the heart muscle relative to its state at end diastole. If one was to measure the deformation of a material relative to its current deformed state it would be called Eulerian strain.

The deformation gradient, F, of a unit of material expresses the shape of this material post deformation and is derived simply from the deformation of three non-coplanar vectors. If $\mathbf{V}_1$, $\mathbf{V}_2$ and $\mathbf{V}_3$ are three non-coplanar column vectors before deformation, and $\mathbf{V}'_1$, $\mathbf{V}'_2$ and $\mathbf{V}'_3$, are these same vectors post deformation, then the Lagrangian deformation gradient F is given by Equation 1.1 where / represents matrix multiplication by the inverse of the matrix following it.

$$F = [\mathbf{V}'_1 \quad \mathbf{V}'_2 \quad \mathbf{V}'_3]/[\mathbf{V}_1 \quad \mathbf{V}_2 \quad \mathbf{V}_3] \tag{1.1}$$

The above expression yields a 3 by 3 matrix that will map any vector in the material experiencing the same deformation to its orientation and magnitude post deformation. The Eulerian deformation gradient is the inverse of the Lagrangian deformation gradient tensor given above.

Lagrangian and Eulerian strain are usually calculated (in cardiac MR) from

the deformation gradient tensor using the following two equations, respectively:

$$E_L = \frac{1}{2}(F^T F - I) \tag{1.2}$$

$$E_E = \frac{1}{2}(I - F_{inv}^T F_{inv}) \tag{1.3}$$

in which F_{inv} is the matrix inverse of F (Eulerian form of F), F^T is the matrix transpose of F, and I is the 3 by 3 identity matrix. The strain tensor E is a symmetric 3 by 3 matrix. The tensor $F^T F$ is known as Green's deformation tensor and its diagonal elements represent the magnitude squared, in its deformed state, of a unit vector that is initially aligned with a coordinate axis in the reference state. The non-diagonal components of Green's deformation tensor are the dot product of unit vectors from different axes when they are deformed and thus provide a measure of the non-axial or shear strains.

As this method produces a squared magnitude result, it is sometimes convenient to express the normal strains in terms of percent length change, which is given in the following Equation (1.4)

$$E_{i,Lin} = \sqrt{2E_i + 1} - 1 \tag{1.4}$$

where E_i is the i^{th} normal strain.

Strain may also be defined as a change in length per unit length along a specified axis and is given by Equations 1.5 and 1.6,

$$E_{ij} = \frac{1}{2}(\frac{\delta u_i}{\delta X_j} + \frac{\delta u_j}{\delta X_i}) \tag{1.5}$$

where $i, j = 1$, 2 or 3; u_1, u_2, and u_3 are displacements along orthogonal axes X_1, X_2, and X_3 , respectively. The above formula yields normal strains when $i = j$. This formula for strain is known as a small deformation approximation and can also be written as follows (Equation 1.6):

$$E_L = F - I \tag{1.6}$$

In cardiac MRI the strain tensor is usually aligned to a local coordinate system (Augenstein and Young 2001, and Moore *et al* 2000). The axes of this coordinate system are defined as the radial direction (from epicardium to endocardium), the circumferential direction around the LV circumference in a short axis image of the heart, and the longitudinal direction (aligned, following the myocardium from the apex towards the base). E is mapped to this coordinate system using a rotation matrix R in the following manner:

$$E_{RCL} = RER^T \tag{1.7}$$

Finally, as E is symmetric it can be decomposed into its principal magnitudes and directions, called principal strains. The principal strain directions are defined as the three mutually orthogonal axes where no shear strain would occur. Principal strain magnitudes are calculated using the eigenvalues of E and the principal strain directions are calculated from the eigenvectors of E.

1.3.2 Strain verses strain rate

As some imaging modalities measure velocities as opposed to displacement, it is important to distinguish between strain and strain rate. Strain rate is the time derivative of strain and can be calculated from velocity. Strain rate gives an instantaneous measure of deformation and, if measured at high temporal resolution, will highlight short-lived deformation phenomena. Strain can be calculated from strain rate using a time integral, but caution must be exercised to ensure that the integration occurs over the same tissue. A more common approach to calculating strain from velocity data is to compute displacement trajectories by integrating the velocity fields as done by Zhu *et al* (1997). Strain can then be calculated in the usual manner using displacement measurement techniques.

1.3.3 Considerations when measuring intramyocardial strain

In all non-invasive kinematic imaging modalities a series of images are normally acquired, providing kinematic data about different axes of deformation. As the heart is moving continuously both due to the cardiac cycle and breathing, it is important to consider that the series of images taken at different times may not be of the exact same tissue. This may not have serious

implications for displacement or velocity measures, but in strain measures a misalignment of one or two mm's can have a drastic effect.

When measuring 3D strain, this problem is confounded further as true 3D strain requires the deformation of four non-coplanar points to be fully formulated (i.e. one cannot use points from the same imaging plane). There are two ways to approach this problem: the first is to co-register the images, thus ensuring that the same portions of myocardium line up. This becomes a very complicated procedure when imaging 3D strain as the entire myocardial volume has to be imaged in order to accurately co-register the data. However this is a trivial task when measuring 2D strain, as only 2D co-registration is required.

The alternate method to overcome this problem is to acquire the different images in parallel, as done by Reese *et al* (2002) who acquired two adjacent image planes simultaneously for phase contrast velocity encoded data and stimulated echo displacement encoded data, respectively. This method ensures that the data is aligned correctly as data for two adjacent planes is acquired at the same time, thus ensuring no cardiac movement between the image acquisitions.

1.4 Literature Review

1.4.1 3D Intramyocardial strain patterns in healthy and diseased myocardium

Knowledge of the expected variations in myocardial strain is of key importance in the diagnosis of cardiac disease. Croisille *et al* (1999) reported the use of strain measures to identify regions of viable and non-viable tissue in ischemia. In left ventricular hypertrophy strains are reduced by up to 40% and characteristic strain patterns are associated with cardiomyopathies (Richeck 2001).

Bogaert and Rademakers (2001) reported a high degree of regional non-uniformity for intramyocardial strains as measured using tagged MRI. Accurate strain measurements therefore require high spatial and temporal resolutions. Transmural strain variations have been reported with strains generally increasing from the epicardium towards the endocardium. The strain

also generally increases from the apex towards the base (Bogaert and Rademakers 2001, Moore *et al* 2000).

Moore *et al* (2000) calculated 3D strain based on tagged cardiac MRI images. When examining the strain circumferentially around the heart, they reported significant variation amongst the different segments of the heart. A mean circumferential strain of -0.24 was reported in the apical anterolateral region as compared to the inferoseptal region where a mean value of -0.16 was found. They found radial strain to be greatest apically, anteriorly and laterally but the longitudinal strain, however, was found to be homogenous in the circumferential direction.

Moore *et al* (2000) reported that the most positive principal strain is approximately radial, the most negative principal strain lies in the circumferential longitudinal direction forming a left-handed spiral from the apex to the base when viewed from the base, and that the second principal strain also lies in the circumferential longitudinal plane.

Variations in the timing of the intramyocardial strain patterns are also important not only when investigating the electrical conductivity of the heart, but also in other pathological states such as ischemia where post-systolic circumferential shortening has been reported (Hatle and Sutherland 2000). Zwanenburg *et al* (2004) reported timing variability in the healthy myocardium, most importantly, early onset and late peak shortening in the lateral wall.

1.4.2 Intramyocardial strain measurement techniques

Ultrasound and Magnetic Resonance Imaging (MRI) are the only two imaging modalities that can measure intramyocardial mechanics of the heart non-invasively. Both these techniques have been widely used in the measurement of intramyocardial strain.

Ultrasound, which is inexpensive, accessible and portable, measures tissue velocities using the Doppler Effect. This technique was first used to image myocardial wall motion in 1961 (Yoshida *et al*). Ultrasound produces either two- or three-dimensional (2D or 3D) images but is only able to measure velocities and strain rate in a single dimension down the ultrasound beam. Ultrasound can image at a rate of up to 300 frames per second, which far exceeds the temporal resolution achievable with MRI. Currently 3D displace-

ments cannot be measured with ultrasound, although ongoing research in speckle tracking (Voigt and Flachskampf 2004) may address this. Measuring 3D velocities with Doppler imaging is also complicated, as three sets of images (with the ultrasound beam oriented in three non-coplanar directions) need to be acquired and co-registered. Images produced with echocardiography suffer from a large amount of noise that introduces significant error into velocity measures.

Several studies have reported the use of ultrasound to measure strains in 3D (for example, Stoylen *et al* 2003, Edvardsen *et al* 2002). The most important limitation associated with this technique is that true 3D strains are not measured, but only single-dimensional strains in long axis and short axis images, respectively, giving rise to strain distortion if the angle to the tissue is not the same as the angle of the strain. Furthermore, for a high temporal resolution, limited spatial resolution is achieved such that transmural variations in strain can not be detected. Edvasdsen *et al* and Stylen *et al* both report the ability to identify infarcts.

Cardiac MRI has evolved since its inception in the early 1980's to an imaging modality that offers high anatomical clarity. Various MRI techniques have been applied to measure intramyocardial strain (typically in 2D or 1D measures), these are MRI tagging, harmonic phase MRI (HARP), displacement encoded MRI (DENSE), strain encoded MRI (SENC), and phase contrast (PC) imaging.

MRI tagging has become the gold standard in non-invasive strain measurements. The technique uses planes of hypomagnetization as markers to measure deformation and track the motion of the myocardium. This technique does not suffer from phase inhomogeneities as do other MRI techniques. Tagging inherently measures 2D strain and in order to image full 3D strain both short axis and long axis images must be acquired and co-registered over the entire volume of the heart. Tagging limits the achievable spatial resolution, since tag spacings greater than twice the pixel size are required in order that tags may be clearly identified at the given pixel resolution. Automatic detection of the tag lines is highly complex and often requires significant and time consuming user input, which is further complicated by tag fading.

Moore *et al* (2000) used tagged cardiac MRI images to compute 3D strain and presented an estimate of the accuracy of the technique as a function of temporal variability. The most negative principal strain was found to have

the highest accuracy (2.7% RMS variability about a cubic fit, given as a percentage of the peak cubic fit), while the radial strain and radial shear components had the greatest inaccuracy (up to 23% RMS variability about a cubic fit).

Myocardial tagging spatially modulates the image thus forming harmonic peaks at different frequencies when viewed in k-space (frequency space). Harmonic phase MRI (HARP) (Osman *et al* 2000) is essentially an image processing technique in which one harmonic peak is filtered out using a band pass filter resulting in a phase image that is modulated in the same pattern as the tag lines, Figure 1.3 demonstrates the post processing procedures.

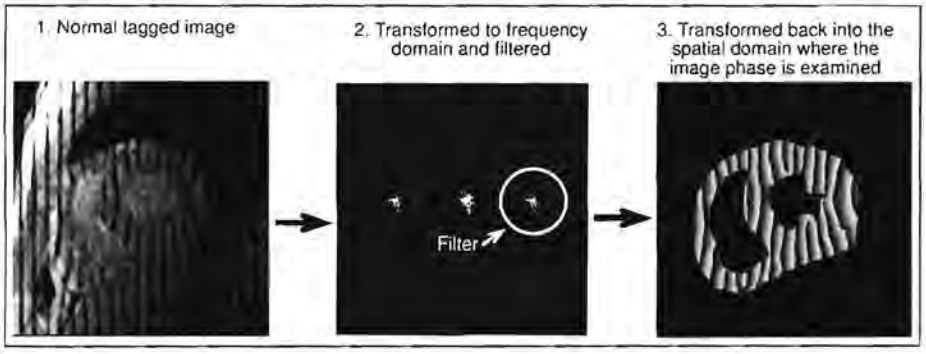

Figure 1.3: Demonstration of the HARP imaging process, images created by Bruce Spottiswoode.

Automated pseudo tag lines can now be superimposed on the image at either the original tag separation or a higher frequency. Pseudo tags are superimposed using the knowledge that within one tag cycle the resultant phase will change from $-\pi$ to π. The spatial gradient of phase provides a simple and straightforward calculation of one-dimensional (1D) strain. Sampath *et al* (2003) used HARP to calculate 2D cardiac strain and reported good circumferential strain results. Pan *et al* (2005) co-registered short axis and long axis HARP images to calculate full 3D strain and reported similar circumferential strain trends. As this technique is relatively new, extensive validation has not been performed. Sampath *et al* reported that phase inhomogeneities introduced error into the measurement and that the accuracy of the technique diminished over time due to tag fading. Although this technique boasts rapid processing times, the application of a band pass filter results in a spatial resolution lower than the image pixel resolution (Kim *et al* 2004, Parthasarathy and Prince 2004). Displacement encoding

with stimulated echoes (DENSE), first reported by Reese *et al* in 1996, avoids the use of a band pass filter in isolating the harmonic peak and provides greater flexibility in computing displacements.

DENSE (Aletras *et al* 1999a, Reese *et al* 1996) encodes the displacement of the tissue onto the phase of the image. This results in the quantification of displacement for each image pixel allowing high resolution kinematic data. The displacement encoding is done in the image acquisition sequence as opposed to post-processing as in HARP. The only report on using DENSE to calculate 3D strain is by Reese *et al* (2002), where two adjacent slices were imaged in parallel. The authors don't give an indication of the errors introduced into the strain calculation. Kim *et al* (2004) reported high spatial resolution (2.7mm by 2.7mm) with a temporal resolution of 60ms in their 2D strain calculations using DENSE. Their results are consistent with those reported by Moore *et al* (2000) with achieved strain resolutions sufficient to observe transmural variations. Aletras *et al* (1999b) reported less than 3% error in myocardial strain measurements using DENSE. One disadvantage of DENSE is that only one encoding direction can be acquired in one heart beat thus requiring longer acquisition times than low temporal resolution PC MRI.

Although DENSE is able to accurately measure three-dimensional displacements, measuring through plane strain requires DENSE data of two consecutive image planes. Calculating strain in this manner is no trivial task. Strain encoded (SENC) MRI, first proposed by Osman *et al* (2001), measures through plane strain without the need to acquire two consecutive image planes. SENC is unique amongst the kinematic measurement sequences as it uses the image magnitude to estimate the through plane strain by applying tag planes parallel to the imaging plane. Garot *et al* (2004) showed that the longitudinal strain measured using SENC at a high spatial resolution (1.5 by 2.5mm) correlated well with that obtained with 3D tagging. They reported longitudinal strain findings in patients with myocardial infarction consistent with those reported in the literature.

One limitation of SENC is that it only provides a 1D strain measure (measured from the tag frequency and spatial gradient of phase), so that a full 3D strain tensor cannot be formulated by extending a 2D strain imaging technique to incorporate SENC. Furthermore, *a priori* knowledge of the expected strain is required to ensure that saturation does not occur. The primary advantage of this technique is that the post processing is fast and simple.

The only MRI kinematic measurement technique that does not use tagging is phase contrast (PC) velocity encoding (Nayler *et al* 1986). PC encodes the tissue velocity onto tissue phase using a bipolar gradient. This technique measures three-dimensional velocity by obtaining three orthogonally encoded images. Zhu *et al* (1997) presented a method based on velocity maps to measure intramyocardial 2D strain. The authors propose that the method is capable of obtaining strain measures of high accuracy, but they caution that the technique is currently limited to 2D strain, as 3D strain would require imaging the entire myocardial volume.

Since PC imaging does not use tagging, it does not suffer from tag fading as do all of the other MRI sequences mentioned. As such, an entire cardiac cycle can be imaged with all images of the same quality. The technique also yields a high spatial resolution with velocity measures at a voxel resolution. However, since PC imaging does not inherently measure displacement, a strain rate is computed. Strain rate is most useful when images are acquired at a high temporal resolution, which is not the case in MRI.

The current project aims to combine SENC and DENSE MRI to develop a technique that is clinically feasible to measure true high resolution 3D intramyocardial strain with reasonable processing times and acceptable accuracies.

1.4.3 Strain tensor visualization

When investigating pathology using strain quantification, it is of key importance to clearly and simply visualise this complex 3D measure. The strain tensor consists of six independent measures which can be expressed as either three normal strains with three shear components or as three eigenvalues and three eigenvectors (principal strains). It is desirable to view all of this information in a manner that allows one to observe the interaction of all the strain components. Wunsche *et al* (2004) suggest a few suitable techniques in their recent review article.

The simplest manner of visualising the strain tensor in the myocardium is to display each of the six components on separate colour maps. In this case it is crucial that the strain tensor is aligned to the natural coordinate system (radial, circumferential and longitudinal axes). The primary disadvantage of this method is that all the data is disjoint with the shear strain not providing much useful information. An alternate approach is to visualise each of the

three principal strains on a separate colour map and overlay, on each image, the vectors defining the directions of the principal strains.

A method that attempts to visualise all the components of the tensor in one image involves encoding the strain components onto an icon, called a glyph. One commonly used glyph is a simple ellipsoid, where the axes of the ellipsoid are defined by the eigenvectors and the length of the axis is related to the eigenvalues. For instance, if all three eigenvalues were equal, a sphere would be displayed. This concept was developed further by Ennis *et al* (2005) who give an indication of the similarity between the eigenvalues with the roundness of the glyph along that particular axis. Again this method produces a sphere when all eigenvalues are the same, but when the first is greater, for instance, than the second and third that are still equal,the glyph becomes prolate. When the first and second are equal but greater than the third, the glyph becomes oblate. The glyph therefore becomes very circular in the plane that encompasses two eigenvectors with two similar eigenvalues. The advantage of this second glyph technique is that it highlights the differences between the eigenvalues more than the simple ellipsoid while still displaying the vector directions. With these glyph techniques the magnitude and sign of only one principal strain can be encoded onto the colour of the glyph thus leaving the sign of the other two unresolved. The main problem with glyph techniques is that they suffer from visual cluttering, particularly when there are a large number of sample points.

When the entire volume of myocardium is imaged, the strain data can be displayed using information about the principal strain vector fields. Streamlines is one such technique that attempts to give a continuous representation of the vector field of one principal strain. A path is followed by the streamline through the vector field and displayed by a curving cylinder with the colour representing the magnitude of the principal strain. Hyperstreamlines encode the other two principal strains onto the roundness of the cylinder in a similar manner to the ellipsoid glyphs mentioned above. The last technique is called a Line Integral Convolution (LIC). This approach textures a surface to depict the direction of one principal strain vector with the magnitude depicted by image colour or texture.

Chapter 2

Theory

2.1 Magnetic resonance imaging theory

2.1.1 The MRI signal - classical description

Nuclear Magnetic Resonance (NMR), of which the first signals were detected late in 1945, forms the basis for nuclear magnetic resonance imaging. The name NMR imaging has been shortened in the medical field simply to Magnetic Resonance Imaging (MRI) due to the unfavourable connotations with nuclear radiation.

NMR relies on the fact that atoms with an odd number of protons and/or neutrons in the nucleus exhibit a non-zero nuclear spin angular momentum, $\boldsymbol{I}$. These nuclear spins act as magnetic dipole moments, $\boldsymbol{\mu}$, that are originally oriented randomly. When these atoms are placed in an external magnetic field, $\mathbf{B_0}$, (typically 1.5T or 3T in medical applications), they will interact with it according to the nuclear Zeeman interaction

$$H = -\boldsymbol{\mu} \cdot \mathbf{B_0} \tag{2.1}$$

The effect of this interaction is to cause the magnetic dipole moments to precess about $\mathbf{B_0}$ at a resonant frequency ω_L, termed the Larmor precession frequency, given by:

$$\omega_L = \gamma B_0 \tag{2.2}$$

in which γ is the gyromagnetic ratio. Typically, $\mathbf{B_0}$) is applied in the z-direction, called the longitudinal direction. The net effect of all these millions of precessing dipole moments is a net magnetization, $\boldsymbol{M}$, parallel to the applied field $\mathbf{B_0}$.

In the human body the most prevalent atom is hydrogen (H), of which the nucleus is also termed a proton. Both due to its high biological abundance of 63% and natural abundance of 99.985%, this is the nucleus most commonly imaged with MRI. In a magnetic field of 1.5T, the resonance frequency of ^{1}H is 63.86MHz.

The NMR phenomenon occurs when the nuclei in a large static magnetic field, $\mathbf{B_0}$, are exposed for a time t to a time-dependent oscillating radiofrequency (rf) field, $\mathbf{B_{rf}}$, of the form

$$\mathbf{B_{rf}} = 2\mathbf{B_1}cos(\omega t) \tag{2.3}$$

that is applied perpendicular to $\mathbf{B_0}$ at a frequency ω equal to their Larmor precession frequency. This oscillating field $\mathbf{B_{rf}}$ can be decomposed into two counter rotating magnetic fields each with magnitude B_1, where one rotates clockwise about $\mathbf{B_0}$ with frequency ω and the other counter clockwise with the same frequency. If $\mathbf{B_1} << \mathbf{B_0}$, as is generally the case, the effect of a rotating magnetic field on a magnetic moment is negligible unless its frequency of rotation is of the order of the Larmor frequency, ω_L. The component of $\mathbf{B}_{rf}$ that rotates in a direction opposite to that of the precessing dipole moments will therefore have no effect so that $\mathbf{B}_{rf}$ can be thought of as being comprised simply of a magnetic field $\mathbf{B_1}$ that is perpendicular to $\mathbf{B_0}$ and rotating about it in the same direction and with a frequency equal to that of the precessing magnetic dipole moments.

Transforming to coordinates ijk rotating with the same frequency as $\mathbf{B_1}$, causes the magnetic dipole moments to precess in the rotating reference frame about an effective magnetic field $\mathbf{B_{eff}}$ given by

$$\mathbf{B_{eff}} = (\mathbf{B_0} - \frac{\omega}{\gamma})\vec{k} + \mathbf{B_1}\vec{i} \tag{2.4}$$

in which the axis of rotation $\vec{k}$ points along the static external magnetic field, $\mathbf{B_0}$, and the unit vector $\vec{i}$ in the rotating reference frame is chosen along $\mathbf{B_1}$. In the stationary reference frame this results in a tipping of

the net magnetization $\boldsymbol{M}$ from the longitudinal axis towards the transverse (i, j) plane through a spiralling motion. After the rf pulse is switched off, the magnetization continues to precess about the longitudinal axis at the Larmor frequency.

The duration of the rf pulse determines the flip angle. The 90- and 180-degree pulses, respectively, are defined as the times for which $\mathbf{B_1}$ must be applied in order to rotate the magnetization through 90° or 180°, and are given by

$$t_{\frac{\pi}{2}} = \frac{\pi}{2\gamma B_1}$$

and

$$t_{\pi} = \frac{\pi}{\gamma B_1} \tag{2.5}$$

After the application of a 90° pulse, the magnetization is entirely in the transverse plane, whereas a 180° pulse will result in an $\boldsymbol{M}$ anti-parallel to the external magnetic field.

Since the magnetization continues to precess about $\mathbf{B_0}$ at the Larmor precession frequency, after application of the rf pulse, an emf will be induced in a receiver coil according to Faraday's law. This emf is the MRI signal. The magnetization loses its phase coherence over time due to the fact that the local magnetic field experienced by each individual magnetic moment is slightly different due to different neighbouring elements causing each moment to precess at a slightly different Larmor precession frequency. This dephasing results in an exponentially decaying MRI signal termed the Free Induction Decay (FID). In addition, the magnetization returns over time to its equilibrium value parallel to the external magnetic field. This process is called T1- or longitudinal relaxation. The time constant T2 refers to the time when the MRI signal has decayed by 63% due to dephasing, and T1 is defined as the time when the longitudinal magnetization has relaxed to 63% of its maximum value.

2.1.2 MRI Image Formation

Since the frequency of precession is a function of the magnetic field, small variations in the magnetic field can be used to spatially encode the MRI signal. This is achieved through the use of linear gradient fields. Three

mutually orthogonal gradients, termed the slice, frequency, and phase encoding gradients are turned on at different times during the pulse sequence to achieve spatial encoding to produce an MRI image.

The slice encoding gradient is applied perpendicular to the imaging slice during the rf pulse. This causes the resonance condition to be satisfied for only a small band of frequencies so that only nuclei in this band of tissue will be excited, i.e. flipped. The width of the imaging slice will depend on the strength of the gradient field as well as the bandwidth of the rf pulse.

Frequency encoding is applied in one of the in plane directions during signal acquisition causing the frequency of the signal to vary as a function of position along that axis. The frequencies in the signal are decomposed using a Fourier transform. Phase encoding is applied perpendicular to frequency encoding in the plane of the image after application of the rf pulse but before signal acquisition. The application of this gradient results in a linear variation in spin frequency for the duration of the gradient so that higher frequency spins acquire more phase than lower frequency spins. This process is repeated for n different phase encoding gradients for an image with matrix size m $\times$ n, where typically n $\leq$ m and achieves spatial encoding in the phase encoding direction. The phase - and frequency encoded data is decomposed using a 2D Fourier transform to produce an MRI image.

It should be noted that by using three linear gradient fields (in x y or z) a resultant linear gradient can be formed in any direction, so that MRI images can be acquired in any desired plane.

2.1.3 K-space

K-space refers to the raw digitised MRI signal data that, when Fourier transformed, produces the MR image. It is simply an array of numbers of which each row contains the digitised magnitude and phase values for the MRI signal for a single value of the phase encoding gradient. In normal 2D image acquisition no phase encoding is applied in the slice select direction (the X_3-axis), so that k_3 is zero and the k-space grid is two dimensional. Typically, each row corresponds to a repetition of the sequence for a different value of the phase encoding gradient. In 3D imaging, phase encoding is applied in the slice select direction also resulting in a 3D k-space grid. The order in which the k-space array is filled is intimately related to the pulse

sequence, since k is defined in terms of the gradient field $\mathbf{G}$ according to the expression

$$k_i = \gamma \int_0^t G_i(t')dt' \tag{2.6}$$

in which i assumes the values 1, 2, and 3, respectively.

K-space is a spatial frequency representation of the MRI image as demonstrated in Figure 2.1.

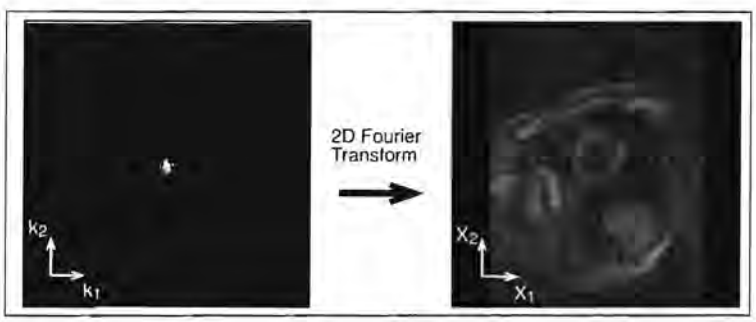

Figure 2.1: Example of k-space data and its associated image for a 2D acquisition A) k-space, B) MRI image.

2.1.4 Cardiac MRI

Traditional MR imaging requires several minutes to compose an image with good contrast and signal-to-noise ratio. This results from having to acquire data for multiple values of the phase encoding gradient in order to fill all the lines in k-space. In cardiac MR this introduces difficulties as the heart is constantly in motion both due to its rhythmic contractions and from breathing. Fast imaging techniques and ECG (Electro-CardioGram) gating have been introduced to address these problems and have succeeded in greatly reducing motion artefacts. Fast imaging techniques may be described firstly by the readout (frequency encoding) mechanism that they employ and secondly by the manner in which they excite the imaged tissue.

Increasing the speed of the readout mechanism involves acquiring large portions of k-space from a single tissue excitation (FID). Echo Planar Imaging (EPI) is one such sequence that increases the readout speed by acquiring

multiple lines of k-space from a single tissue excitation. This is done by applying a small phase encoding gradient at the end of each signal acquisition stage, and alternating negative and positive frequency encoding gradients during signal acquisition, which has the effect of filling multiple lines of k-space in a zig-zag fashion. Figure 2.2 is a typical EPI readout sequence demonstrating the alternating gradients to read multiple lines of k-space. The number of lines that can be acquired after a single excitation of the hydrogen nuclei is limited by the signal decay over time as well as the speed at which readout can occur. The latter also depends on the maximum gradients achievable and maximum readout bandwidth. To resolve this problem multiple lines of k-space are acquired over multiple excitations, this method is called segmented EPI and is demonstrated in Figure 2.3 where three segments are acquired.

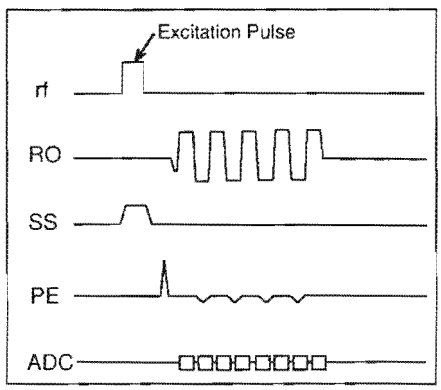

Figure 2.2: EPI sequence diagram. RO is the gradient in the readout direction, SS is the gradient in the slice select direction, PE is the gradient in the phase encode direction and ADC is the Analog to digital converter for the FID readout.

As an alternative to EPI, a spiral acquisition technique can be used which traverses k-space in a spiral by using linearly increasing sinusoidal gradients for both frequency and phase encoding that are 90 degrees out of phase. Both EPI and spiral acquisition readout mechanisms introduce artefacts due to the long readout times that experience T2 signal decay and off-resonance effects.

The manner in which the tissue is excited may also be modified to reduce the acquisition time. One mechanism of obtaining multiple echoes from one excitation is to use 180° refocusing rf pulses, which can be repeated several times without waiting for T1 relaxation. Alternatively, multiple excitations

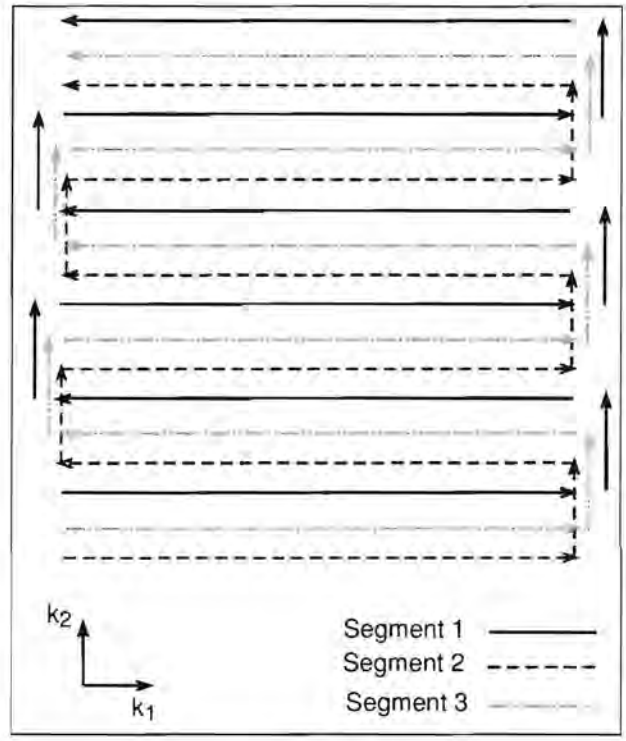

Figure 2.3: k-space trajectory for EPI readout demonstrating the trajectory for three segments from different rf excitations.

can be performed in a short space of time using small flip angles. Since many such excitations in a short period of time do not allow for full T1 recovery, a number of preparation pulses are applied prior to imaging to allow the signal magnitude to achieve a steady state. (Haacke *et al* 1999).

As mentioned previously, fast imaging is used to avoid artefacts introduced by the motion of the heart. Fast imaging alone is, however, not able to overcome these problems. Motion artefacts due to the cardiac cycle are further reduced by performing the imaging operations in multiple limited time frames. By using such windows in multiple cardiac cycles to acquire segments of k-space, a full MRI image can be composed where all the lines in k-space were acquired at the same stage in the cardiac cycle. This window is periodically triggered using an Electro-CardioGram (ECG) QRS wave.

Artefact introduced by the respiratory displacement of the heart is overcome either by breathhold acquisition or by using respiratory gating in the same

manner as ECG gating. Respiratory gating can be achieved using an MRI technique called a navigator echo, which excites a small band of tissue across the diaphragm. The signal from this band is used to measure the location of the diaphragm in order to correct for motion of the heart. All of the MRI sequences described in this thesis exploit the fast imaging techniques mentioned in this section.

2.2 MRI Tagging

In 1988 Zerhouni *et al* developed a technique to apply in vivo tag lines onto images of the heart (Figure 2.4). These tag lines deform with the myocardium allowing calculation of intramyocardial kinematic data. The kinematic imaging techniques used in this project are based on the effects of tagging on myocardial tissue.

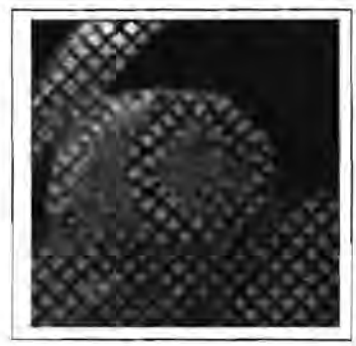

Figure 2.4: Example of tagged myocardium - short axis view.

The tag lines are applied using a tagging kernel which is typically applied at the start of the cardiac cycle; thus all kinematic data is computed relative to the position of the tissue at end diastole. The kernel is followed by a typical cardiac imaging sequence applied at the desired imaging time, which must be before tag fading has occurred. This is governed by the T1 relaxation time. One of the earliest and most popular tagging kernels is the Spatial Modulation of Magnetization (SPAMM) kernel (Axel and Dougherty 1989). A 1-1 SPAMM sequence consists of a 90° rf pulse that flips some of the spins into the transverse plane, followed by a gradient field that modulates the phase of the excited spins in the tagging direction (perpendicular to tag planes). A 90° pulse is then applied to rotate the components of the transverse spin that lie in the zero phase direction back to the longitudinal axis,

thus sinusoidaly modulating the longitudinal magnetization of the tissue.

A sinusoidal modulation pattern does not optimize tag contrast. For this reason higher order SPAMM techniques that add more rf pulses with magnitudes varied in a binomial pattern and with gradients applied between them are often used. Another popular kernel for improved tag contrast is the Delays Alternating with Nutations for tailored Excitations (DANTE) introduced by Mosher and Smith (1990).

One of the disadvantages of tagging is that the tag lines fade over the cardiac cycle due to T1 relaxation of the hypomagnetized tissue. For the 1-1 SPAMM sequence this has been addressed by a technique known as Complementary Spatial Modulation of Magnetization (CSPAMM, Fischer *et al* 1993). The procedure involves obtaining two sets of tagged images, the first obtained in the same manner as above and the second with a negated modulation pattern which suffers from the same tag fading resulting from T1 relaxation as the first. A subtraction of these two images doubles the amplitude variation of the tag pattern offering a substantial reduction in tag fading.

A couple of novel techniques to achieve myocardial kinematic measurements have evolved from MR tagging.

2.3 Displacement encoding with Stimulated Echoes - DENSE

Displacement encoding using stimulated echoes (DENSE) (Reese *et al* 1996, Aletras *et al* 1999a) encodes tissue displacement onto image phase in the same manner as phase contrast velocity encoding (PC) encodes velocity onto phase. By using the stimulated echo that results from the 1-1 SPAMM tagging sequence images can be acquired at any time before the modulation in longitudinal magnetization is lost due to T1 recovery of the hypomagnetized tissue. The encoding gradient in the 1-1 SPAMM kernel applies a uniform gradient of phase across the imaging volume in the encoding direction which, prior to measurement, is unwound using a second encoding gradient (unencoding) with a negated momentum that reverses the gradient of phase accrual across the image. The application of this pair of gradients results in zero phase accrual for tissue that experienced no displacement between application of the gradients. For tissues that moved between application

of the gradients the resulting phase change is proportional to displacement. The timing of the DENSE sequence is illustrated in Figure 2.5.

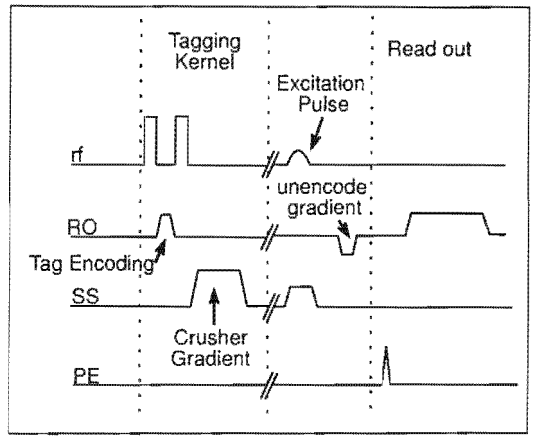

Figure 2.5: DENSE sequence diagram.

As in PC MRI, the displacement information is encoded in the phase image, such that phase inhomogeneities need to be corrected. This is accomplished in DENSE imaging with a phase reference scan whose phase is subtracted from the phase of the encoded image. This results in tissue with zero displacement having a zero phase.

Define image coordinates $\mathbf{x} = (x_1, x_2)$ and transverse magnetization, M_{ij}. The transverse magnetization after encoding in the x_1 direction is given by

$$\begin{aligned} M_{ij}(\mathbf{x}, t) = & \frac{M}{2} sin(\alpha) e^{-\frac{-t}{T1}} e^{-jke\Delta x_1} \\ & + \frac{M}{2} sin(\alpha) e^{-\frac{-t}{T1}} e^{-jke(\Delta x_1 + 2x_1)} \\ & + M_0 sin(\alpha)(1 - e^{\frac{-t}{T1}}) e^{-jke(\Delta x_1 + x_1)} \end{aligned} \tag{2.7}$$

in which α is the flip angle of the excitation pulse; M_0 is the thermal equilibrium value of longitudinal magnetization; Δx_1 is the tissue displacement that occurred in the x_1 direction between the tagging and measurement; and ke is the displacement encoding moment (in cycles per mm).

The first term in Equation 2.7 above describes the stimulated echo that has a phase directly proportional to displacement. The other two terms are, respectively, the complex conjugate echo and the T1 relaxation echo that

results from tag fading. The positions of these echoes in k-space and the effect of the unencoding gradient is demonstrated in Figure 2.6. These last two, artefact-generating echoes are suppressed to ensure that the stimulated echo only contributes to the image; this can be done using several different techniques.

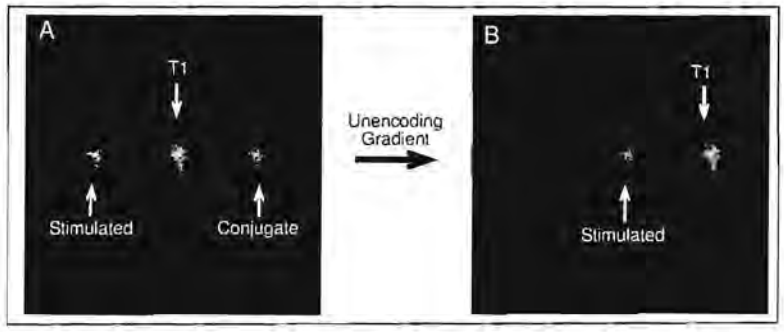

Figure 2.6: K-Space images demonstrating the DENSE sequence. A. Echoes after application of a 1-1 SPAMM tagging kernel. B. The echoes imaged after application of an unencoding gradient that effectively shifts the conjugate echo out of imaged k-space.

The complex conjugate echo is most commonly suppressed by using a large encoding gradient that results in this echo being shifted out of the imaged k-space during the unencoding process as demonstrated in Figure 2.6. There are two primary techniques used to suppress the T1 echo: the first uses a CSPAMM subtraction that doubles the magnitudes of the stimulated echo and complex conjugate echo and removes the T1 echo in the same manner as in tagging (Kim *et al* 2004). The second technique uses dephasing through the image plane (Aletras *et al* 1999b), which results in the T1 echo being shifted out of the imaged k-space in the k_3 direction (as only one k_3 plane is imaged in a 2D acquisition). This is achieved by applying a second encoding gradient in the slice select direction at the same time as the encoding and unencoding gradients. The displacement encoding that this introduces in the through plane direction is removed by applying these same through plane encodings to the phase reference image.

Another artefact-generating echo suppression technique that was proposed by Epstein and Gilson (2004) is called Cosine and Sine Modulation to Eliminate (CANSEL). The technique performs two CSPAMM acquisitions, one with a cosine modulation and one with a sine modulation. Each CSPAMM acquisition inherently removes the T1 echo, but as the complex conjugate

echo is negated in the sine acquisition, addition of these two CSPAMM images results in removal of the complex conjugate echo.

Although DENSE is able to accurately measure 3D displacement with high spatial resolution, through plane strain measurements would require data for two consecutive image planes. Strain encoded MRI (SENC) measures through plane strain directly.

2.4 Strain encoded MRI - SENC

Strain encoded MRI applies tag planes parallel to the imaging plane, as shown in Figure 2.7. Tagging effectively modulates the k-space image data onto two image peaks, in this case along the k_3 axis, one above and one below the centre of k-space. Strain causes a change in the tag frequency resulting in a shift of the k-space peaks. Conventional 2D imaging acquires data in the $k_1 - k_2$ plane, thus only sampling one k_3 value. In order to establish the location of these harmonic peaks, and hence the frequency of the tag planes, images must be acquired for a number of different k_3 encodings. SENC proposes a technique whereby just two images at two different k_3 encoding values are sufficient to estimate this peak. An estimate is formed using a centre of mass estimate of the two encodings. This estimate suffers from a linear error that is corrected. Osman *et al* (2001) reported a linear mapping between the estimate and the actual frequency of $v = 0.96u + 0.035$ where v is the actual frequency and u is the estimate.

If one of these k_3 images is acquired at the same encoding as the tagging was applied, the sequence is identical to DENSE imaging and the phase of the image is a measure of displacement in the through-image plane direction. If the image is acquired with a k_3 encoding different from tagging, a constant phase change is observed over the image. This means that the spatial gradient of phase can be used to measure the relative displacement perpendicular to the imaging plane of neighbouring points, relative to one another, which is sufficient for use in strain calculations.

If $\mathbf{x} = (x_1, x_2)$ are the coordinates of a point in the image plane and x_3 is the through plane position within a voxel, the tissue magnetization (M) as a result of the tagging is defined by:

$$M(\mathbf{x}, x_3, t) = \rho_0(\mathbf{x}, t) + \rho_H(\mathbf{x}, t)cos(\phi(\mathbf{x}, t) + v(\mathbf{x}, t)x_3) \qquad (2.8)$$

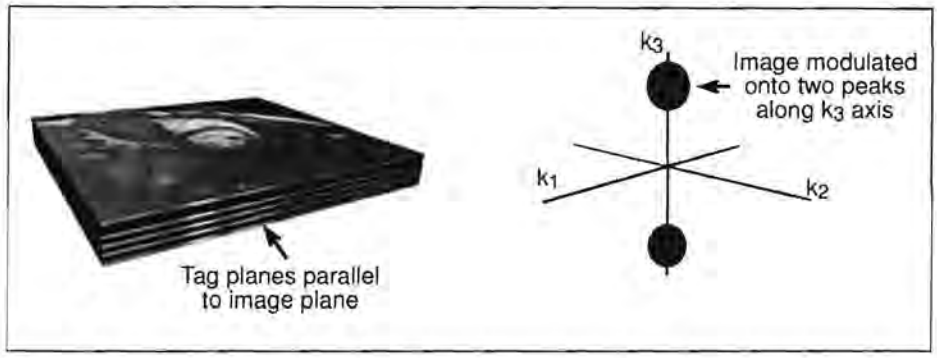

Figure 2.7: The effects of tagging an image parallel to the image plane. On the left is the image space, a slice of myocardium showing the parallel tags. On the right, K-Space, showing how the image slice data is modulated onto two peaks along the k_3 axis.

where ρ_0 is the unmodulated signal that grows with T1 relaxation (tag fading) and ρ_H is the tag amplitude that correspondingly decays with time. The phase ϕ in the above expression gives rise to the frequency of the component of the tags in the image plane, which occurs if the tags tilt out of the image plane due to contraction, and v is the frequency of the tag planes perpendicular to the image plane. The signal along the X_3 axis is dependent on the profile of the excited tissue $g(x_3)$. If the through plane unencoding gradient is ke, the resultant image can be described as the integral over x_3 of the signal:

$$I(\mathbf{x}, t; k_3) = \int_{-\infty}^{\infty} M(\mathbf{x}, x_3, t) g(x_3) e^{-jkex_3} dx_3 \tag{2.9}$$

The above Fourier transform expands to:

$$\begin{aligned} I(\mathbf{x}, t; k_3) = \rho_0(\mathbf{x}, t) G(k_3) + \rho_H(\mathbf{x}, t) e^{-j\phi(\mathbf{x},t)} G(k_3 + v(\mathbf{x}, t)) \\ + \rho_H(\mathbf{x}, t) e^{+j\phi(\mathbf{x},t)} G(k_3 - v(\mathbf{x}, t)) \end{aligned} \tag{2.10}$$

in which G is the Fourier transform of the slice profile g. Each of the three echoes is weighted by the unknown frequency slice profile G. Osman *et al* (2001) suggest a bell shape for G (Figure 2.8) although, in reality, it depends on the profile of the rf excitation pulse.

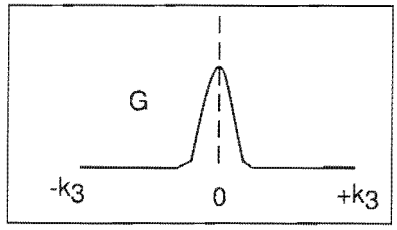

Figure 2.8: Suggested bell shape profile of G.

A priori knowledge of the width of G is important in choosing suitable encoding values to image. The slice thickness (width of g) is inversely proportional to the frequency spread (width of G), so that a thin slice results in a large frequency spread. As mentioned previously, SENC acquires two images at different k_3 encodings. Ideally these two images should lie within the width of G for one of the peaks in order to ensure an accurate estimate for the centre of mass. This is demonstrated in Figure 2.9 where the magnitude of all three echoes are displayed along the k_3 axis.

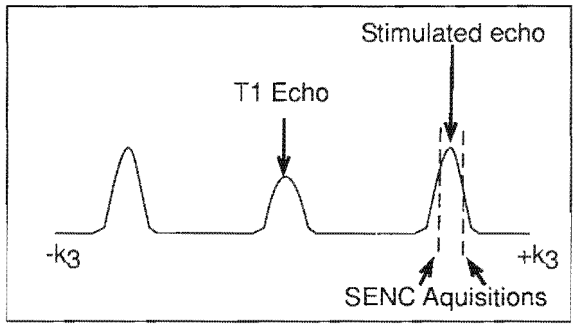

Figure 2.9: k_3 spectrum of G, demonstrating all three echoes arising from tagging and the positions of SENC encodings.

Since SENC relies on the image intensity to estimate the post-deformation tag frequency, it is important that images with a good signal-to-noise ratio (SNR) are acquired. This can be achieved with a large slice thickness and a large read out field of view (RoFOV) that result in large voxels and thus increased signal.

SENC thus allows strain to be measured perpendicular to the imaging plane without requiring adjacent planes to be imaged.

2.5 Superquadratic glyphs

Due to the fact that 3D strain has six components that are expressed in a 3×3 symmetric tensor, its visualization is very complex. Ennis *et al* (2005) described a method to visualize tensor fields using superquadratic glyphs. A glyph is a technique that uses an icon to express the three principal directions and magnitudes of the tensor, eigenvectors and eigenvalues, respectively. Eigenvectors describe the glyph orientation and eigenvalues describe the lengths in that particular direction. The superquadratic glyph technique is able to distinguish isotropic, transversely isotropic and orthotropic tensors. Isotropic tensors have the same components in all rotated coordinate systems (i.e. all the eigenvalues are equal), transversely isotropic tensors have the same components if rotated about a specific axis (two eigenvalues are equal) and orthotropic tensors have three specific axes of preferred orientation (ie. all the eigenvalues are different).

The shapes of superquadratic glyphs range from discs and spheres to cubes and prolates. The shape is determined by the following set of functions:

$$C_L = \frac{\lambda_1 - \lambda_2}{\lambda_1 + \lambda_2 + \lambda_3},\ C_P = \frac{2(\lambda_2 - \lambda_3)}{\lambda_1 + \lambda_2 + \lambda_3},\ C_S = \frac{2\lambda_3}{\lambda_1 + \lambda_2 + \lambda_3} \tag{2.11}$$

where C_L , C_P and C_S are measures of the anisotropy between the three eigenvalues (λ_i) and sum to 1. The three eigenvalues are sorted in ascending order, $\lambda_1 > \lambda_2 > \lambda_3$. The shape of the glyph functions are defined by:

$$C_L \geq C_P \Rightarrow \left[\begin{array}{c} \alpha = (1 - C_P)^\gamma,\ \beta = (1 - C_L)^\gamma \\ \rho(\theta, \phi) = \begin{pmatrix} cos^\beta(\phi) \\ -sin^\alpha(\theta) sin^\beta(\phi) \\ cos^\alpha(\theta) sin^\beta(\phi) \end{pmatrix} \end{array} \right]$$

$$C_L < C_P \Rightarrow \left[\begin{array}{c} \alpha = (1 - C_L)^\gamma,\ \beta = (1 - C_P)^\gamma \\ \rho(\theta, \phi) = \begin{pmatrix} cos^\alpha(\theta) sin^\beta(\phi) \\ sin^\alpha(\theta) sin^\beta(\phi) \\ cos^\beta(\phi) \end{pmatrix} \end{array} \right] \tag{2.12}$$

in which α and β determine the overall superquadratic shape. This shape function can be aligned to the eigenvectors and scaled in that axis by the eigenvalue; γ highlights the differences between the eigenvalues by adjusting

the sharpness of the glyph edges, and is generally chosen to be between 3 and 6. θ and ϕ are local glyph coordinates in a spherical coordinate system

The magnitude of the strain can be represented with a colour mapped to one eigenvalue. These shapes therefore express the 3D strain of the myocardium in a single image. An example of one of these superquadratic glyphs is shown in Figure 2.10, where E1, E2 and E3 are the three principal strains. It demonstrates a transversely isotropic tensor where E2 and E3 are equal, and E1 is larger. The circular nature of the glyph in the E2-E3 plane demonstrate that E2 and E3 are equal and the square nature of the edges between E1 and the E2-E3 plane demonstrate that E1 is significantly larger than E2 and E3 (this is also visible in the fact that the glyph is longer in the E1 axis).

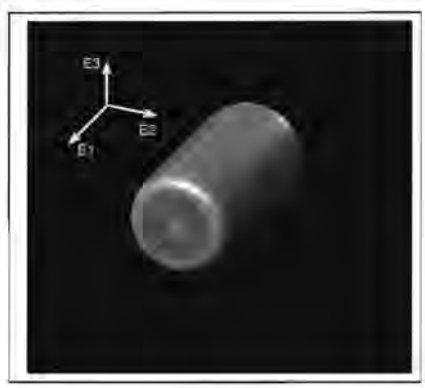

Figure 2.10: Example of transversely isotropic Glyph image, showing the directions of the three principal strains E1, E2 and E3

Chapter 3

Experimental apparatus and techniques

This project develops a technique to measure and calculate 3D intramyocardial strain and further provides 3D strain visualization tools. Images were acquired using cine-DENSE and cine-SENC MRI. A cine-DENSE sequence was adapted to perform both cine-SENC and cine-DENSE acquisitions. Simulations were performed prior to implementation to explore the functional accuracy of the method. These simulations are, however, described in a later section to aid the continuity of this chapter.

3.1 MRI scanner and subjects

The combined cine-DENSE cine-SENC sequence was tested and optimized on an Avanto 1.5 Tesla MRI scanner (Siemens Medical Systems, Erlangen, Germany) located at the University of Virginia (UVA, Charlottesville, Virginia, United States of America). Pulse sequence programming was done with the Siemens Integrated Development Environment for Applications (IDEA) that uses Microsoft Visual C++. The Avanto scanner was running the VB11 software platform.

A total of six volunteers were scanned at UVA. All subjects gave written informed consent in accordance with protocols approved by the UCT and UVA human investigation committees. None of the volunteers had any known cardiac pathology. The images required to optimally tune the cine-SENC

sequence were acquired for five volunteers; strain measurements were performed for four volunteers.

3.2 Sequence programming

The cine-DENSE sequence developed by the University of Virginia (Kim *et al* 2004) was adapted as part of this project to obtain cine-SENC measurements in order to compute 3D strain.

3.2.1 The cine-DENSE sequence

In this project, cine-DENSE was used to measure the two in plane components of displacement. Cine-DENSE achieves fast imaging using a segmented EPI readout trajectory over multiple cardiac phases. Displacement data for one encoding axis is measured in one breathhold, consisting of a phase reference image followed by a CSPAMM pair. The CSPAMM pair serves to double the signal magnitude and suppress the T1 echo.

Each of the three images are acquired over multiple cardiac cycles (typically 5 heart beats per image). The tagging kernel is applied at end diastole for each heart beat and is triggered by the QRS wave of the ECG readout. Tagging can be achieved in any direction by applying the encoding gradient along either the readout, phase encode, or slice select directions, or a combination of these. Due to short repetition times (TR) and the small rf excitation angle, a dummy scan with duration equal to a single cardiac cycle is performed at the start of each of the three image acquisitions to achieve a steady state that serves to reduce EPI artefacts. This series of events is illustrated in Figure 3.1.

After the tagging kernel a slice selective rf excitation pulse is applied at the desired imaging time. This is followed by an unencoding gradient that is opposite and equal to the tag encoding gradient. Therefore each ECG trigger is followed by several rf excitations and their associated EPI readout segments that are used in the reconstruction of images from different cardiac phases. The sequence is illustrated in Figure 3.2.

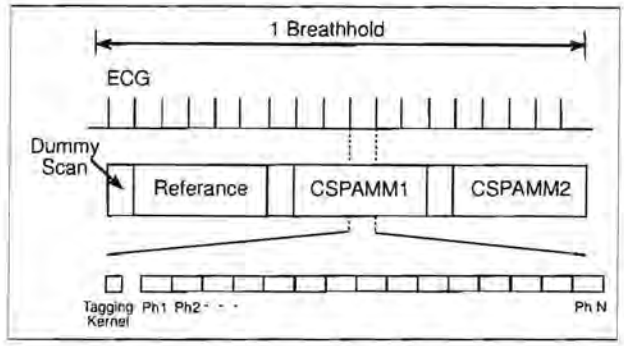

Figure 3.1: Cine-DENSE general sequence timing.

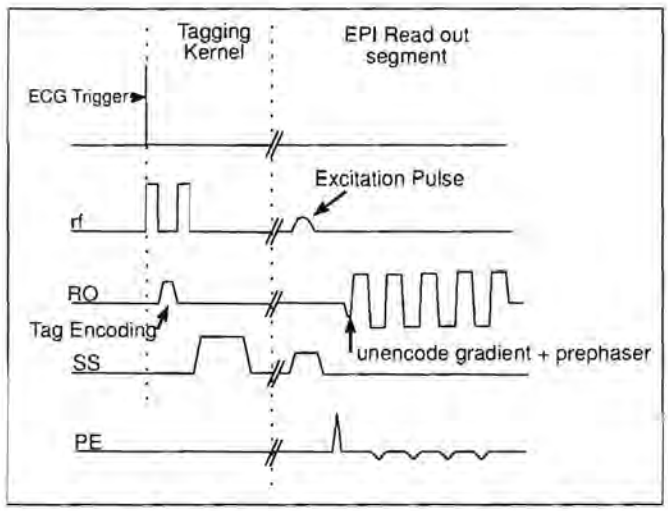

Figure 3.2: The cine-DENSE MRI sequence, where RO is the readout gradient, SS is the slice select gradient, and PE is the Phase encode gradient.

3.2.2 Cine-DENSE sequence code structure

The cine-DENSE sequence was programmed in C++ and compiled with the Siemens IDEA package, version VB11. Essential components of an IDEA sequence are *fSEQInit*, *fSEQPrep*, *fSEQCheck*, *fSEQRun* and *fSEQRunKernel*. *fSEQInit* initialises the sequence hard limits and the protocol interface. *fSEQPrep* prepares the components that are needed at run time. *fSEQCheck* checks the real time sequence for gradient overflows. *fSEQRun* and *fSEQRunKernel* execute the sequence and control its basic timing elements.

The special sequence dependent parameters are set in the sequence special card in the protocol editor prior to each running of the sequence. The interface of this special card to the sequence is initialised in the global *fSEQInit* function and parameter changes are handled through a set of global functions.

The tagging kernel is encapsulated in the *SBBLineTagDENSE* class that is run by the *fSEQRunKernel* where the final sequence preparation is performed. The pre-readout excitation and gradients are encapsulated in the *SeqBuildBlockGREEPIKernel* class that is also run after final preparation in the *fSEQRunKernel*. This class controls the *EPIReadOut* class that performs the actual rf signal acquisition and EPI trajectory traversal through k-space. This structure is summarised in the class relationship diagram in Figure 3.3.

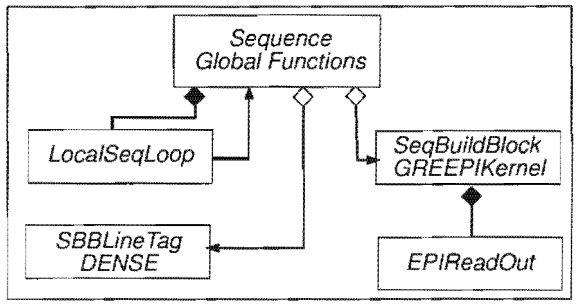

Figure 3.3: Cine-DENSE class structure diagram.

The general sequence flow is controlled in the *fSEQRunKernel* where the type of image acquisition is set, for example a reference image or encoded image and which type of CSPAMM image is to be acquired. In this structure, the encoding gradient is applied in the *SBBLineTagDENSE* kernel, between the two 90° rf Pulses. The unencoding gradients are applied in the *SeqBuildBlockGREEPI* kernel.

3.2.3 Modifications to achieve cine-SENC capability

Cine-SENC capability was added to the cine-DENSE sequence. The new sequence was termed a cine-SENC-DENSE sequence. Four main areas required modification.

Firstly, the ability to choose between performing a DENSE acquisition or

a SENC acquisition was added to the protocol editor interface and in the SENC case, interface variables were added to specify the sequence parameters and type of SENC scan to perform. The former was done by adding an extra selection to the DENSE scan mode dropdown menu in the sequence special card of the protocol editor, allowing the user to choose between CSPAMM DENSE and SENC. In the latter a second dropdown selection box was added to enable the user to choose whether to perform a reference scan, no reference scan, or a conjugate scan (for which the unencoding gradient of the second SENC image is negated). Two double-type variable edit fields were added to specify the moment of the unencoding gradient and the step size, respectively. The step size refers to the increase in unencoding gradient strength between successive SENC images. The additions to the special card parameters are indicated with arrows in Figure 3.4.

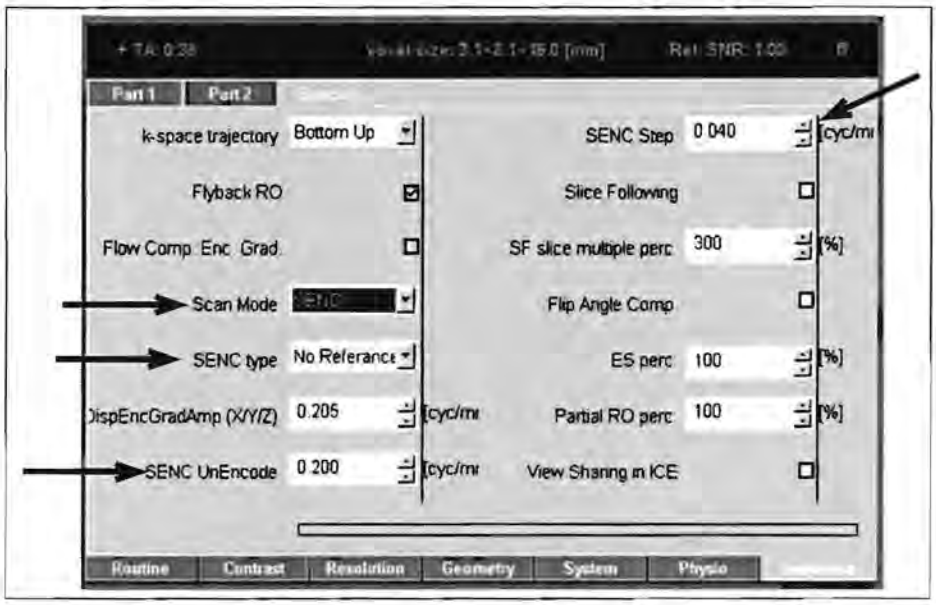

Figure 3.4: POET - changes to the sequence special card.

Secondly, the *SBBLineTagDENSE* class was modified to enable a greater encoding gradient. The duration between the two tagging rf pulses was increased in order that a gradient moment of 0.4 cyc/mm could be achieved as described by Osman *et al* (2001).

Thirdly, the global sequence running pattern was modified in the *fSEQRunKernel* to determine the sequence of images acquired, that is, a phase

reference image (if specified) followed by either two or three encoded images.

Finally, the unencoding gradient in the slice select direction was modified to equal the value specified in the protocol editor (with step size increments for successive images and negation if conjugation had been selected). As with DENSE, this gradient was implemented simultaneously with the slice select refocusing gradient.

3.2.4 Tuning of the cine-SENC measurement

The parameters that required optimisation were the encoding and unencoding gradients, the unencoding step size, and parameters that affect the SNR and thus the SENC results, such as slice thickness (ST) and readout field of view (RoFOV). EPI parameters required tuning also as certain combinations produce artefacts that gave rise to significant signal loss through ghosting.

Phantom experiments were performed to investigate the relationship between ST and the frequency slice profile. The phantom comprised a plexiglass cylinder filled with agarose gel for which the T1 and T2 properties are similar to myocardium. Four experiments were performed using slice thicknesses of 8mm, 11mm, 14mm and 16mm, respectively. In all cases a RoFOV of 400mm was used. For this experiment the actual encoding value was inconsequential, but the range of unencoding values and frequency resolution were important. The table below lists the parameters used:

Table 3.1: Parameters used for phantom scans.

Slice Thickness (mm)	Encoding (cyc/mm)	Minimum unencoding (cyc/mm)	Maximum unencoding (cyc/mm)	Unencoding resolution (cyc/mm)
8	0.4	0.19	0.60	0.01
11	0.2	0.135	0.265	0.005
14	0.42	0.32	0.525	0.005
16	0.2	0.115	0.260	0.005

SNR in myocardium is less than SNR in the phantom. In order to relate SNR of the phantom data to expected values in human subjects, SNR was calculated for a human volunteer and in a phantom using the identical encoding technique. This relationship was measured using the DENSE protocol with an encoding gradient of 0.1cyc/mm. The reason for using DENSE is that in SENC, encoding the myocardium through the image plane for human data

results in intra voxel dephasing (the SENC effect) that will affect the SNR results as the phantom will not experience dephasing and myocardium will.

Once the relationship between the width of the frequency slice profile and ST is understood, the appropriate parameters for volunteer studies needed to be determined. This process was initiated using the encoding moment suggested by Osman *et al* (2001) of 0.4cyc/mm. The width of the frequency slice profile should cover double the range of frequency change expected due to longitudinal strain in normal myocardium (15%). The following formula was used to calculate the strain from SENC images (Osman *et al* 2001):

$$E = \frac{W}{\sqrt{\omega^2 + v^2}} - 1 \tag{3.1}$$

in which W is the initial encoding frequency, ω is the in plane component of modulation at the imaging time, and v is the through plane frequency of modulation at the imaging time. The above expression yields a required frequency width of greater than 0.14cyc/mm (from first zero crossing to the next) for an encoding gradient of 0.4cyc/mm. The phantom studies indicated that an 8mm slice thickness would produce the necessary frequency spread.

Volunteer scanning was an iterative process involving changing ST, RoFOV, encoding and unencoding frequencies, as well as EPI readout parameters. Five volunteers were scanned in this process. The parameters for each volunteer are listed in Table 3.2. Volunteer 1 was scanned using both RoFOV of 360mm and 480mm. DENSE uses 360mm RoFOV whereas Osman *et al* (2001) used 480mm in their SENC sequence. The effect of doubling the slice thickness was explored during the scans on volunteer 2. For this volunteer the encoding frequency was reduced to 0.2cyc/mm to reduce the frequency shift from myocardial contraction as the doubled slice thickness halves the frequency profile.

The third volunteer was scanned to investigate the effects of EPI echo train length and segments on artefact generation in the image. EPI ghosting can result in significant signal attenuation. Different combinations of echo train length and segments were explored and the artefacts produced were compared. For this volunteer the ST was also reduced to 11mm so as to increase the frequency spread.

The fourth volunteer was scanned using an echo train length of 15 with 15

Table 3.2: Parameters used in cine-SENC volunteer scans.

	Encoding (cyc/mm)	ST (mm)	Unencodings (cyc/mm)	RoFOV (cyc/mm)	EPI Echo Train length (Segments)
1	0.4	8	0.4, 0.47	360 and 480	9(18)
2	0.2	16	0.2, 0.235	360	9(18)
3	0.2	11	0.2, 0.24	480	9(18), 7(14), 5(10), 9(9)
4	0.2	11	0.2, 0.24	480	15(15)
5	0.15	16	0.15, 0.185	480	9(18)

segments EPI configuration to further investigate appropriate EPI parameters, a slice thickness of 11mm, and an encoding frequency of 0.2cyc/mm. The SNR was maximized for the last volunteer with a 16mm ST and 480mm RoFOV. The encoding frequency was reduced to 0.15cyc/mm with unencoding frequencies at 0.15cyc/mm and 0.185cyc/mm.

3.2.5 Imaging Protocols

The kinematic data to formulate 3D strain were acquired over a 16mm slice in five breathholds. The upper 8mm's of the slice were imaged during two breathholds with cos CSPAMM cine-DENSE, one encoded in the X_1 direction and one in X_2, where X_1 and X_2 are mutually orthogonal and lie within the image plane. This was repeated in another two breathholds for the lower 8mm's of the slice. Cine-SENC data, consisting of a phase reference and two encoded images, were acquired in the fifth and final breathhold. These imaging planes are demonstrated in Figure 3.5.

The parameters used in the CSPAMM cine-DENSE and cine-SENC acquisitions are listed in tables 3.3 and 3.4, respectively. The cine-DENSE parameters yield a voxel size of 2.8 x 2.8 x 8mm, whereas the cine-SENC voxel size is 3.75 x 3.75 x 16mm.

3.3 Image processing and computation of strain

Post-processing algorithms were applied to both the cine-DENSE and cine-SENC images prior to computation of 3D strain. Post processing of both DICOM and raw data files were performed in a graphical user interface

Table 3.3: Parameters for cine-DENSE.

Parameter	Value
Read out Field of View	360mm
Percent Field of View Phase	75%
Acquisition window	800ms or less
TR	22ms
Bandwidth	800Hz
EPI Factor (train length)	9
Segments	18
Displacement encoding	0.1cyc/mm
rf Excitation angle	15°

Table 3.4: Parameters for cine-SENC acquisition.

Parameter	Value
Readout Field of View	480mm
Percent Field of View Phase	75%
Slice Thickness (ST)	16mm
Acquisition window	800ms or less
TR	22ms
Bandwidth	800hz
EPI Factor (train length)	9
Segments	18
Encoding	0.15cyc/mm
rf Excitation angle	15°
SENC type	Reference
Initial Unencoding	0.15cyc/mm
SENC unencode step size	0.035cyc/mm

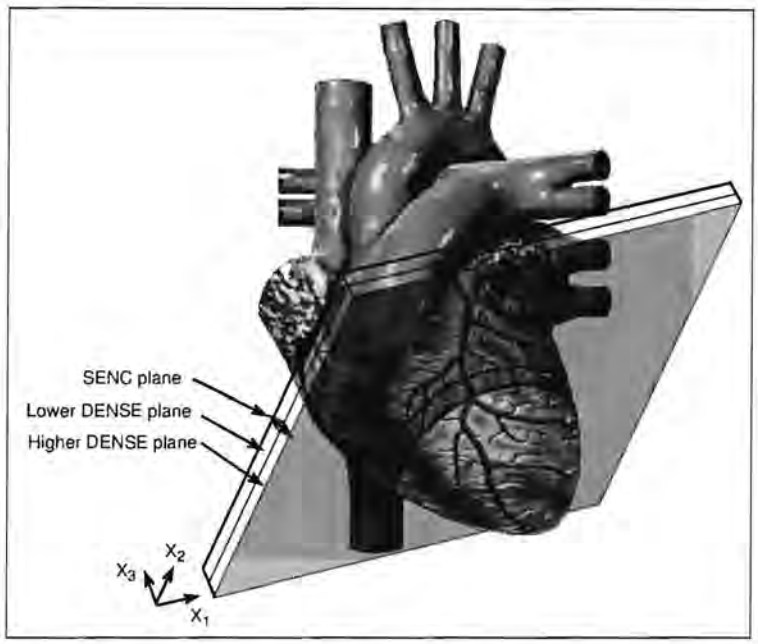

Figure 3.5: Illustration of cine-DENSE and cine-SENC imaging planes in protocol.

(GUI). All post processing was performed using MATLAB (The Mathworks Inc, Natick, MA, USA).

3.3.1 The image processing and strain calculation GUI

The image processing and strain calculation GUI (Main_GUI) controls all the post processing of the cine-DENSE and cine-SENC data and performs a number of important functions. The first function is to read the DICOM or raw data files into the GUI data structure. For the cine-DENSE images this was done using the DICOM cine-DENSE read functions provided in the CineDENSEAnalysis3D GUI written for the University of Cape Town and the University of Virginia. For the cine-SENC DICOM and raw data files, read functions were written that read in up to three different image groups scanned in one acquisition (typically phase reference, first SENC plane and second SENC plane). Phase correction of the cine-SENC data was performed at this stage by subtracting the phase of the phase reference, if acquired, from each of the encoded images. After the DICOM images have been loaded, a 2D cross-correlation between the first cine-DENSE data set and

all the other cine-DENSE data sets acquired was performed in order to align each image set to the others. Cine-SENC images were aligned manually with slider bars displayed beside the images, since cross-correlation techniques would not work consistently for SENC images due to the low signal intensity for the myocardium.

If the cine-SENC acquisition had a larger RoFOV it was scaled to obtain the same pixel size as the cine-DENSE acquisitions. Resizing was performed with a bilinear interpolation between complex neighbouring voxels to yield a higher resolution cine-SENC image.

The GUI also allows the user to view the magnitude or phase data of any of the acquired cine-DENSE or cine-SENC images via two drop-down selection boxes. It is important to view all of the images acquired in order to ensure that they are aligned correctly.

The GUI provides the ability to manually contour the myocardium and adjust these contours so that they fit for all images of all acquisitions. One set of contours should fit all the different sets of images. The contouring requires drawing of both endocardial and epicardial polygons. Vertices may be moved or added to the contour to allow contour adjustment, which is important when dealing with multiple data sets.

The cine-DENSE and cine-SENC post-processing functions as well as the functions that perform the 3D intramyocardial strain calculation are called from the GUI. The features of the GUI are illustrated in Figure 3.6.

3.3.2 Cine-DENSE Processing

Several post-processing procedures are performed on the complex cine-DENSE images for each encoding direction and imaging plane. The first two procedures are performed online by the scanner's MR image reconstruction (MRIR) computer and involve subtraction of the CSPAMM image pairs to remove the T1 echo. This effectively doubles the magnitude of the encoded data. Phase correction is achieved by subtracting the phase of the reference image from the phase of the encoded image (post CSPAMM correction).

The remainder of the post processing was performed offline on a stand alone computer using the Matlab functions provided in CineDenseAnalysis3D. For calculating 3D strain from cine-DENSE and cine-SENC data only one further post processing step was performed, this was spatial and temporal

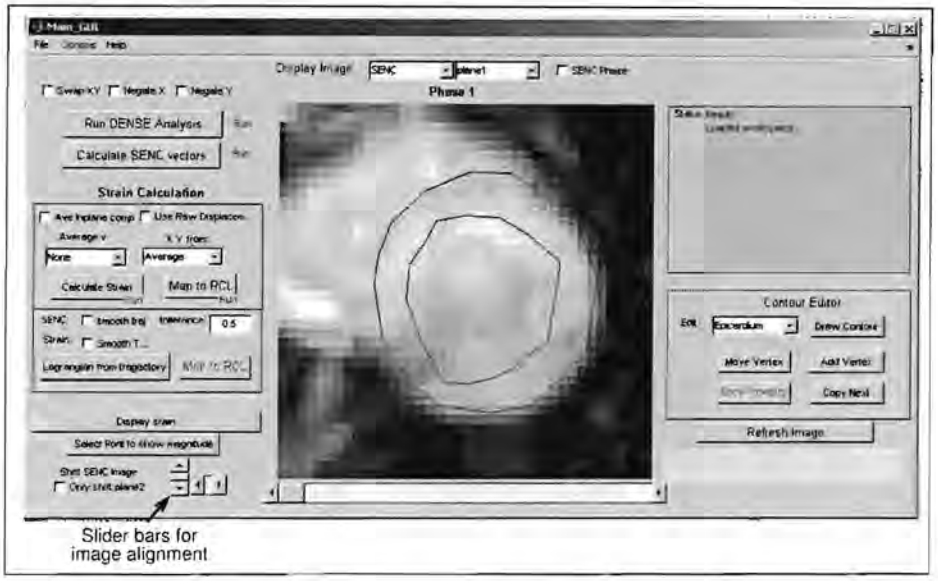

Figure 3.6: Main_GUI interface for data processing.

phase unwrapping. A guided flood-fill algorithm was used (Spottiswoode *et al* 2005a) that allows the calculation of absolute displacement of the myocardial tissue in each voxel. Typically this phase unwrapping is not essential in 2D strain calculation, however as strain is to be calculated from two separate cine-DENSE image planes (higher and lower) this procedure was necessary to ensure that there is no displacement offset between the two planes.

For motion trajectory based strain calculation, as described in later sections, the motion of the myocardium in the first cine frame was tracked through time using a weighted nearest neighbours interpolation of the displacement vectors in each frame. This yields for each frame a field of displacement vectors that originate at the starting points of the trajectories. Displacement vectors of successive frames are subtracted to obtain motion trajectories. Temporal fitting (Spottiswoode *et al* 2005b) was applied to the trajectories to reduce noise and produce Lagrangian equations of motion. These tasks were performed using the CineDENSEanalysis3D software tool for analysing cine-DENSE data.

3.3.3 Cine-SENC processing

Each myocardial voxel at each time frame of the cine-SENC acquisition was processed to calculate a vector describing the frequency and orientation of its tag planes. The in plane and through plane components of the cine-SENC vector were calculated using phase and magnitude data, respectively. A Matlab function was written to process cine-SENC acquisitions with either two or three unencoded images.

In the case where images were acquired for three unencoding frequencies, the two images with the greatest signal magnitude for the same tissue were selected, on a voxel by voxel basis, and processed in the same manner as if images were acquired for two unencoding frequencies. A centre of mass (COM) estimate was performed for the two identical voxels at different unencoding frequencies using the following formula:

$$u = \frac{W_a|P1| + W_b|P2|}{|P1| + |P2|} \tag{3.2}$$

in which $P1$ and $P2$ are the values of the voxels for encoding frequencies W_a and W_b, respectively. Osman *et al* (2001) reported a linear error in u that could be removed using

$$v = a \cdot u + b \tag{3.3}$$

with a and b equal to 1.0368 and -0.01392, respectively. Optimal results were achieved using a and b equal to 0.96 and 0.004, respectively. This result (v) is the tag frequency perpendicular to the imaging plane.

The spatial gradient of phase ($\Delta\phi$), which yields the tag frequency in the imaging plane, was computed from the change in through plane displacement between neighbouring voxels in the SENC images based on the principle that displacement is encoded onto the phase of the image. For SENC images the fact that the unencoding gradient is unequal to the encoding gradient simply results in a phase offset that does not influence relative displacement measurements. This change in displacement between neighbouring voxels was recorded separately for each neighbour of a voxel, so that each combination could be treated separately in computing the deformation gradient in the strain calculation. The in plane tag frequency at the imaging time is then given by

$$w = \Delta x_3 \cdot \frac{ke}{V_w} = \frac{\Delta\phi}{2\pi \cdot ke} \cdot \frac{ke}{V_w} \tag{3.4}$$

where ke is the SENC encoding frequency, V_w is the voxel width and Δx_3 is the difference in x_3 displacement between neighbouring voxels. Figure 3.7 is a flow diagram of the processing performed on the cine-SENC images. The resultant tag plane frequency vectors are normal to the tag plane and have a magnitude equal to the tag frequency.

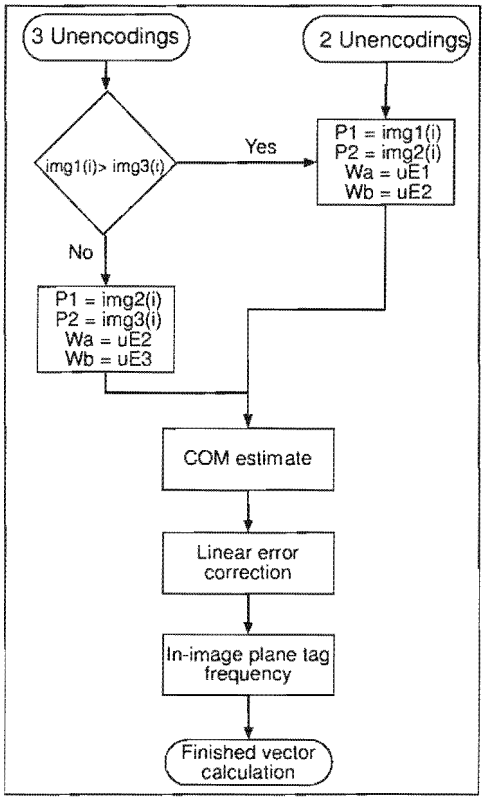

Figure 3.7: Flow diagram of SENC post processing performed for each frame and voxel.

3.3.4 Computation of Strain using DENSE and SENC MRI

This project proposes a combination of cine-DENSE and cine-SENC MRI to compute 3D strain. Cine-SENC was used to measure through plane deformation due to the fact that it is robust against myocardial shifts between

breathholds and demonstrates low measurement noise. 2D cine-DENSE images were acquired for two orthogonal in plane encoding directions for two adjacent image planes in order to fully formulate the through plane shear strains.

Strain was calculated using four voxels adjacent to a selected voxel in both the higher and lower DENSE image planes, as well as these same five adjacent voxels from the SENC image, as illustrated in Figure 3.8. The proposed method reconstructs the inverse deformation gradient F_{inv} using eight different combinations of these voxels. In Figure 3.8 voxel C is the voxel for which strain is to be calculated and A, B, L and R represent the voxel above, below, to the left and to the right of C, respectively. A subscript h or l denotes higher (h) or lower (l) DENSE image planes. The eight combinations are [A_h R_h C_h C_l], [R_h, B_h C_h C_l], [B_h L_h C_h C_l] , [L_h A_h C_h C_l], [A_l R_l C_h C_l], [R_l, B_l C_h C_l], [B_l L_l C_h C_l] , [L_l A_l C_h C_l]. A value for F_{inv} is calculated for each of the eight combinations for which all the voxels fall within the myocardial contours. The strain calculation is then performed using an average of all the inverse deformation gradients.

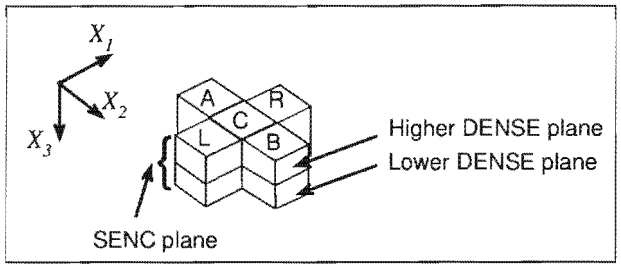

Figure 3.8: Voxel neighbours used in combination SENC and DENSE strain calculation.

The inverse deformation gradient (F_{inv}) is calculated using

$$F_{inv} = \begin{bmatrix} \frac{\delta x_1}{\delta X_1} & \frac{\delta x_1}{\delta X_2} & \frac{\delta x_1}{\delta X_3} \\ \frac{\delta x_2}{\delta X_1} & \frac{\delta x_2}{\delta X_2} & \frac{\delta x_2}{\delta X_3} \\ \frac{\delta x_3}{\delta X_1} & \frac{\delta x_3}{\delta X_2} & \frac{\delta x_3}{\delta X_3} \end{bmatrix} \tag{3.5}$$

where $\frac{\delta x_i}{\delta X_j}$ is the partial derivative of the displacement in direction x_i with respect to axis X_j. Terms with $i = 1$ or 2 are calculated directly from the DENSE displacement data and the partial derivatives of x_3 in directions X_1 and X_2 are calculated using the SENC spatial gradient of phase. The final

term with $i, j = 3$ is calculated using the change in the through plane tag frequency as computed from SENC.

Consider, for example, the calculation of F_{inv} for the set of voxels [A_h, R_h, C_h, C_l]. The first step is the formation of three non-coplanar vectors $\mathbf{V}_{Ah}$, $\mathbf{V}_{Rh}$ and $\mathbf{V}_{Cl}$ each originating from the centre of C_h towards the centres of A_h, R_h and C_l, respectively. The calculation of these vectors at the imaging time is trivial, with each vector lying parallel to one of the axes X_1, X_2 or X_3, respectively, and with magnitudes equal to the voxel separation ($\mathbf{V}_{Ah}$ and $\mathbf{V}_{Rh}$ are 2.8mm long and $\mathbf{V}_{Cl}$ has a magnitude equal to the difference in slice position between the higher and lower DENSE image planes, 8mm). The calculation of these vectors at the start of the cardiac cycle, now $\mathbf{V}'_{Ah}$, $\mathbf{V}'_{Rh}$ and $\mathbf{V}'_{Cl}$, is performed using both DENSE and SENC data. The difference in X_1 and X_2 displacements between C_h and the respective neighbouring voxels, calculated using DENSE measurements, produces the X_1 and X_2 components for each vector.

The X_3 components of these vectors are calculated using the SENC frequency vectors that describe the orientation and frequency of the tag planes for each voxel. This is based on the knowledge of how a plane (parallel to the tag plane) deforms over the cardiac cycle. Consider each vector individually: if its head lies in a plane parallel to the tag plane then the equation for that plane at the imaging time is given by:

$$ax_1 + bx_2 + cx_3 = d \tag{3.6}$$

In the above expression a, b and c are the components of the SENC frequency vector normal to the tag plane and scaled to unit length at the imaging time, and d represents the perpendicular distance of the plane from an origin centred at C_h. The value of d is calculated by substituting the components of the vector $\mathbf{V}$ into x_1, x_2 and x_3. The equation for the plane through the same vector head and parallel to the tag plane at the start of the cardiac cycle is given by:

$$a'x_1 + b'x_2 + c'x_3 = d' \tag{3.7}$$

in which a', b', and c' are the components of the unit vector normal to the tag planes at the start of the cardiac cycle. In order to determine the distance of this plane from the origin at C'_h, d' is computed using

$$d' = d\frac{|\mathbf{S}|}{|\mathbf{S}'|} \tag{3.8}$$

where $\mathbf{S}$ is the frequency vector of the tag planes at the imaging time and $\mathbf{S}'$ is the applied tag plane frequency vector at the start of the cardiac cycle. Using the equation of a plane for each vector ($\mathbf{V}'_{Ah}$, $\mathbf{V}'_{Rh}$ and $\mathbf{V}'_{Cl}$) at the start of the cardiac cycle, the X_3 components of each can now be determined by solving for x_3 after substituting known values for x_1 and x_2.

F_{inv} is then calculated using these three non-coplanar vectors as follows:

$$F_{inv} = [\mathbf{V}'_{Ah} \quad \mathbf{V}'_{Rh} \quad \mathbf{V}'_{Cl}]/[\mathbf{V}_{Ah} \quad \mathbf{V}_{Rh} \quad \mathbf{V}_{Cl}] \tag{3.9}$$

This process was repeated for each combination of voxels that lie within manually defined myocardial boundaries and the mean F_{inv} was found. The mean of F_{inv} was determined before matrix inversion so as to reduce the noise that would be propagated across the components of F.

The Lagrangian strain (E_L) was then computed using

$$E_L = \frac{1}{2}(F^T F - I) \tag{3.10}$$

and the Eulerian strain (E_E) using the average F_{inv} as follows:

$$E_E = \frac{1}{2}(I - F_{inv}^T F_{inv}) \tag{3.11}$$

The final calculation performed on these strain measures was to rotate them to the radial, circumferential and longitudinal (RCL) coordinate system. The rotation tensor was calculated such that the first dimension of the strain tensor represents the radial strain and is given by:

$$R = \begin{bmatrix} cos(\theta) & -sin(\theta) & 0 \\ sin(\theta) & cos(\theta) & 0 \\ 0 & 0 & 1 \end{bmatrix} \tag{3.12}$$

Where θ is the angle between the X_1 direction and the radial direction with the radial direction defined by the vector joining the centroid of the surface enclosed by the epicardial boundary to the position of the strain measure.

3.3.5 2D Lagrangian strain calculation using cine-DENSE temporal trajectories

Calculating strain directly from the temporal trajectories of tracked myocardium provides several enhancements to the 2D data analysis process. These enhancements include viewing the deformation of one unit of myocardium over the cardiac cycle, i.e. displaying the strain on a Lagrangian map of myocardium. The second advantage is that strain can be calculated at any desired temporal resolution as the equations of displacement can be evaluated at any desired time point before the last measurement. The trajectories can also be evaluated at any desired spatial resolution, although it should be noted that for both a temporal resolution greater than the number of myocardial frames acquired and a spatial resolution greater than the pixel resolution no additional information is added but simply more continuous data. The difficulty when analyzing strain in different myocardial segments is that the myocardium twists and contracts asymmetrically throughout the heart cycle causing tissue to move into adjacent segments. This problem is solved by using trajectories. The segments are defined at the start of the cardiac cycle and then tracked through time.

The technique to calculate strain using the trajectories is trivial as the deformation information provided by the trajectories is inherently Lagrangian. A Matlab function was written to calculate 2D strain directly from these trajectories at any desired time point. Each strain calculation was associated with a trajectory, and thus centred about that trajectory. The mask of trajectories used to calculate the strain contains five trajectories (C, A, R, B and L) whose arrangement of starting points are demonstrated in Figure 3.9.

Vectors $\mathbf{V}_A$, $\mathbf{V}_R$, $\mathbf{V}_B$ and $\mathbf{V}_L$ are formed by connecting, for the same point in time, trajectory C to A, R, B and L, respectively. Two of these vectors are illustrated in Figure 3.9B and C before and after deformation. A prime ($'$) is used to denote the same vector at a later time. The Lagrangian deformation gradient F is calculated four times, using each of the four different combinations of non co-linear vectors ($[\mathbf{V}_A, \mathbf{V}_R]$, $[\mathbf{V}_B, \mathbf{V}_R]$, $[\mathbf{V}_B, \mathbf{V}_L]$ and $[\mathbf{V}_A, \mathbf{V}_L]$). For example, using the vectors demonstrated in Figure 3.9B and C, F is given by

$$F = [\mathbf{V}'_A \ \ \mathbf{V}'_R]/[\mathbf{V}_A \ \ \mathbf{V}_R] \tag{3.13}$$

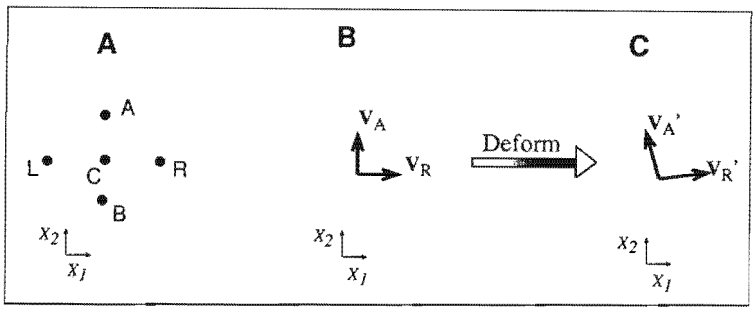

Figure 3.9: A) Arrangement of trajectory starting points used in strain calculation. B) Example of vectors joining trajectories at start of cardiac cycle. C) Same vectors joining trajectories after deformation.

Lagrangian strain was computed from the average of all the deformation gradients (F) in this formation which fell within the myocardial contours.

If the trajectories are computed for all three spatial dimensions, the accuracy of the deformation gradient can be improved by calculating the deformed vectors in 3D. It should be noted, however, that the vectors prior to deformation should be left as 2D vectors as the third dimension of these vectors will not affect the calculation of the 2D strain.

The above method for computing 2D strain is currently being used by researchers at UCT and UVA. The effects of using 3D vectors rather than 2D vectors were investigated by analysing data where 3D displacements had been calculated and plotting strain time curves of one myocardial segment for both 2D and 3D vectors.

3.3.6 3D Lagrangian strain calculated using two adjacent sets of cine-DENSE temporal trajectories

Although this technique suffers from the effects of respiratory miss-alignment of myocardium between breathholds, it was computed to allow comparison with the combined DENSE SENC technique. As this method calculates the strain from 3D trajectories it offers the same potential advantages as the previously mentioned trajectory based 2D strain calculation technique. A function was written in Matlab to perform the strain calculation. Although the function evaluates the strain at a fixed temporal resolution, it could be

extended to evaluate strain at any chosen time point by using the temporal equations of motion.

The Figure 3.10 demonstrates the two different combinations of trajectories used to produce two separate strain fields. The reason for this arrangement is to keep the in plane components of strain separate for each image plane.

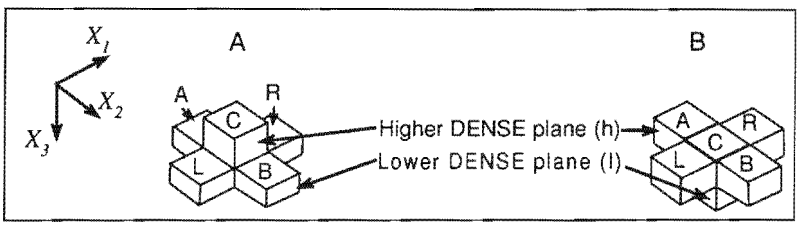

Figure 3.10: Formation of trajectories used in 3D strain calculation. Each trajectory starts in the centre of the voxels shown. A and B are two different formations used to calculate two strain fields.

Using trajectories that originate from centres of the voxels shown in Figure 3.10, vectors are created from C_l in scenario A or C_h in scenario B to the five adjacent voxels (C_h or C_l, A, R, B, and L). A 3D deformation gradient is constructed using combinations of non co-linear in plane vector pairs as described previously together with the added through plane vector. The deformation gradient is calculated four times in each scenario and if a trajectory is not contained in the myocardial boundaries, the deformation gradient containing that trajectory was not computed.

For example, the deformation gradient for one group of trajectories in scenario B whose vectors are $\mathbf{V}_A$, $\mathbf{V}_R$ and $\mathbf{V}_{Cl}$ at the start of the cardiac cycle and $\mathbf{V}'_A$, $\mathbf{V}'_R$ and $\mathbf{V}'_{Cl}$ post deformation, is calculated using:

$$F = [\mathbf{V}'_A \ \mathbf{V}'_R \ \mathbf{V}'_{Cl}]/[\mathbf{V}_A \ \mathbf{V}_R \ \mathbf{V}_{Cl}] \tag{3.14}$$

The average deformation gradient is used to calculate strain.

3.4 Error quantification simulation

The error in the strain tensor can be grouped into one of two areas, namely myocardial position variability between breathholds and noise in the kine-

matic measurements. The inter-breathhold error is predominantly due to variations in the volume of the lungs in different breathholds.

3.4.1 Measurement of inter-breathhold myocardial position variability in a volunteer

The first step in investigating the effects of inter-breathhold myocardial position variability is to obtain a measure of the inter-breathhold myocardial misalignment in a healthy volunteer. In this exercise ten series of long axis gradient recalled echo cine-EPI images were acquired in ten separate breathholds for a healthy volunteer. Five of these series were acquired in the two chamber long axis view and the other five with a four chamber long axis view.

Matlab was used to analyze these images. The myocardium was contoured and the long axis labelled for the last image in each cine series. An example from each group of images and the contouring is shown in Figure 3.11.

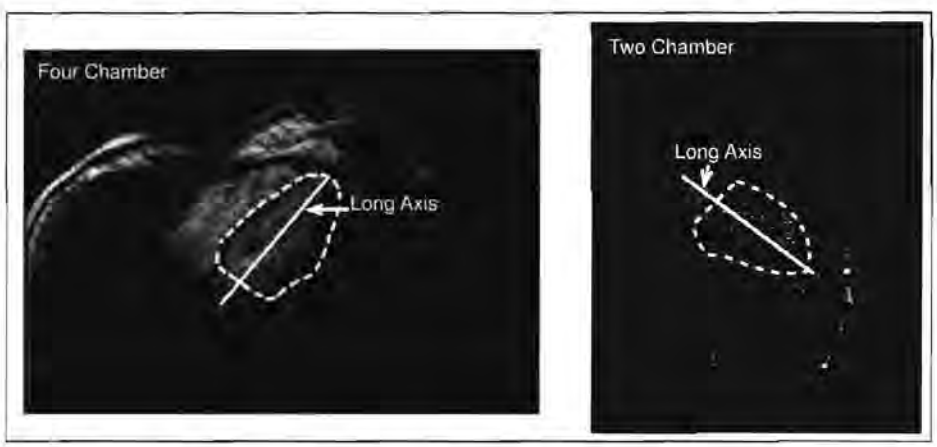

Figure 3.11: Long axis images to determine inter-breathhold myocardial position variability.

Four measurements were obtained from each of these images to demonstrate how the myocardium tilts, shifts in the long axis, and shifts in the mid-ventricular short axis. These are the angle of the long axis in the image, the separation of the furthest separated contours at the base, in the long axis direction, the same at the apex of the heart, and lastly the distance between

the two furthest separated contours at a mid-ventricular short axis image plane (perpendicular to long axis).

3.4.2 Simulation to estimate the error due to inter-breathhold myocardial position variability

A simulation was performed to estimate the effect of obtaining strain measurements from slightly offset measurement planes. The simulations were performed in Matlab. A pseudo inverse deformation gradient was calculated for the purpose of reconstructing measurements at specified imaging planes. Pseudo deformation gradients were calculated using an optimization tool to solve for a specified strain tensor. Twelve end systolic strain tensors, formulated from the results published by Moore *et al* (2000) were used to reconstruct deformation gradients. These are listed below and are orientated in the radial (R), circumferential (C) and longitudinal (L) coordinate systems:

E = Strain and F = deformation gradient.

$$E = \begin{bmatrix} 0.46 & -0.01 & 0.03 \\ -0.01 & -0.15 & 0.01 \\ 0.03 & 0.01 & -0.12 \end{bmatrix} \quad F = \begin{bmatrix} 1.378 & -0.053 & -0.016 \\ 0.064 & 0.833 & 0.017 \\ 0.091 & 0.051 & 0.868 \end{bmatrix}$$

$$E = \begin{bmatrix} 0.43 & -0.02 & 0.08 \\ -0.02 & -0.13 & 0.03 \\ 0.08 & 0.03 & -0.12 \end{bmatrix} \quad F = \begin{bmatrix} 1.355 & -0.029 & 0.028 \\ 0.087 & 0.855 & 0.040 \\ 0.132 & 0.027 & 0.866 \end{bmatrix}$$

$$E = \begin{bmatrix} 0.39 & 0.10 & 0.06 \\ 0.10 & -0.11 & 0.04 \\ 0.06 & 0.04 & -0.12 \end{bmatrix} \quad F = \begin{bmatrix} 1.319 & 0.052 & 0.006 \\ 0.150 & 0.874 & 0.035 \\ 0.114 & 0.045 & 0.875 \end{bmatrix}$$

$$E = \begin{bmatrix} 0.44 & 0.05 & -0.05 \\ 0.05 & -0.15 & 0.09 \\ -0.05 & 0.09 & -0.11 \end{bmatrix} \quad F = \begin{bmatrix} 1.364 & 0.005 & 0.087 \\ 0.105 & 0.832 & 0.005 \\ 0.025 & 0.016 & 0.880 \end{bmatrix}$$

$$E = \begin{bmatrix} 0.54 & 0.09 & 0.01 \\ 0.09 & -0.18 & 0.03 \\ 0.01 & 0.03 & -0.11 \end{bmatrix} \quad F = \begin{bmatrix} 1.427 & 0.030 & -0.047 \\ 0.161 & 0.800 & 0.030 \\ 0.094 & 0.035 & 0.881 \end{bmatrix}$$

$$E = \begin{bmatrix} 0.68 & 0.09 & 0.02 \\ 0.09 & -0.19 & 0.04 \\ 0.02 & 0.04 & -0.15 \end{bmatrix} \quad F = \begin{bmatrix} 1.521 & 0.013 & -0.052 \\ 0.187 & 0.785 & 0.040 \\ 0.132 & 0.050 & 0.837 \end{bmatrix}$$

$$E = \begin{bmatrix} 0.53 & 0.05 & 0.05 \\ 0.05 & -0.18 & 0.03 \\ 0.05 & 0.03 & -0.12 \end{bmatrix} \quad F = \begin{bmatrix} 1.424 & -0.008 & -0.010 \\ 0.131 & 0.806 & 0.037 \\ 0.123 & 0.029 & 0.871 \end{bmatrix}$$

$$E = \begin{bmatrix} 0.40 & 0.05 & 0.07 \\ 0.05 & -0.16 & 0.03 \\ 0.07 & 0.03 & -0.09 \end{bmatrix} \quad F = \begin{bmatrix} 1.335 & -0.000 & -0.018 \\ 0.110 & 0.828 & 0.039 \\ 0.116 & 0.024 & 0.907 \end{bmatrix}$$

$$E = \begin{bmatrix} 0.51 & 0.05 & 0.05 \\ 0.05 & -0.17 & 0.03 \\ 0.05 & 0.03 & -0.12 \end{bmatrix} \quad F = \begin{bmatrix} 1.414 & -0.009 & -0.0098 \\ 0.125 & 0.817 & 0.043 \\ 0.119 & 0.037 & 0.866 \end{bmatrix}$$

$$E = \begin{bmatrix} 0.42 & 0.01 & 0.01 \\ 0.01 & -0.13 & 0.05 \\ 0.01 & 0.05 & -0.12 \end{bmatrix} \quad F = \begin{bmatrix} 1.354 & -0.031 & -0.031 \\ 0.068 & 0.854 & 0.054 \\ 0.067 & 0.053 & 0.865 \end{bmatrix}$$

$$E = \begin{bmatrix} 0.37 & 0.05 & 0.03 \\ 0.05 & -0.12 & 0.05 \\ 0.03 & 0.05 & -0.11 \end{bmatrix} \quad F = \begin{bmatrix} 1.311 & -0.007 & -0.012 \\ 0.095 & 0.870 & 0.051 \\ 0.078 & 0.053 & 0.880 \end{bmatrix}$$

$$E = \begin{bmatrix} 0.42 & 0.06 & 0.08 \\ 0.06 & -0.15 & 0.03 \\ 0.08 & 0.03 & -0.10 \end{bmatrix} \quad F = \begin{bmatrix} 1.346 & -0.004 & 0.031 \\ 0.121 & 0.841 & 0.036 \\ 0.137 & 0.024 & 0.888 \end{bmatrix} \tag{3.15}$$

The inverse deformation gradients were calculated using matrix inversion. The first step was to recalculate what would be measured using DENSE and SENC if the image planes were shifted along the long axis and then tilted out of the R-C plane using expected values as measured for the healthy volunteer. As there are five breathholds, five sets of identical points representing voxel positions at the imaging time were used to reconstruct each of the five measurements from each breathhold. The layout of these points in the RCL coordinate system is demonstrated in Figure 3.12.

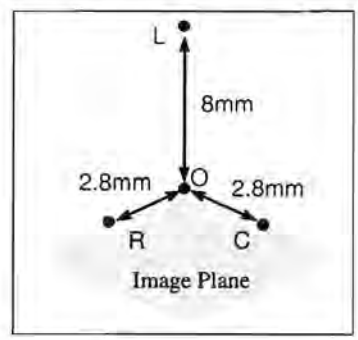

Figure 3.12: Separation of points at imaging time used in reconstruction.

For each of the five sets, a normally distributed random displacement in the long axis was calculated using a standard deviation as measured in the

volunteer data. A tilt was added to the long axis in order to tilt the points in the R- and C-axis out of the image plane with a normally distributed angle and a standard deviation as inferred from the volunteer data. This tilt was applied in a direction randomly chosen between 0 and 2π with a linear distribution. It was assumed that the shift of the myocardium within the image plane were corrected using 2D correlation of the images so that no random displacement in the R-C plane was accounted for. The first set of points for the first breathhold, however, had no random displacement or tilt added to it, as this data set is imaged at the desired slice, with the other data sets being acquired with inaccuracy about it.

These five sets of displaced points were mapped back to their positions at the beginning of the cardiac cycle, using the inverse deformation gradient, and the added random shifts and tilts were removed so as not to include them in the DENSE or SENC measurement. The DENSE measurement was simply the change in displacement in the R or C directions of the relevant points. The in plane SENC measure was recalculated using the change in through plane displacement between the central point and the two points in the R and C-axes, multiplied by the encoding frequency (set at 0.15cyc/mm for this exercise) and divided by the in plane point separation of 2.8mm. The through plane SENC frequency was calculated as the change in separation of the two vertically adjacent points multiplied by the encoding frequency (0.15cyc/mm).

From the recalculated DENSE and SENC measures the deformation gradient was recalculated using the method outlined previously for calculating strain using a combination of both cine-DENSE and cine-SENC data.

This model of through plane slice variability was repeated 5000 times for each of the 12 deformation gradients. The value of the input strain tensor was scaled by the values [0.1 0.2 0.3 0.4 0.5 0.6 0.7 0.8 0.9 and 1] for every 500 repetitions. The aim of scaling the strain tensor is to understand the effect of the strain magnitude on the error. For each calculation of strain, a measure of the strain error was determined by subtracting it from the strain calculated from the input deformation gradient. For each set of 500 repetitions a root mean square (RMS) error was calculated.

This same model was used to estimate the error or noise introduced into the calculation of a 3D strain tensor using 3D DENSE data. An extra set of points was added to the model (ie. six sets of points) in order that six DENSE measurements could be determined to include the effects of

through plane variability. The 3D strain tensor was recalculated in the manner described above and the RMS error for each set of 500 repetitions was determined.

3.4.3 Estimate of the strain error resulting from noise in the kinematic measurements

An estimate was obtained of the noise introduced into the strain tensor due to errors in the DENSE and SENC measurements in a similar way to the methodology described previously to investigate the effects of through plane myocardial position variability. The aim of the simulation was to add expected noise to reconstructed measurement values and then recalculate the strain. The purpose of this is to obtain an estimate of the strain error using the proposed combination of DENSE and SENC MRI.

A measure of the cine-DENSE displacement error was necessary to perform such a simulation. A data set where two CSPAMM acquisitions were performed in the same breathhold with the same encoding had been previously acquired at UVA for a healthy volunteer. This data set was acquired for both the X_1 and X_2 encoding directions. The phase of one CSPAMM data set was subtracted from the phase of the other and the resultant phase was unwrapped using the CineDenseAnalysis3D software. The displacement was calculated from this phase and a differential error was calculated for each pixel with the pixels arranged as demonstrated in Figure 3.13, where the

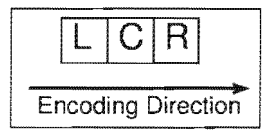

Figure 3.13: Average differential displacement pixel arrangement.

displacement of C was subtracted from L and that of R from C. The average yields a differential displacement error. This was performed in the encoding direction for both the X_1 and X_2 data and the standard deviation for the differential displacement of the myocardium was calculated from the combination of the X_1 and X_2 calculations. The reason for computing the standard deviation of differential displacement rather than that of displacement is that the component of the error common to neighbouring pixels is removed.

The four points illustrated in Figure 3.12 were deformed during the simulation using one of twelve inverse deformation gradients as calculated in the previous section (3.4.2). DENSE and SENC measures were reformulated from the deformation of these points in a manner similar to that described previously. Noise was first added to the through plane SENC measurement by adding to its magnitude Gaussian distributed noise with a standard deviation of 1.5% of the encoding frequency. This value was based on the 1.5% RMS error reported by Osman *et al* (2001). Gaussian distributed random noise was added to the in plane component of the SENC vector using a standard deviation as calculated from the above differential displacement measurement for DENSE error and scaled from mm to tag frequency by multiplying by the encoding frequency and dividing by the voxel width. This magnitude of error was based on the fact that the in plane component of the SENC vector is calculated from the change in phase between neighbouring pixels with the phase being equivalent to a DENSE displacement measure.

Before noise was added to the DENSE measures, the X_1 and X_2 components of the three non-coplanar vectors, as used in the strain calculation, were first determined. Gaussian distributed random noise, computed from the differential displacements, was added to these values. The strain was then calculated using the method described above.

This experiment was repeated 5000 times for each of the 12 deformation gradients. The value of the input strain tensor was scaled by the values [0.1 0.2 0.3 0.4 0.5 0.6 0.7 0.8 0.9 and 1] for every 500 repetitions. The error in the recalculated strain tensor was calculated as the difference between the strain tensor calculated from the input deformation gradient and the recalculated strain tensor. An RMS error was calculated for each group of 500 simulations and from this the relationship between the strain error and the magnitude of the strain was formulated.

To investigate the proportion of measured noise as a result of the DENSE measures, this experiment was repeated with the standard deviation of all cine-DENSE noise set to 0.

3.5 Deformation visualization techniques

Four visualization techniques were implemented, three of them visualized the intramyocardial strain, and one visualized the deformation gradient.

The first technique is a simple colour map where individual components of the tensor are mapped to the colour of the pixel. Strains were mapped to the RCL coordinate system to ensure uniformity of the measure around the myocardium.

The second technique visualized the strain by performing eigenvector decomposition on the strain tensor. Each eigenvalue is displayed on a separate colour map depicting the magnitude of each principal strain with the orientation of the corresponding eigenvector depicted by a 3D line vector across the location of strain on the colour map. The eigenvalues were sorted from most negative (first principal strain) to most positive (third principal strain).

The last strain visualization technique mapped the strain tensor onto the shape, size and colour of a glyph. A superquadratic glyph convention proposed and outlined by Ennis *et al* (2005) was used. Essentially the anisotropy between the three eigenvalues are displayed using the glyphs roundness. The shapes are defined as explained in Section 2.5 with the glyphs displayed in the myocardial position where the strain was calculated. Each glyph was scaled along its axes by the corresponding principal strain values, and orientated in the respective eigenvector directions with the surface colour corresponding to the most negative principal strain.

The deformation gradient visualization technique displays a cube deformed by the deformation gradient of interest. In this manner a field of deformation gradients can be visualised on different frames.

All of the techniques were collated into a Matlab GUI that controls the generation of figures, what type of visualization technique is utilized, and which strain component is displayed on each. It also allows the user to select which cine frame to display. This GUI is shown in the figure below:

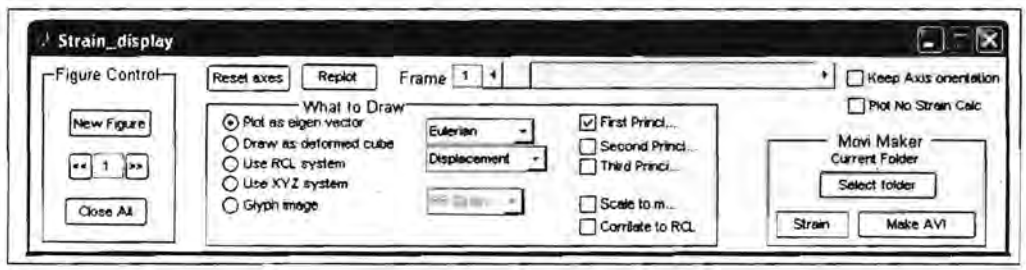

Figure 3.14: Strain display GUI, Matlab.

Chapter 4

Results

4.1 Fine Tuning SENC Parameters

The aim of the tuning process was to find the appropriate SENC encoding gradients, unencoding gradients and slice thickness. This process involved investigating the relationships between slice thickness, the frequency profile of the slice, and the SNR using both phantom and human data.

4.1.1 Results of phantom investigations

The phantom was encoded at a frequency *ke* and unencoded at several different unencoding values about *ke*. Figure 4.1A is a plot of the signal magnitude as a function of the difference between the unencoding gradient and *ke* for an 8mm slice for selected cine imaging frames. As expected, frame 18 has the lowest signal magnitude and shortest distance between its first two minima with a separation of 0.11cyc/mm.

Figure 4.1B is a plot of the frequency profile for a slice thickness of 11mm for the same cine imaging frames. Frame 18 again has the shortest distance between its first two minima that are separated by 0.095cyc/mm.

Figure 4.1C shows the results for a 14mm slice thickness. The width between the two minima of frame 18 is reduced to 0.06cyc/mm.

Figure 4.1D demonstrates the frequency profile for a 16mm slice thickness. The separation of the first two minima for frame 18 is now 0.055cyc/mm. The smallest unencoding frequency imaged in this experiment was 0.115cyc/mm

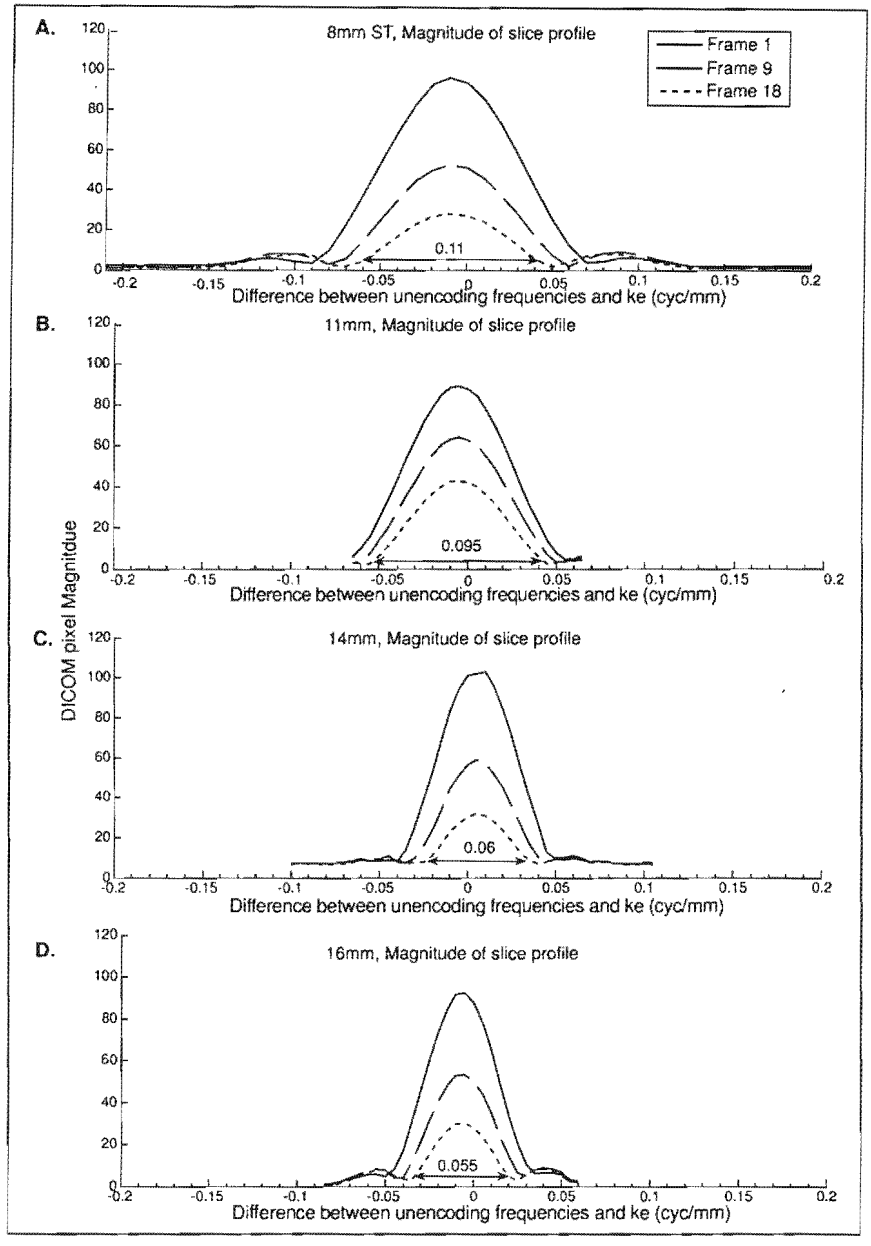

Figure 4.1: Frequency profiles for slice with a slice thickness of 8mm (A), 11mm (B), 14mm (C) and 16mm (D). The pixel magnitude is plotted against the difference between unencoding and encoding value. Profiles are shown for cine frames, 1, 9 and 18. Each was encoded at (A) 0.4cyc/mm (B) 0.2cyc/mm (C) 0.4cyc/mm and (D) 0.2cyc/mm.

(Figure 4.1D), which demonstrates that there is no observable interference from the T1 echo at such a low frequency.

Variations of the shape of the frequency profile with cine phase include decreased magnitude for later cine phases, shorter distances between the first two minima, and wider side lobes.

The difference between the signal observed in a phantom compared to myocardium was explored by scanning both the phantom and a healthy volunteer with the same DENSE encoding parameters. The SNR was calculated using

$$SNR = \frac{MeanSignal}{\sigma_{noise}} \tag{4.1}$$

in which σ_{noise} is the standard deviation of the background noise. In the phantom the SNR was found to be 27.4 compared to a value of 16.7 for the SNR of the myocardium.

4.1.2 Human SENC parameter optimization

When imaging a phantom different outcomes are obtained to that when imaging myocardium. It was therefore necessary to image several volunteers to understand the effects of different imaging parameters and select the set of parameters that provide the most optimal images to demonstrate the SENC effect. Volunteers were imaged according to the parameters listed in Table 3.2.

Figure 4.2 shows images for an 8mm slice encoded at 0.4cyc/mm for two different unencoding frequencies. Important observations are that these images have low signal quality and demonstrate significant ghosting of the myocardium along the phase encode direction. Most importantly, it is observed that by frame five the signal of the myocardium has completely dephased for an unencoding gradient of 0.4cyc/mm and is not visible. Similarly, the signal of the myocardium has completely dephased by frame 12 for the series unencoded at 0.47cyc/mm. Figure 4.3 shows the results of repeating the exact same experiment with a readout FOV of 480mm. Although these images demonstrate a distinct improvement in the signal quality, they still suffer from the same myocardial ghosting along the phase encode direction.

Again and most importantly, the signal from myocardium has completely dephased in a number of frames for both image sets.

When imaging volunteer two, the encoding gradient was reduced to 0.2cyc/mm to allow a larger slice thickness for improved SNR. Figure 4.4 shows the images acquired for unencoding frequencies of 0.2cyc/mm and 0.235cyc/mm, respectively. This series of images demonstrates an increase in image or signal quality but substantial proportions of the myocardium still fade completely for several frames. For example, in frames 11 and 12 there are portions of myocardium that do not appear in either image set.

EPI artefacts can cause significant signal attenuation due to portions of the myocardial signal being lost in the ghost image. This is serious for SENC imaging where the magnitude of the image is used to compute the kinematic data. Two volunteers were imaged to find the optimal configuration of EPI parameters. An encoding frequency of 0.2cyc/mm and unencoding frequencies of 0.2 and 0.24cyc/mm were used. The two EPI parameters that were varied were the echo train length (ETL) and the number of segments. Images were obtained for the following configurations: ETL(Segments) 7(14), 5(10), 9(9), 9(18) and 15(15). Selected images, roughly at end systole, are shown in Figure 4.5 where particular artefacts are highlighted with a white box around them. The one configuration which demonstrates robustness towards EPI artefact is the 9(9) configuration. However, due to the halved number of segments, this configuration takes double the number of heart beats to acquire as compared to a 9(18) configuration.

The EPI configurations of 7(14), 5(10) and 9(18) all demonstrate significant myocardial ghosting that can be present in multiple frames. The 15(15) configuration, however, does not present such ghosting but instead greater signal inhomogeneity and tissue distortion.

Thus if no reference image was to be acquired a 9(9) EPI configuration will yield the best results. Since we would like to obtain the SENC measurement and a phase reference image in a single breathhold, the 9(18) EPI configuration was selected for this study. Typically, only the first few frames are affected by the ghosting artefact.

After observing in Figure 4.4 that portions of the myocardium completely fade from the image, it was decided to reduce the encoding gradient to 0.15cyc/mm. Images acquired of volunteer five are shown in Figure 4.6. In

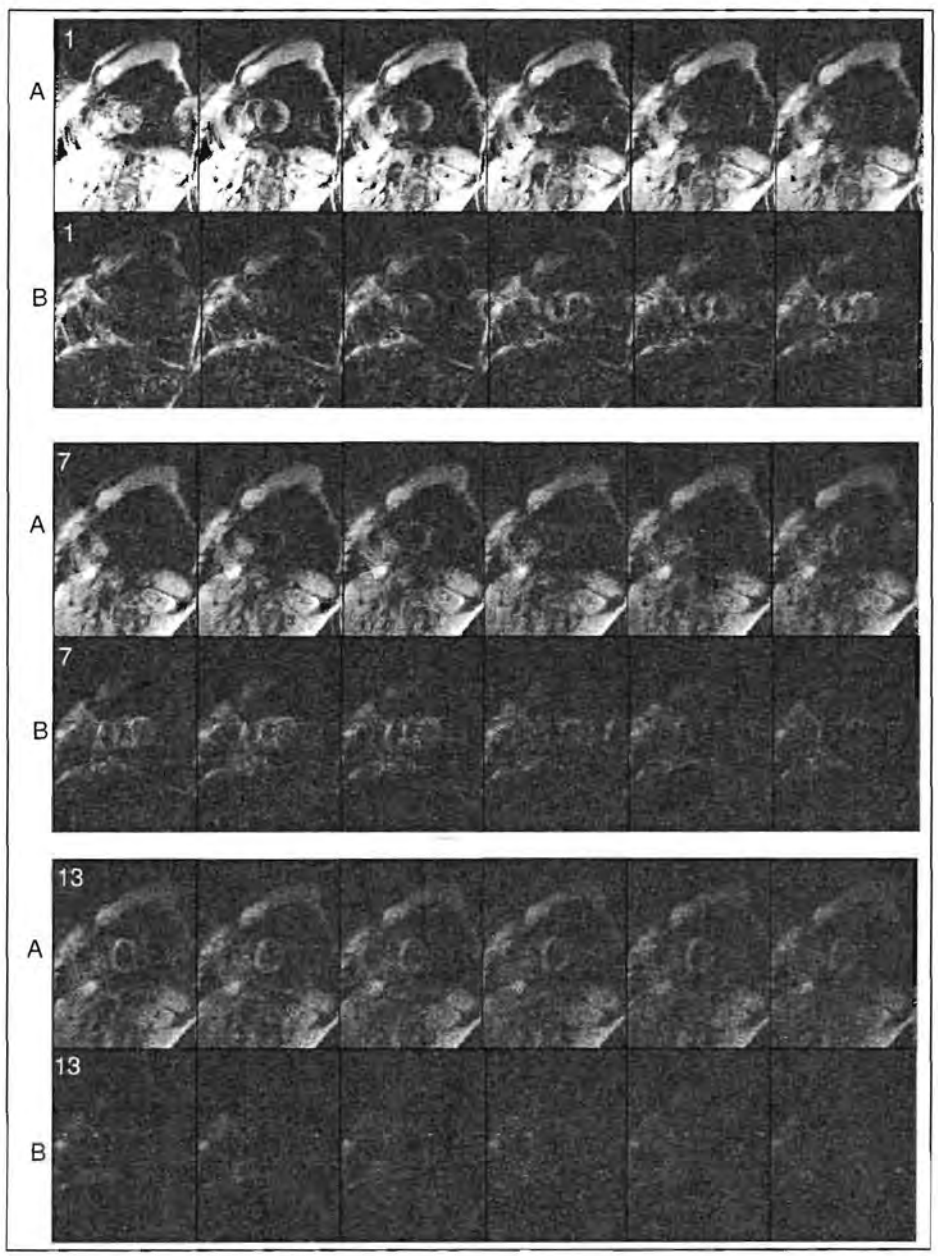

Figure 4.2: Volunteer 1, encoded at 0.4cyc/mm with readout FOV = 360mm and slice thickness 8mm. Image set A is unencoded at 0.4cyc/mm and image set B is unencoded at 0.47cyc/mm.

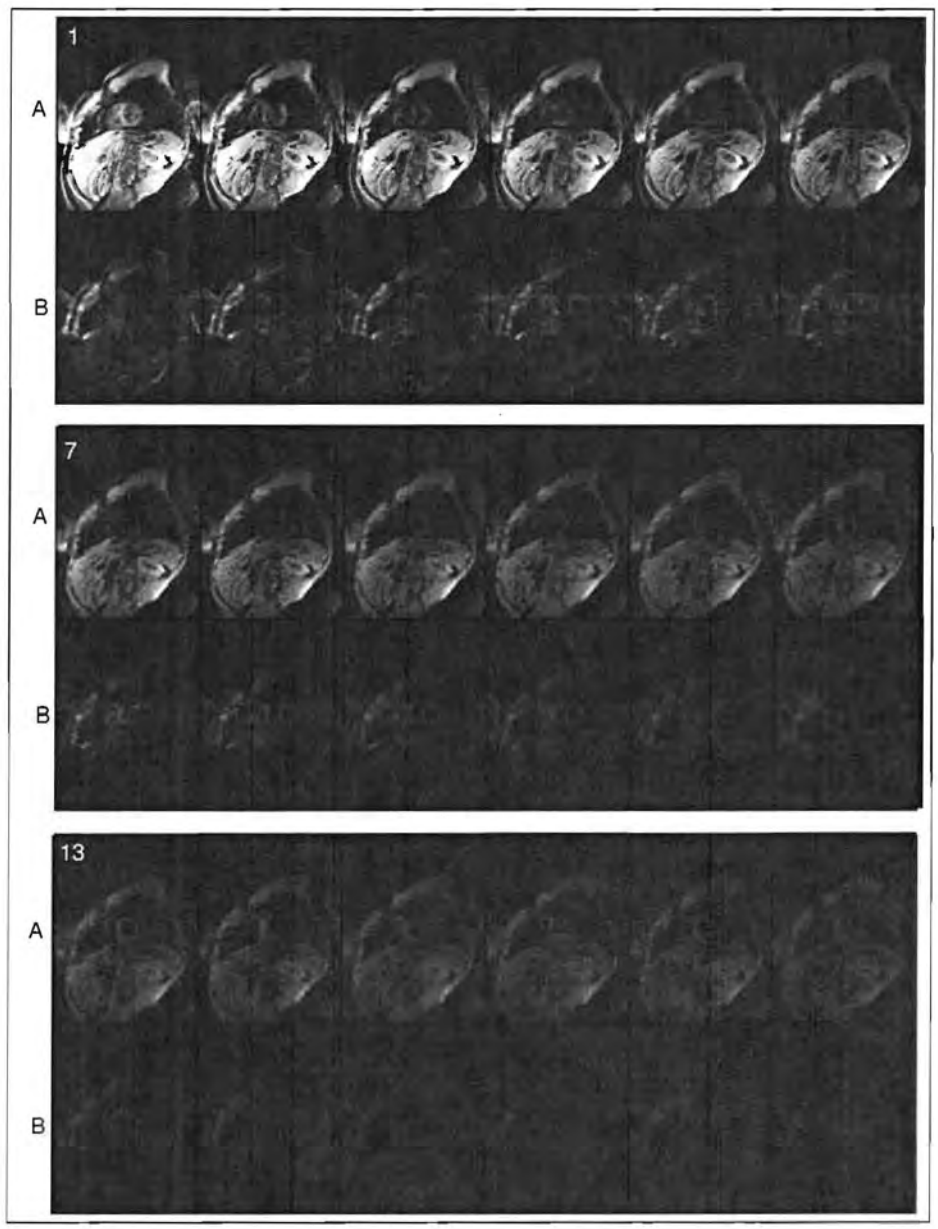

Figure 4.3: Volunteer 1, encoded at 0.4cyc/mm with readout FOV = 480mm and slice thickness 8mm. Image set A is unencoded at 0.4cyc/mm and image set B is unencoded at 0.47cyc/mm.

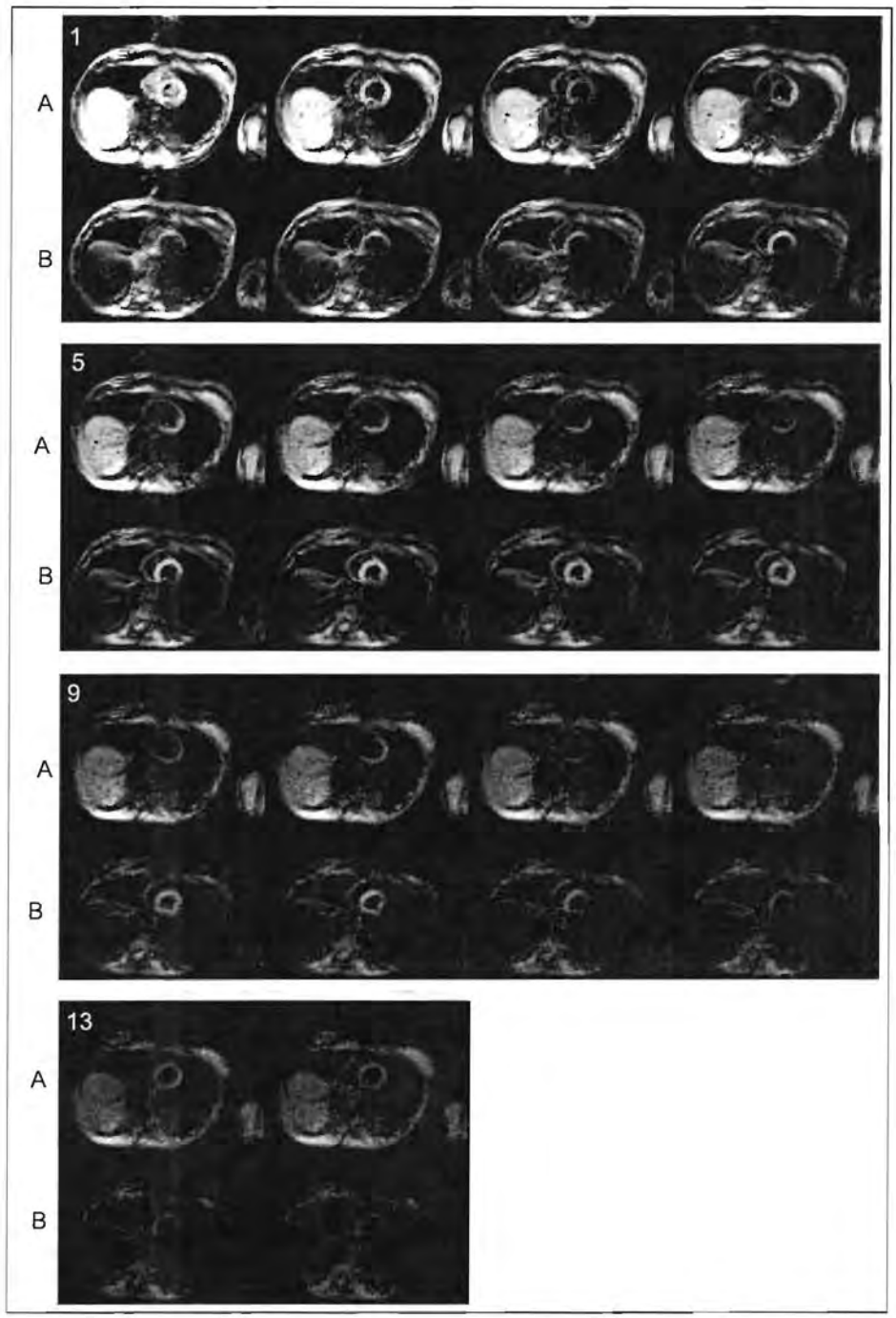

Figure 4.4: Volunteer two. Encoded at 0.2cyc/mm and unencoded at 0.2cyc/mm (set A) and 0.235cyc/mm (set B), respectively. Readout FOV is 360mm, 16mm slice thickness. The cine frame is indicated for the first frame in each row.

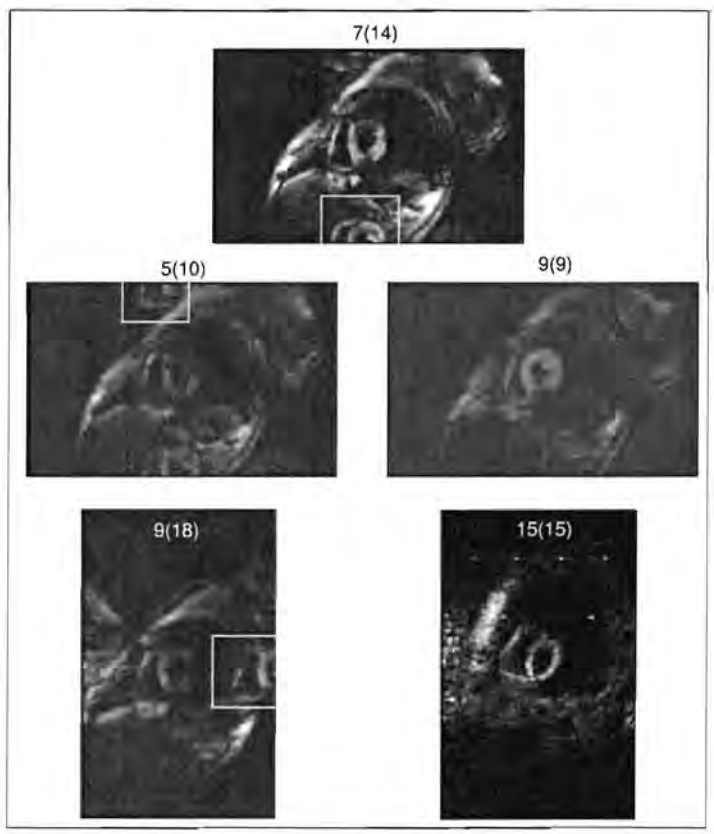

Figure 4.5: Images acquired using EPI configurations with different echo train lengths and different numbers of segments. In the above images the ETL and segments are specified using the notation ETL(Segments). All of the above images were acquired for volunteer 3 except for the 15(15) acquisition of volunteer 4. The artefacts are highlighted with square white boxes.

this figure the EPI ghosts are present in frames 1, 2 and 3 but absent in later frames.

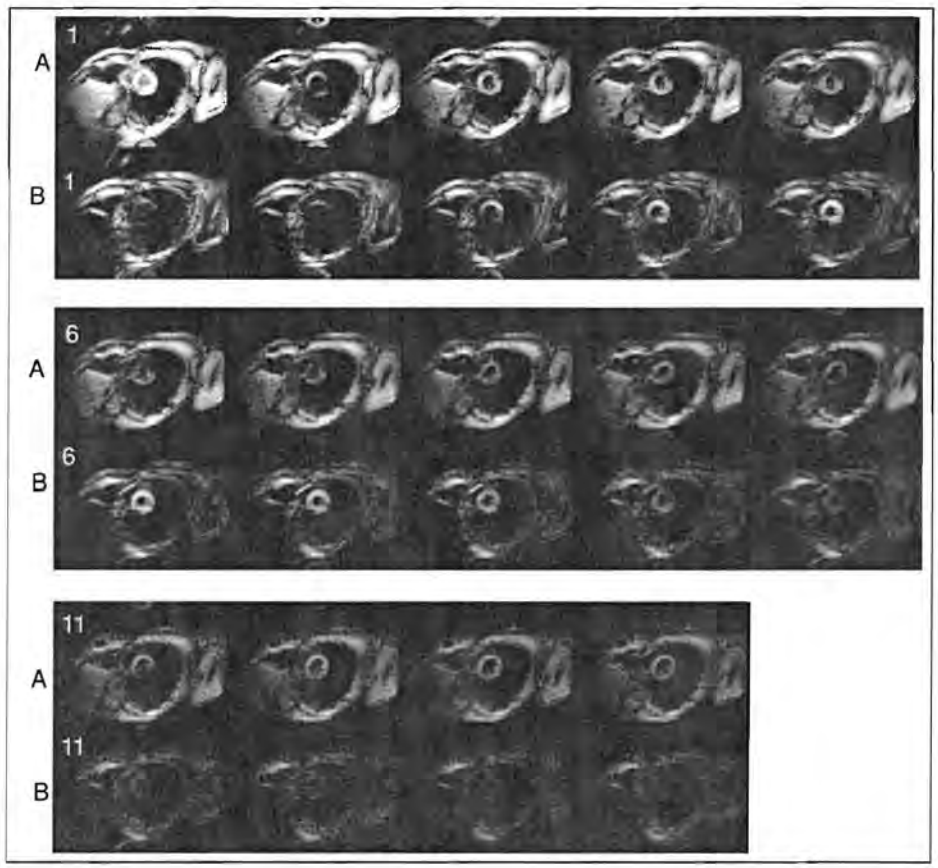

Figure 4.6: Volunteer 5 with 0.15 cyc/mm encoding, and 0.15 cyc/mm (set A) and 0.185 cyc/mm (set B) unencoding frequencies, respectively. Slice thickness is 16mm, readout FOV is 480mm, and ETL and segments are 9 and 18, respectively.

4.2 Image Processing and strain computation

The image processing and strain computation was performed in Matlab on an AMD 2500 processor with 512MB of RAM. After the myocardium was segmented with contours that are satisfactory for all acquisitions (DENSE and SENC), cine-DENSE processing was performed. This includes phase unwrapping and tracking and takes 77 seconds for a volunteer with 18 cine

phases. The calculation of the SENC vectors takes 2.5 seconds and the strain calculation a further 21.2 seconds. The temporal resolution of both cine-DENSE and cine-SENC is 44ms.

4.2.1 Colour map strain visualization

The normal and shear strains projected onto the radial, circumferential and longitudinal axes are presented for volunteer three. Figures 4.7, 4.8 and 4.9 depict the normal strains in the circumferential, radial, and longitudinal directions, respectively. Figure 4.10, Figure 4.11 and Figure 4.12 depict the circumferential radial, radial longitudinal, and circumferential longitudinal shear strains, respectively.

In Figure 4.7 a number of distinct outliers occur where a pixel of red appears amongst blue pixels. Despite these outliers, the circumferential strain is predominantly smooth. Removing these outliers from the calculation, the mean strain for the end systolic frame (8) is -0.17 with a standard deviation of 0.07. Circumferential shortening (squared) is demonstrated through the cycle with a gradual increase from zero strain to a maximum strain at end systole and then returning to a very low, but noisy strain at mid diastole. Clearly the noise levels increase as the cardiac cycle progresses.

In Figure 4.8, the radial strain, or radial thickening squared, is demonstrated. Non-uniform patterns of strain are observed for frames 4 to 11 with some regions having very little strain compared to large strain in other areas. There is no common transmural variation. Some regions have larger endocardial strain and others have larger epicardial strain. The increase in noise levels in this data is observed in the large variability of the data. There are two very large outliers in the end systolic frame (8) with strain values of 107 and 322, respectively, whereas the remainder of the strain values have magnitudes ≤ 1 . Outliers depicting a radial strain greater than 0.8 were removed providing a mean end systolic strain of 0.32 and standard deviation of 0.19.

In Figure 4.9 the strain in the longitudinal axis (through the image plane) is depicted. This strain measure is very smooth with very few outliers and little visual noise. It should be noted that the range of the colour map has been reduced in this figure to a range of -0.25 to +0.25 as strain through the plane is significantly lower than the radial and circumferential normal strains. After removing outliers with strains greater than zero, the mean end

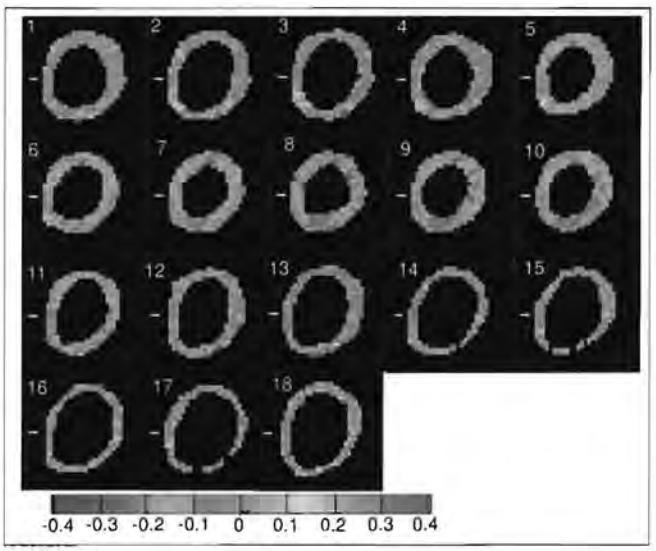

Figure 4.7: Colour map of circumferential strain for volunteer 3. White arrows indicate the septum and the numbers are the cine frame number. The scale is given at the bottom.

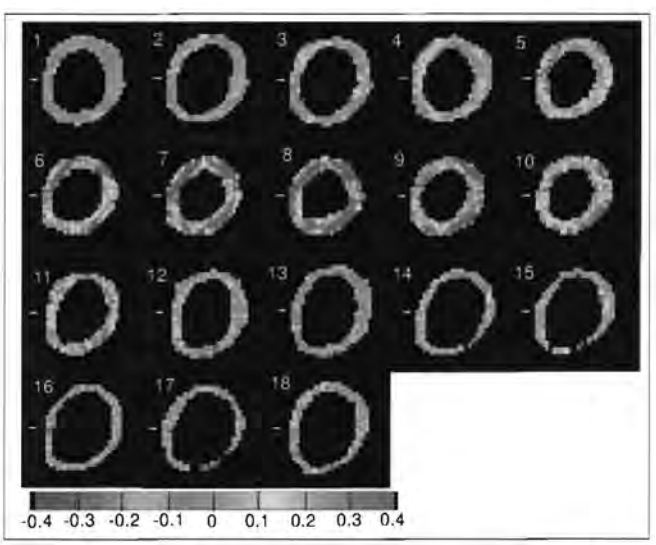

Figure 4.8: Colour map of radial strain for each cine frame. A White arrow indicates the position of the septum. Frame numbers are given and a colour bar shows the colour mapping.

systolic strain was -0.10 with a standard deviation of 0.03. The progression of longitudinal shortening (squared) through the cardiac cycle can be observed with peak strains occurring in frames 8 and 9. It should be noted that in the inferior wall (at the bottom right of the myocardium) the increase in longitudinal strain is delayed and starts appearing only after frame 8 while strain for other areas peaked at this frame.

Figure 4.10 depicts the circumferential radial shear strain that peaks in frame 8. A negative, positive, negative, positive pattern (starting at the septum in a clockwise traversal) is predominant through the cycle; this pattern was observed in three of the four volunteers. The last few frames (15 to 18) exhibit a scatter of strain values with no clear regional pattern. A maximum end systolic shear strain of +0.35 was calculated (excluding outliers) with a minimum of -0.36 (excluding outliers).

Figure 4.11 visualises the radial longitudinal shear strain. The peak shear strain again occurs in frame 8. Although regional patterns of shear strain are observed, these patterns are not the same throughout the cardiac cycle or between volunteers. The maximum end systolic shear strain was 0.32 with a minimum of -0.2. For the volunteer data displayed below,regions of shear strain greater than the background noise levels persist into frame 16.

Figure 4.12 displays the circumferential longitudinal shear strain and demonstrates clearly regions of negative shear strain with one or two inconsistent positive regions. A peak positive end systolic shear strain of 0.08 (excluding outliers) and a minimum end systolic shear strain of -0.22 (excluding outliers) were calculated. Regional patters of shear strain can be observed for all frames.

Tables 4.1 and 4.2 list the mean and standard deviation, respectively, of the normal strains at end systole for the four volunteers for whom images required for strain calculation were acquired.

Table 4.1: Mean normal end systolic strain.

	Volunteer 1	Volunteer 2	Volunteer 3	Volunteer 4
Radial	0.40	0.32	0.32	0.32
Circumferential	-0.18	-0.17	-0.17	-0.15
Longitudinal	-0.07	-0.11	-0.10	-0.06

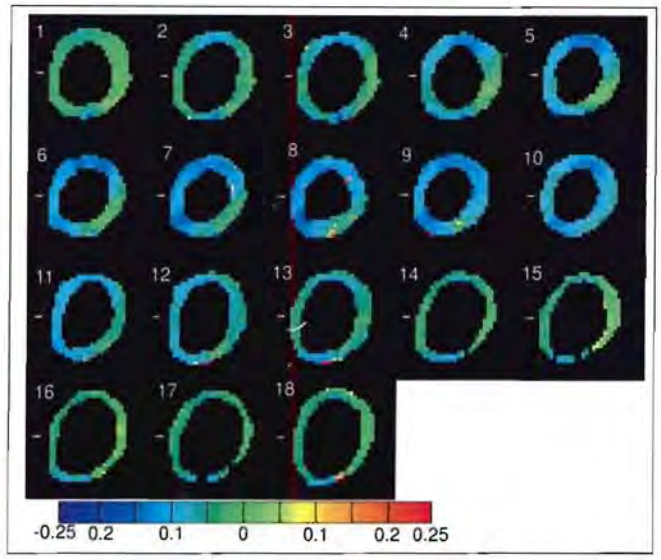

Figure 4.9: Colour map depicting longitudinal strain for each cine frame. Frame numbers are given as well as a colour bar depicting the colour map used.

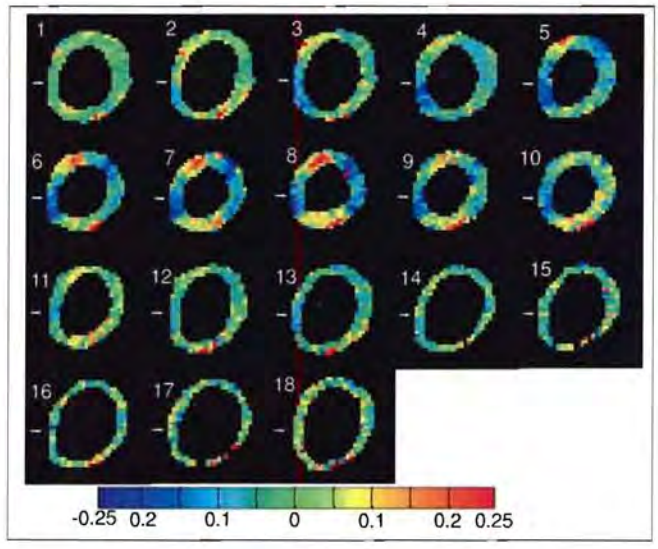

Figure 4.10: Colour map of radial circumferential shear strain for each cine frame. A white arrow indicates the position of the septum. Frame numbers and a colour bar depicting the colour mapping are given.

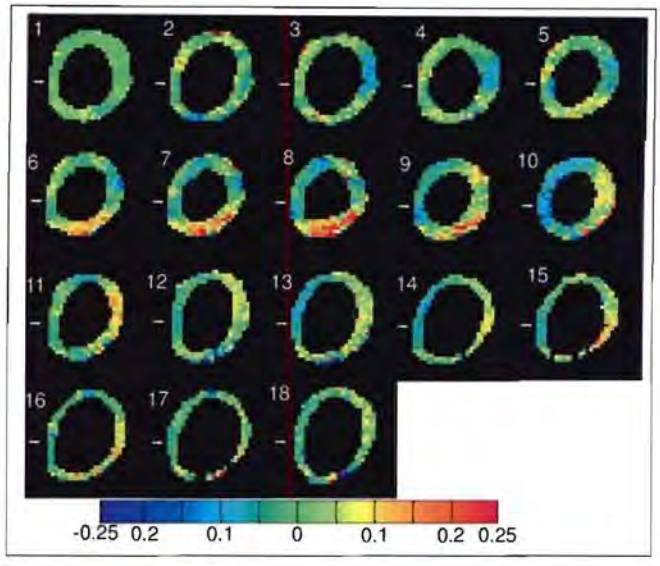

Figure 4.11: A colour map display of the radial longitudinal shear strain for all cine frames. A white arrow indicates the position of the septum. The frame numbers and a colour bar depicting the colour mapping are shown.

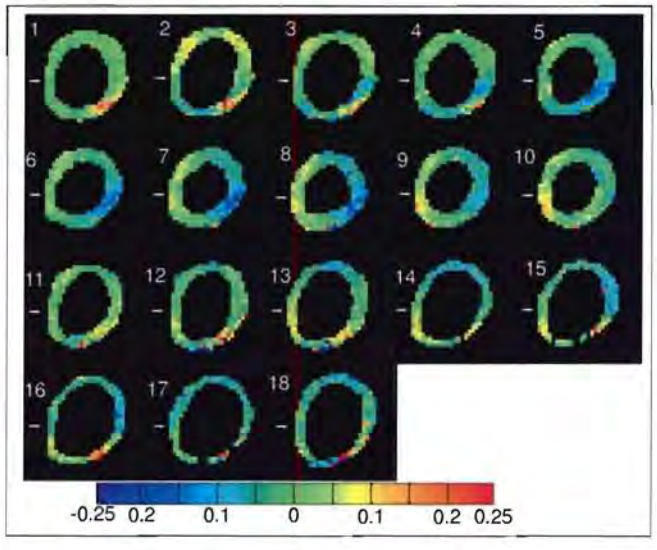

Figure 4.12: Colour map display of circumferential longitudinal shear strain for all cine frames. Cine frame numbers are specified and the position of the septum is indicated with a white arrow. A colour bar shows the colour mapping employed.

Table 4.2: Standard deviation of normal end systolic strain.

	Volunteer 1	Volunteer 2	Volunteer 3	Volunteer 4
Radial	0.20	0.2	0.19	0.19
Circumferential	0.07	0.06	0.07	0.06
Longitudinal	0.03	0.03	0.03	0.04

4.2.2 Principal strain visualization

The end systolic principal strains and directions, calculated from eigenvector and eigenvalue decomposition are depicted in figures Figure 4.13A, Figure 4.13B, Figure 4.14A and Figure 4.14B for volunteers one, two, three and four, respectively. The magnitude of the principal strain is depicted on a colour map projected onto a 3D slice and its direction by a bar displayed above the colour map. The principal strains were sorted from most negative (first principal strain) to most positive (third principal strain). These slices are orientated such that the apex is above the displayed slice (slice viewed from apex).

These maps demonstrate clearly the regional uniformity of the magnitude of the principal strain. The first principal strain has a distinct circumferential component with a longitudinal contribution. The images below are viewed from apex, looking towards the base, and the first principal strain vectors appear to predominantly be part of a anti-clockwise spiral from the apex to the base. The most non-uniform data is obtained for the third principal strain that is orientated within the image plane in a radial direction.

The second principal strain is predominantly orientated in the longitudinal direction with a circumferential component and smaller magnitude than the first principal strain. This strain predominantly forms a clockwise spiral from the apex to the base (note the images are viewed from the apex). A few second principal strain vectors form part of the spiral predominant in the first principal strain, and where this occurs, the first principal strain forms part of the spiral predominant in the second. This tends to occur where the two principal strains have a similar magnitude.

4.2.3 Visualization of the deformation with cubes

The deformation gradient was visualised by mapping a cube (at end diastole) to its shape at the imaging time. Figure 4.15 depicts the myocardium

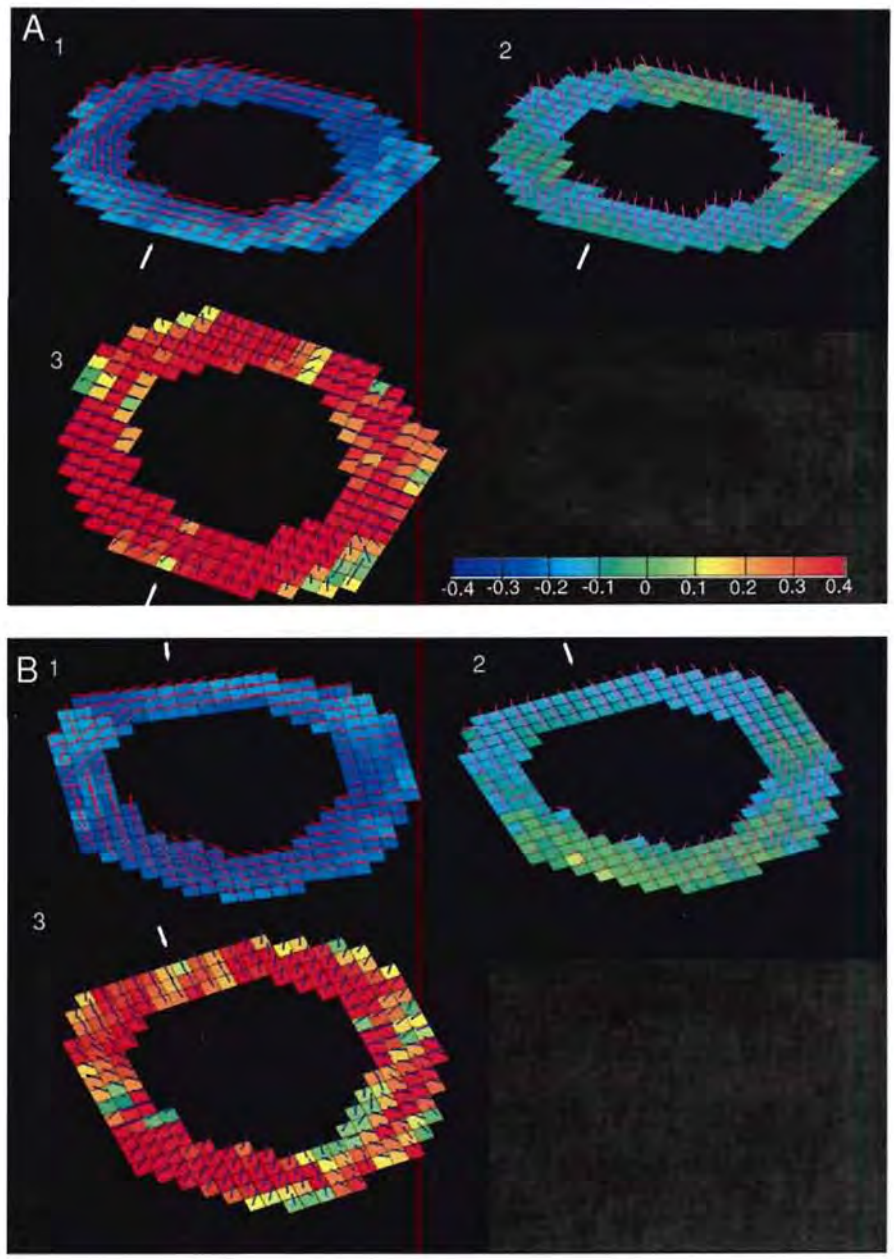

Figure 4.13: Magnitude and direction of the first, second and third principal strains for volunteer one (A) and two (B). The magnitudes of the principal strains are displayed on a colour map and the directions with a line segment. The position of the septum is indicated with a white arrow and a colour bar shows the colour mapping.

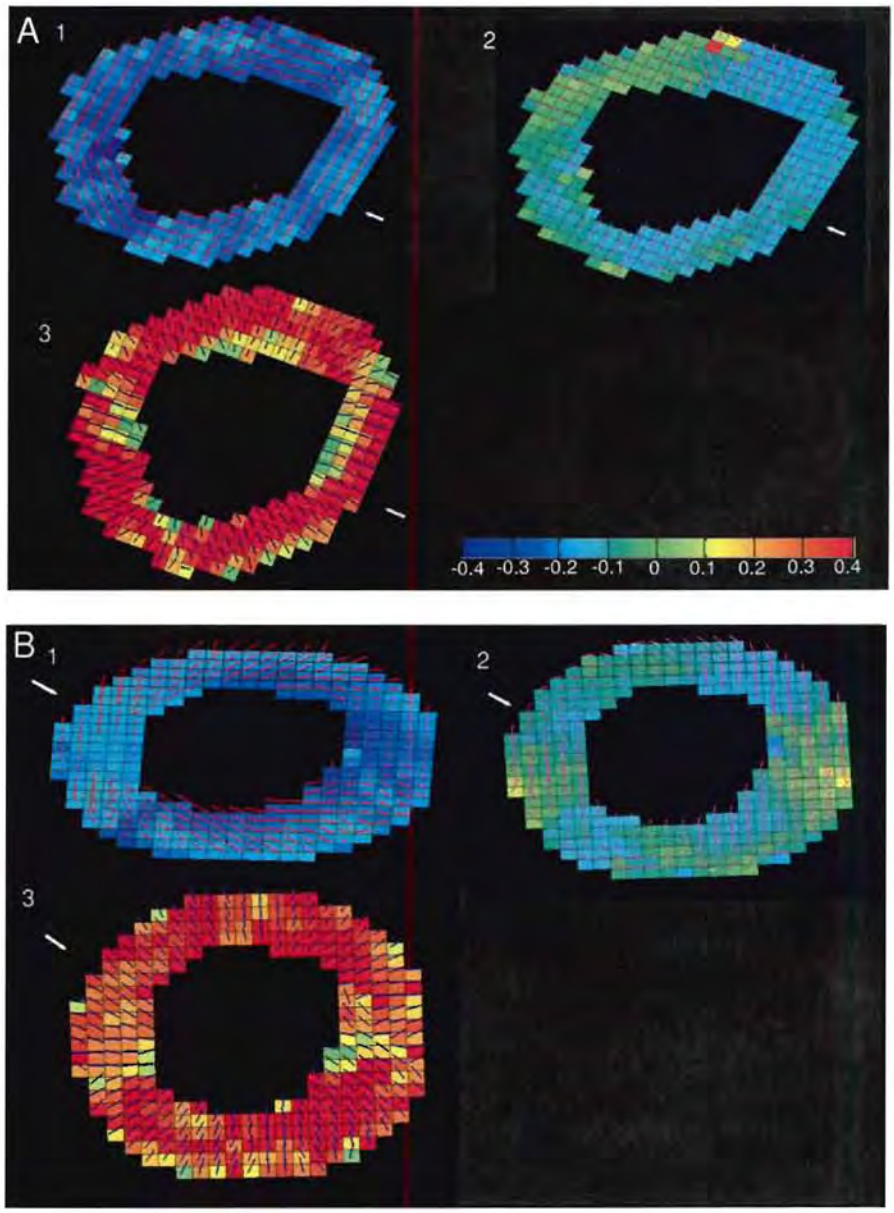

Figure 4.14: Magnitude and direction of the first, second and third principal strains for volunteer three (A) and four (B). The magnitudes of the principal strains are displayed on a colour map and the directions with a line segment. The position of the septum is indicated with a white arrow and a colour bar shows the colour mapping.

as fields of such deformed cubes for four cine frames as computed using data acquired at the imaging time. The cubes depict how the myocardium deforms in the three imaging axes. The change in length of each edge of a cubes frame depict the linear normal strains. The degree of distortion of a face from rectangular to non-rectangular yields a measure of the shear strain. In the end systolic frame (6) the cubes are seen to stretch in the radial direction and become thinner in the circumferential and longitudinal directions. When the in plane axes of the cube are not aligned with the radial or circumferential directions its in plane face becomes diamond shaped. This demonstrates radial thickening and circumferential shortening. In the last cine frame the cubes have largely returned to their original shape.

4.2.4 Glyph images of strains for healthy volunteers

Glyph images were produced for each of the four volunteers. Glyphs are shown for frames 1, 5, 8 and 13 for volunteer 2 in Figure 4.16. In frame 1 the glyph values are negligible, demonstrating small strain magnitudes. The strains peak at end systole (frame 8 for the series shown) and decrease again as the cardiac cycle proceeds into diastole. The mid diastolic frame (13) demonstrates significant fluctuation in glyph values, particularly in the radial direction.

End systolic glyphs are shown for volunteer one, three and four in Figure 4.17, Figure 4.18 and Figure 4.19, respectively. Fluctuations in the size of the glyphs, particularly in the radial direction, highlight inconsistencies in the calculated myocardial strain magnitudes. The shape of the glyphs in the circumferential longitudinal direction are generally rounded, demonstrating a degree of transverse isotropy between these axes, which is consistent with the circumferential longitudinal shear strain having a small magnitude. The magnitude of the first principal strain (most negative) is mapped to the glyph colour. It is evident that the radial normal strain is in general larger than the circumferential strain, since the components of the the glyphs in the radial direction are significantly larger than in the circumferential direction.

4.2.5 Calculating 3D strain from DENSE trajectories

Two adjacent sets of 3D motion trajectories calculated from cine-DENSE data were acquired with the two imaging planes separated by 2.8mm for volunteer one. The strain tensor at end systole mapped to the radial, cir-

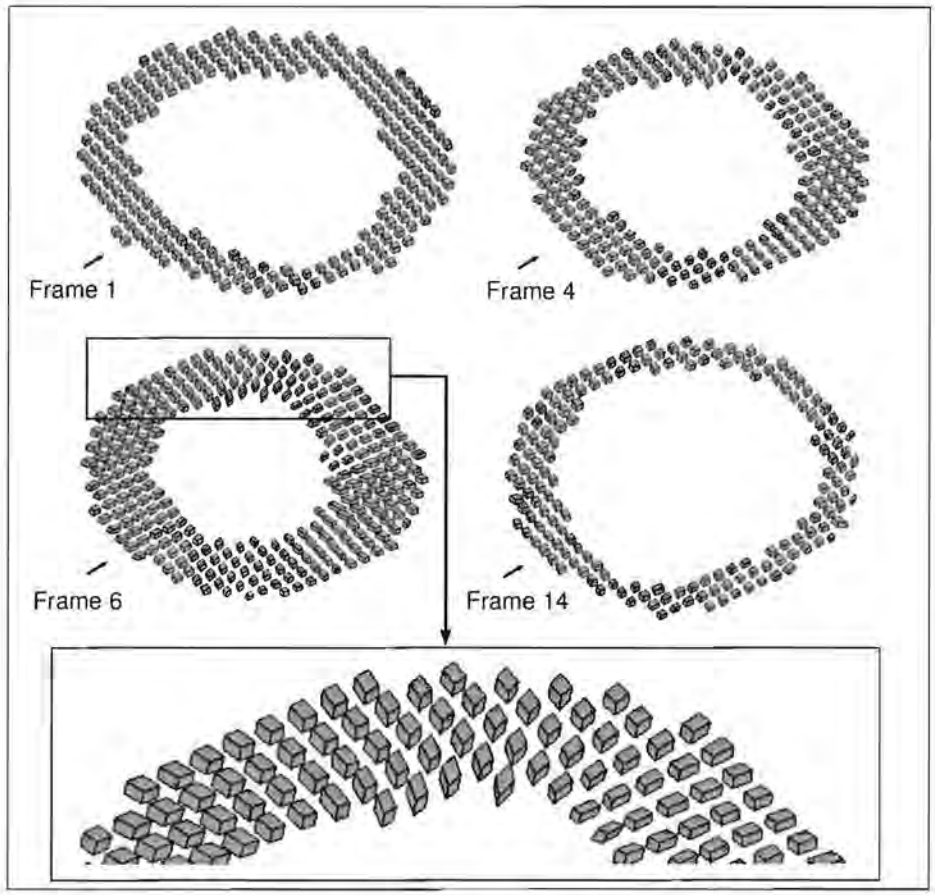

Figure 4.15: Cubes situated at pixel centres of the myocardium depict the deformation gradient at their location for volunteer 4. The three axes of the cube, at the start of the cardiac cycle, correspond to the three imaging axes and the axes of the deformation gradient. Frame 6 is acquired at end systole.

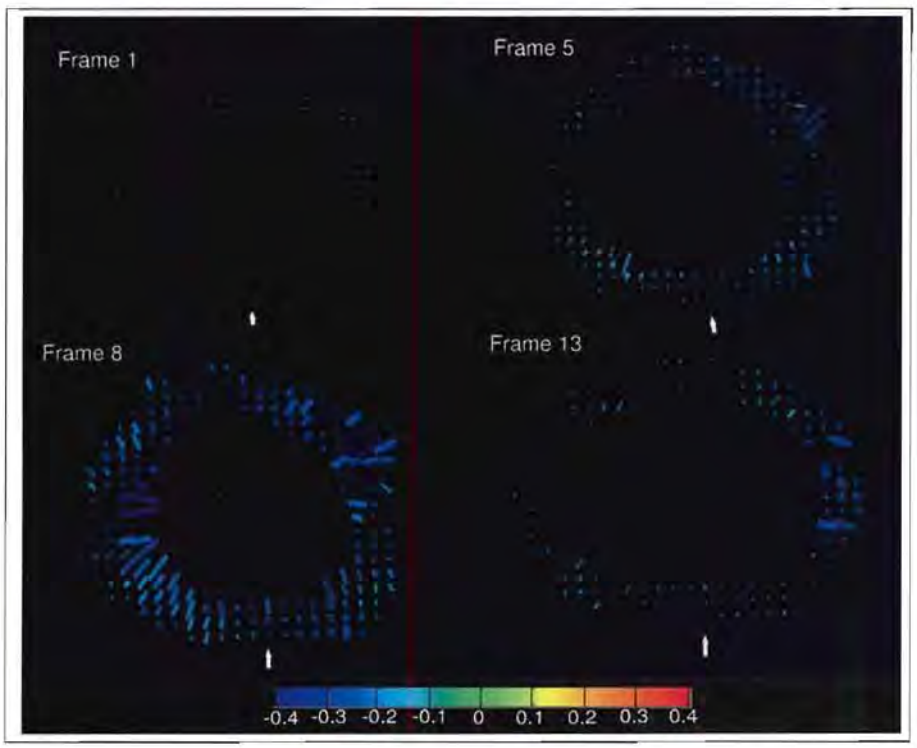

Figure 4.16: Glyph visualizations of strain for volunteer two. Glyphs are drawn for frames one, five, eight, and thirteen. The magnitude of the first principal strain is mapped onto the glyph colour and a white arrow indicates the position of the septum.

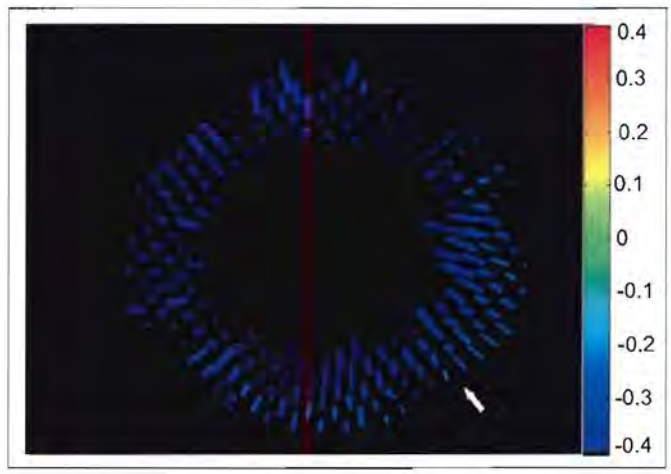

Figure 4.17: End systolic glyph visualization for volunteer one. The colour depicts the first principal strain and a white arrow indicates the position of the septum.

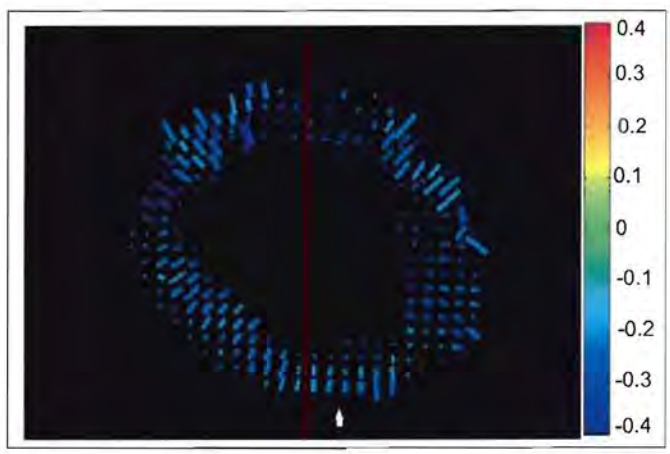

Figure 4.18: End systolic glyph visualization for volunteer three. The colour depicts the first principal strain and a white arrow indicates the position of the septum.

Figure 4.19: End systolic glyph visualization for volunteer four. The colour depicts the first principal strain and a white arrow indicates the position of the septum.

cumferential and longitudinal coordinate system is demonstrated in a colour map in Figure 4.20. The significant inaccuracy of the normal strain in the longitudinal direction is evident in bands of measured positive strain (red) in this measure as well as the presence of large (absolute value >0.3) radial longitudinal shear strains.

4.2.6 Calculating 2D strain from DENSE trajectories

This Matlab function is able to calculate the strain for any pixel on frame 1 at any specified time point between the first and last cine frames by using the DENSE trajectories. The circumferential and radial strains are demonstrated for 70% of the cardiac cycle in 10% increments in Figures 4.21 and 4.22, respectively. From these images one can observe how the strain for a segment of myocardium, as defined in the first cine frame, varies throughout the cardiac cycle. The myocardial map is the same for all frames.

Strains calculated using 3D motion trajectories were compared with those calculated from 2D motion trajectories. The purpose of this exercise was to demonstrate the resulting increase in magnitude of positive strains and reduction in magnitude of negative strains when using the 3D motion trajectories. To demonstrate this result strain time curves of the posterior free wall were plotted for the first and second principal strains (2D strain) computed

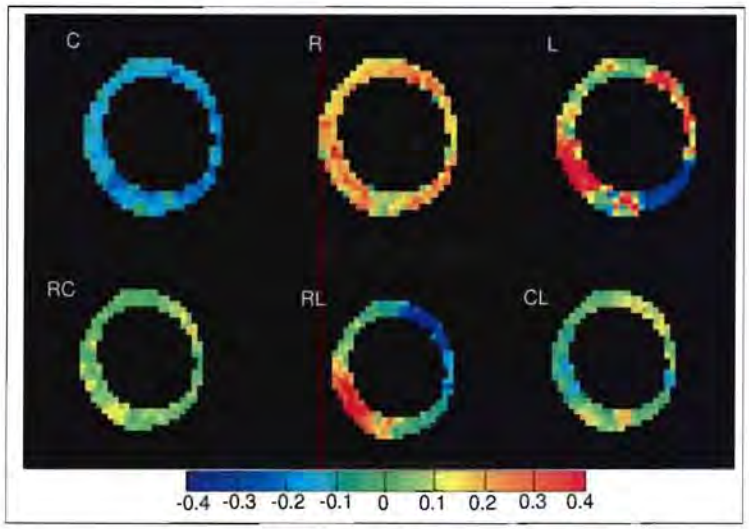

Figure 4.20: End systolic 3D strain calculated on volunteer one using two adjacent planes of 3D DENSE motion trajectories. R, C and L represents the normal strains in the radial, circumferential and longitudinal directions, RC the radial circumferential shear strain, RL the radial longitudinal shear strain and CL the circumferential longitudinal shear strain.

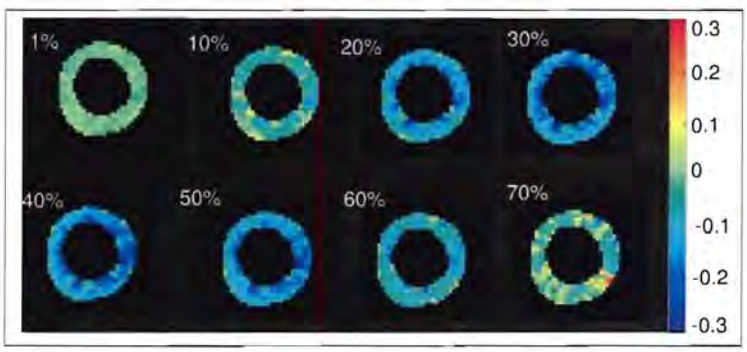

Figure 4.21: 2D Lagrangian circumferential strain for volunteer one calculated using 3D motion trajectories. Strain was measured at various times in the cardiac cycle and displayed on the myocardial map of the first cine frame (Lagrangian strain map).

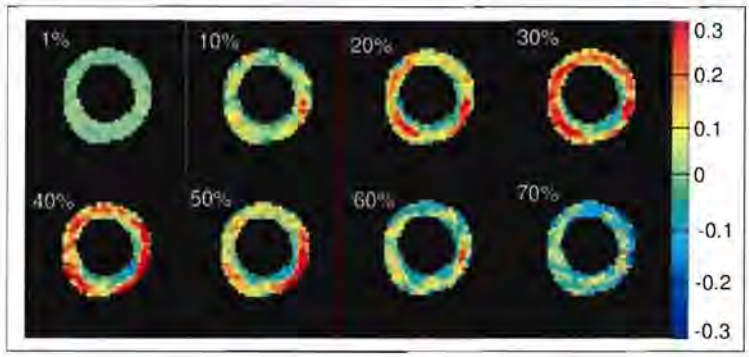

Figure 4.22: 2D Lagrangian radial strain for volunteer one calculated using trajectories of 3D motion. Strain was measured at various times in the cardiac cycle and displayed on the myocardial map of the first cine frame (Lagrangian strain map).

from both 2D and 3D motion trajectories. The reduction in magnitude for negative strains when using 3D motion trajectories is demonstrated in the plot of the first principal strains E1 in Figure 4.23. The principal strains are sorted from most negative to most positive. Figure 4.24 demonstrates the corresponding increase in magnitude for positive strains when using the full 3D motion trajectories.

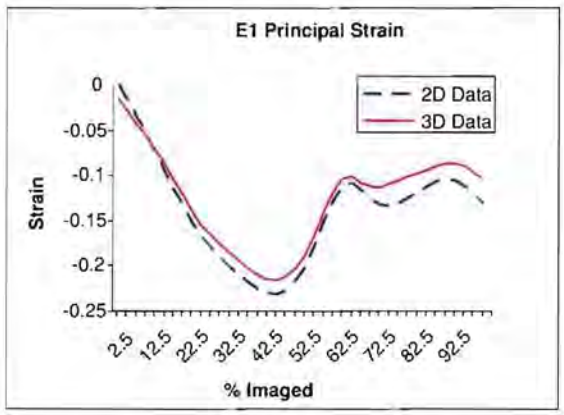

Figure 4.23: Strain time curves comparing computations based on 3D motion trajectories to those from 2D motion trajectories for the first principal strain in the posterior free wall.

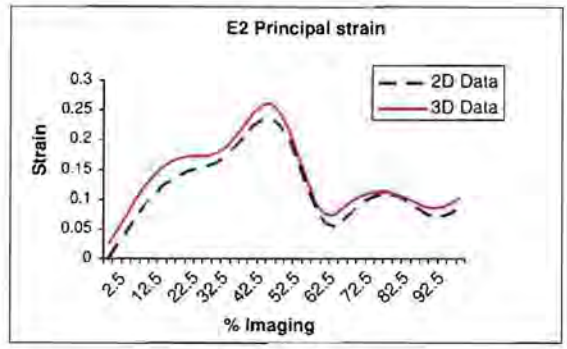

Figure 4.24: Strain time curves comparing computations based on 3D motion trajectories to those from 2D motion trajectories for the second principal strain in the posterior free wall.

4.3 Error quantification simulations

4.3.1 Measurements of inter-breathhold myocardial position variability for a healthy volunteer

Five two chamber and five four chamber long axis cine series of images were acquired over multiple breathholds. Figure 4.25A and B show the contours for the final cine image of each breathhold for the four chamber and two chamber views respectively.

In the four chamber view (Figure 4.25A), the maximum separation of the contours in the long axis direction at the base and apex is 3.4mm and 2.3mm respectively. The contours in this image group have a maximum midventricular separation of 3.4mm. The angle of the long axis to the horizontal axis for each image in the group is 51.45°, 50.98°, 51.22°, 48.58°, and 48.99°, respectively.

The contours and measurements for all the images in the two chamber long axis group of images are shown in Figure 4.25B. The maximum separation of the contours at the base and apex is 3.7mm. The maximum separation of contours in the short axis plane is 2.7mm and the five angles of the long axis to the horizontal are 34.67°, 35.36°, 35.71°, 35.71°, and 35.71°, respectively.

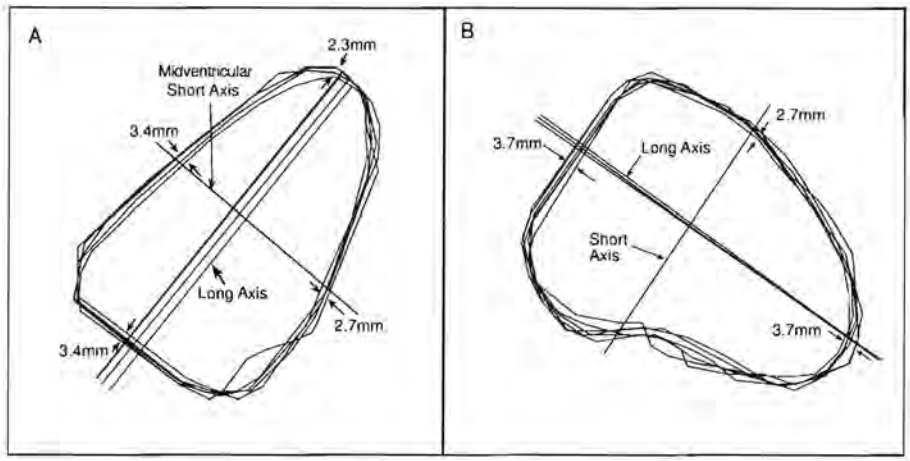

Figure 4.25: Contoured four chamber (A) and two chamber (B) long axis images showing the five overlapping contours for the final frames of each cine series.

4.3.2 Simulation to explore strain error resulting from inter-breathhold myocardial position variability

The results of the simulation provide an estimate of the error introduced into each individual component of the strain tensor as a result of variations in the position of the myocardium between breathholds. It follows from the results presented in the previous section that the standard deviation of the shift of the image plane in the long axis is 2mm and that the tilt of the image plane out of the short axis has standard deviation 1.5°. The error in each tensor component is dependent on the deformation. The errors are computed separately for each of the 12 strains used in the simulation. The error plotted is the root mean square (RMS) error computed for 500 repetitions of the simulation with each of the 12 input strains, where the input strain is scaled from 10% to 100% (in 10% increments) for every 500 repetitions.

In Figure 4.26 the strain error is plotted as a function of strain on a separate graph for each component of the strain tensor that is aligned to the RCL coordinate system. Each line corresponds to a different input strain. The largest RMS errors occur in the radial longitudinal shear strain with maximum amplitude 1.5% strain. The next largest RMS errors are in the circumferential longitudinal (Ecl) shear components with a maximum of

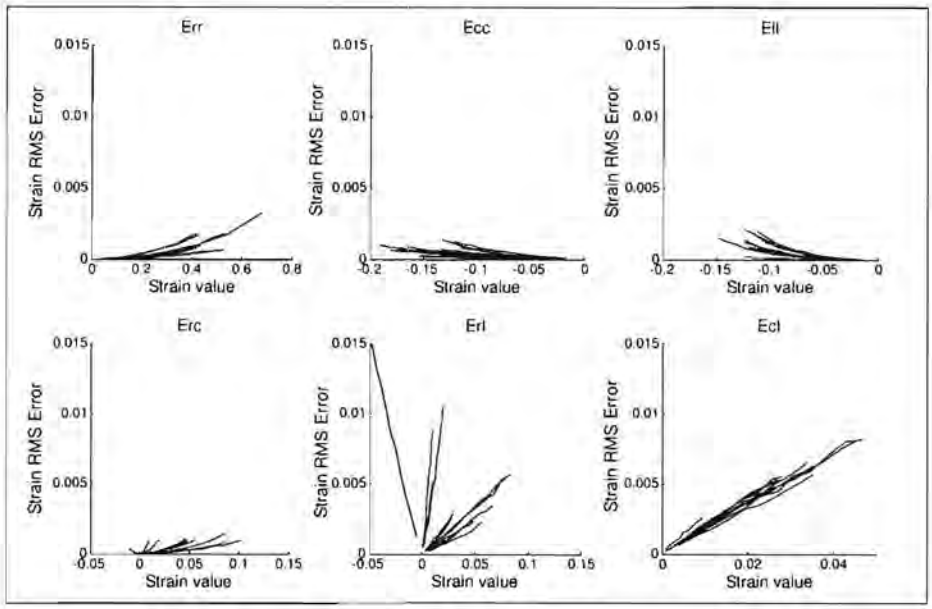

Figure 4.26: RMS errors plotted as a function of strain for the simulation to explore the effects of variability in the myocardial position between breath-holds. The error for each of the 12 input strain values is plotted on a separate line for each strain component in the RCL system. Err is the radial normal strain, Ecc the circumferential, Ell the longitudinal, Erc the radial circumferential shear strain, Erl the radial longitudinal shear strain, and Ecl is the circumferential longitudinal shear strain.

0.82% strain. The RMS errors of the remaining components of the strain tensor are all negligible with values less than 0.5% strain.

This simulation was repeated using 3D DENSE (DENSE encoded in 3 orthogonal directions) to compute strains. The data are plotted in Figure 4.27. The RMS error for longitudinal strain reaches a maximum of 4% strain. The shear strain components have the same RMS errors found in the previous simulation (maximum 1.5% for radial longitudinal, maximum 0.82% for the circumferential longitudinal, and less than 0.5% for radial circumferential shear strain). The radial and circumferential normal strains again have RMS errors of less than 0.5%.

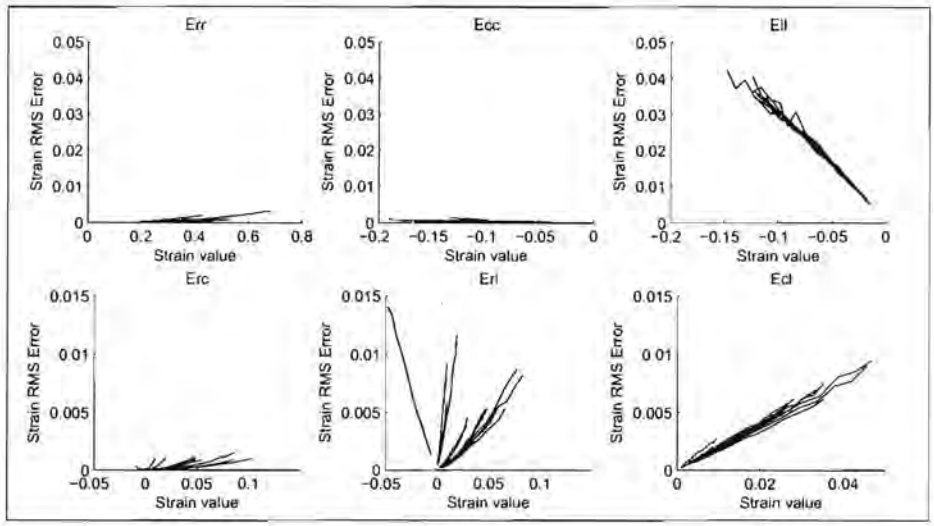

Figure 4.27: RMS errors plotted as a function of strain to explore the effects of variability in the myocardial position between breathholds. 3D strain was calculated using 3D DENSE displacement. The error for each of the 12 input strain values is plotted on a separate line for each strain component in the RCL system.

4.3.3 Simulation to explore strain error resulting from kinematic measurement noise

The first step in calculating the error introduced in the 3D strain tensor due to measurement noise was to calculate the noise introduced into a CSPAMM cine-DENSE measurement. The intramyocardial differential displacement noise introduced into a CSPAMM cine-DENSE measure is plotted as a standard deviation of noise as a function of the cine frame number in Figure 4.28. In this figure frame 15 corresponds to end systole with a noise standard deviation of 0.23mm.

This result was used in the simulation. In this simulation the RMS strain error for each 500 repetitions is plotted against strain magnitude and each component of the tensor was plotted on a separate scatter plot in Figure 4.29. The greatest error is introduced into the radial strain component with RMS errors of over 20% at a radial strain of 40%. The longitudinal normal strain has the least error introduced with a maximum error of less than 1.6% strain. The radial circumferential shear strain has RMS strain errors in the range of 6% to 10% and is the largest error for the shear strain components.

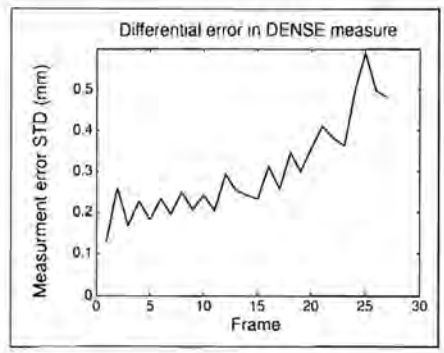

Figure 4.28: Standard deviation of error for the average difference between the displacement of a voxel and that of its two neighbours in the encoding direction.

The circumferential and longitudinal normal strains are plotted again in Figure 4.30 with adjusted axes limits to show that the magnitude of the strain error varies inversely with the magnitude of the strain. However, this is not the case in the positive (radial) strain where there is a direct relationship between the magnitude of the strain and the RMS error.

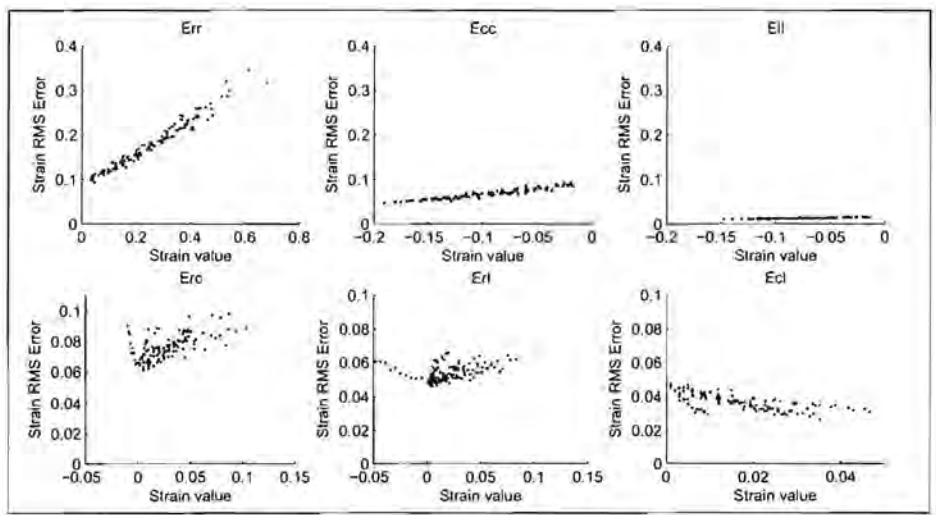

Figure 4.29: Scatter plots of RMS strain errors resulting from noise in DENSE and SENC measures. The RMS error is calculated for values ranging from 10% to 100%, in increments of 10%, for each of the 12 strains that were used in the simulation.

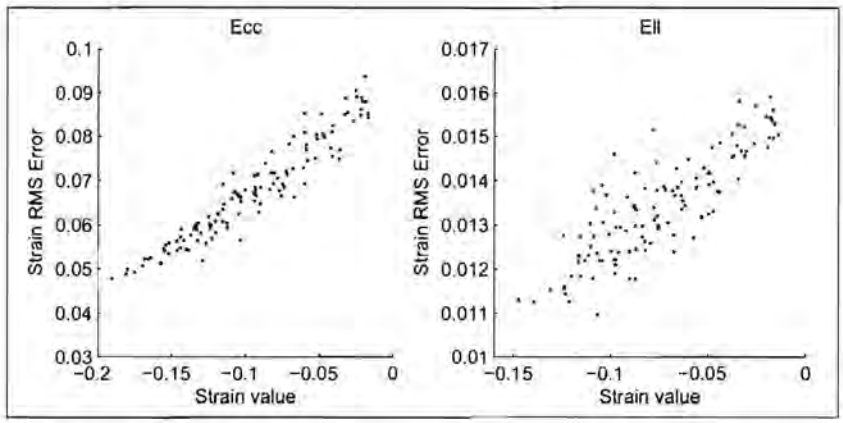

Figure 4.30: Ecc and Ell replotted with different axes limits. These graphs depict the simulated RMS error for these components of the strain tensor as a result of measurement error in the DENSE and SENC measurements and demonstrate the inverse relationship between negative strain magnitude and RMS error.

The effects of SENC noise alone were explored by repeating the simulation but with all the cine-DENSE noise set to zero. The results are plotted in Figure 4.31. The RMS error of all the tensor components is significantly reduced, except for the longitudinal strain. Notably the radial RMS error is now in the range of 0.5% to 2% strain and the circumferential strain RMS error is below 1%. The radial circumferential shear strain has an RMS error less than 1%.

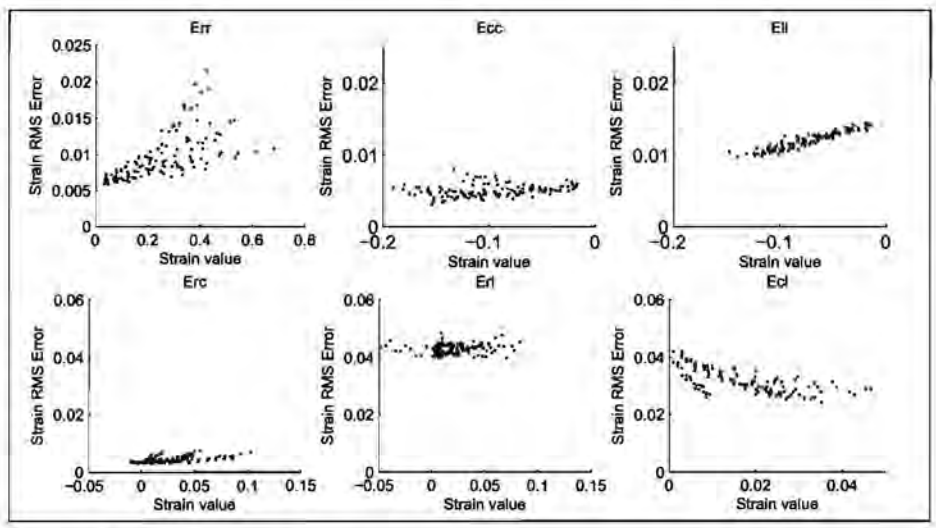

Figure 4.31: Simulated RMS error due to kinematic noise from SENC measures only.

Chapter 5

Discussion and Recommendations

As the simulations provide insight into the results of strain calculation in the volunteers, the results of the simulations are discussed first. Following the discussion on the simulation are discussions on the kinematic measurement techniques, the cine-DENSE and cine-SENC 3D strain calculations and trajectory based strain calculations. The chapter concludes with general limitations and makes recommendations for the future.

5.1 Simulations of strain computation

Simulations were performed to investigate the accuracy of the strain calculation technique. The two primary sources of error that were identified are inter-breathhold myocardial position variability and noise in the kinematic measurement. The simulations show that the error due to kinematic measurement noise is roughly five times larger than that due to variations in the position of the myocardium between breathholds for all components other than the longitudinal strain.

The simulations exploring the effects of noise in the kinematic measurement indicated that all the components of the strain tensor, except longitudinal normal strain, have significant errors that at times are of the order of the expected strain magnitude (the shear components and the radial normal strain). The longitudinal strain has an error less than 1.6% RMS strain. By repeating the simulation with the expected cine-DENSE noise set to

zero, cine-DENSE was identified as the predominant source of error for the radial and circumferential components of the normal strain and the radial circumferential shear strain. Cine-SENC was identified as the predominant source of error for the longitudinal shear components and longitudinal normal strain. The longitudinal normal strain error is significantly less than that of the other components due to the fact that this measure predominantly arises from the SENC estimation of through plane tag frequency, which boast a very small RMS error (1.5%). This results from the fact that this measurement depends on the image magnitude rather than the stimulated echo phase.

Interestingly, the simulation showed that the kinematic measurement error for negative strain is inversely proportional to the magnitude of the strain, and proportional to strain magnitude for positive strains. This results from Lagrangian strains being calculated from Eulerian data. Consider, for example, the simple formula for linear normal strain

$$E = \frac{|\overrightarrow{l}_t|}{|\overrightarrow{l}_0|} - 1 \tag{5.1}$$

in which $\overrightarrow{l_0}$ is a vector along the axis at the reference time and $\overrightarrow{l_t}$ is the same vector at the imaging time. For strains (E), calculated from Eulerian data, the measured variable containing a measurement error is $\overrightarrow{l_0}$. The more negative the strain the larger $\overrightarrow{l_0}$ becomes, thus reducing the significance of the error. The opposite is true for positive strains. Since the radial strain has the largest positive magnitude of all the strain components its associated RMS error is the largest and most significant.

The kinematic simulation technique produces an over estimate of the in plane radial and circumferential strain errors. This results from these components of strain being calculated from one cine-DENSE measurement plane in the simulation, whereas these were computed from the average deformation of two cine-DENSE imaging planes in the actual strain calculation. Furthermore, the error introduced into the deformation gradient for cine-DENSE is an over estimate as in the differential displacement error calculation the error is as a result of two CSPAMM measures whereas phase errors arise from the phase reference and a single CSPAMM in a typical cine-DENSE acquisition, where the phase reference is expected to have less phase noise due to its magnitude being significantly larger.

The error introduced into the through plane SENC measure is an under estimate as the technique reported by Osman *et al* (2001) was a single phase acquisition method. Increasing this expected error will affect the normal strain in the longitudinal direction.

Errors arising from variations in the position of the myocardium between breathholds are lower than those resulting from noise in the kinematic measurements. Using DENSE alone to calculate a full 3D strain tensor yields the largest error for the longitudinal components as a result of respiratory misalignment. Combining DENSE and SENC reduces the error in the longitudinal normal strain but offers no improvement for longitudinal shear strains. It should be noted, however, that data for the variability in the myocardial position between breathholds was acquired for only a single volunteer, thus a comprehensive picture of myocardial motion between breathholds cannot be formulated.

The simulation of strain calculated using 3D DENSE data shows significant errors for longitudinal tensor components. These result from the deformation gradient components $F_{1,3}$, $F_{2,3}$ and $F_{3,3}$ (the third column of F) being derived from the differences in displacement between voxels in two image planes that were measured in different breathholds. The errors are not only affected by the tilt of the image planes but also by the fact that the points used to measure the differences in displacement may not be separated by the expected amount, as the two image planes may have shifted closer together or further apart due to variations in position between breathholds. This error is, however, limited by the large separation of the two DENSE measurement planes (8mm). A larger separation results in these errors becoming less significant as the difference in displacement increases. The same reasoning applies for the error in the longitudinal shear strains for the technique that proposes a combination of DENSE and SENC MRI. In this case $F_{1,3}$ and $F_{2,3}$ are calculated using the difference in displacement between the higher and lower DENSE image planes.

The simulations show that the magnitude of the error is proportional to the magnitude of the strain, which is different to the relationship for kinematic measurement errors. The simulation did not account for shifts of the myocardium within the image plane but assumed that these, if present, were corrected by some form of cross-correlation between the images. A cross-correlation would, however, only solve misalignment errors due to translation and not changes in the rotation or shape of the myocardium. These rota-

tions or changes in shape of the myocardium are not expected to be large enough to have a significant effect on the calculation of strain.

The simulations performed demonstrate that the errors in the strain tensor depend on the particular myocardial deformation, as highlighted by the fact that different deformation gradients yield different RMS errors. The 12 deformation gradients used are sufficient to explain the effects of the range of deformations expected in the heart. The simulations assumed that the imaging axes were the radial, circumferential and longitudinal axes, which they are not. For the actual imaging axes larger shear strains are expected as these axes are not generally aligned with the principal strain directions. Furthermore, the large radial strain will not typically be aligned to an imaging axis, resulting in a reduced magnitude of the positive strain in each axis and therefore also a reduction in the effects of its error.

Since these simulations were not performed in the imaging coordinate system, they have only investigated the noise levels in the radial circumferential, radial longitudinal, and circumferential longitudinal shear strains, whereas the shear strains measured will be between the imaging axes. This is of particular importance where the radial and circumferential axes do not line up with the imaging axes as larger shear strains will be measured between the imaging axes. These large shear strains can be observed in the plots of the deforming cubes as they become significantly diamond shaped within the image plane where these two coordinate systems do not line up. The most vulnerable shear strains are the small through plane shear strains that have magnitudes similar to those in the radial, circumferential and longitudinal coordinate system due to the fact that the longitudinal axis lines up with the through plane axis. The small magnitude of these shear strains in the imaging coordinate system is demonstrated in the plots of the deforming cubes that do not become significantly diamond shaped along these axes.

5.2 Discussion of kinematic measurement techniques

The two techniques that were used to perform kinematic measurements were strain- and displacement encoded MRI (SENC and DENSE, respectively). In this discussion I will focus on the strain encoded MRI technique as its sequence development and tuning was central to this thesis. Cine-SENC parameters were optimized using a phantom and human volunteer data. The frequency profiles of slices for different slice thicknesses were explored

using several different unencoding frequencies. These phantom experiments demonstrate that the width of the frequency profile is inversely proportional to the slice thickness, as would be expected from the Fourier transform relationship.

The frequency profiles of the phantom are symmetric - a necessary requirement for a centre of mass estimation. It was found that the shape of the frequency profile is different for different cine phases indicating that different SENC linear correction parameters are appropriate for different cine phases.

For unencoding frequencies greater than 0.115cyc/mm the contribution to the signal from the unmodulated T1 echo centred about $k_z = 0$ is zero. Therefore, no interference will be present for the unencoding frequency of 0.15cyc/mm that was used in the SENC protocol.

Volunteer imaging demonstrated that the myocardium fades from the image too fast for an encoding frequency of 0.4cyc/mm to be realised. In order to reduce the rate at which the myocardium fades from the images, the width of the frequency profile could be increased or the encoding frequency reduced. However increasing the width of the frequency profile would reduce the slice thickness to a value less than 8mm, which impacts directly on the SNR of the images. A smaller encoding frequency was therefore preferred. The encoding frequency was reduced to 0.15cyc/mm, for which a slice thickness of 16mm could be used. A tradeoff exists for SENC imaging between a high encoding frequency and a large slice thickness as a high encoding frequency provides a higher sensitivity to strain while a large slice thickness affords an improvement in SNR but requires a lower encoding frequency.

In all the images for which the EPI echo train length (ETL) was double the number of segments a significant myocardial ghost appears along the phase encode direction near the edge of the image. For lower encoding frequencies of 0.15cyc/mm the ghosting usually only appeared in the first three cine frames. At higher encoding frequencies multiple ghosts appeared spread out along the phase encode direction. This ghosting may result from through through plane myocardial motion that could produce significant changes in the image, resulting in phase encode errors.

Ghosting can cause a significant measurement error in SENC as it relies on changes in myocardial signal magnitude and ghosting effectively reduces regional myocardial signal. The EPI parameters that produce the fewest artefacts are an ETL of 9 with 9 segments. Since this configuration halves

the number of segments per heartbeat, the number of heartbeats required to generate the image is doubled. Therefore, only two images can be acquired in a single breathhold. One could choose to acquire two SENC encoded images in one breathhold without a phase reference image. Care should be taken, however, to double the repetition time (TR) from that used for the DENSE acquisitions that use a 9(18) EPI configuration in order to match the cine image timings. Alternatively the SENC measurement could be performed over two breathholds, each with a phase reference and one encoded image. For this project fewer breathholds were preferred and a phase reference image deemed necessary, whereas the presence of artefacts was not critical. For these reasons a 9(18) ETL-segment combination was used.

The protocol chosen for cine-SENC used an encoding frequency of 0.15cyc/mm and unencoding frequencies of 0.15cyc/mm and 0.185cyc/mm. The primary reason for this encoding frequency was to enable a slice thickness of 16mm for optimal SNR. Although a slice thickness of 16mm is large, it is justified in view of the fact that two adjacent 8mm planes of cine-DENSE are acquired. Volunteer scanning shows that this combination of slice thickness and encoding is appropriate as the myocardium dephases but does not completely disappear from the image when unencoded at a frequency of 0.15cyc/mm. The value 0.185cyc/mm for the second unencoding frequency was based on the assumption that the Eulerian longitudinal strain is not expected to exceed 19%. Eulerian longitudinal strain is given by (Osman *et al* 2001)

$$E_E = \frac{W}{\sqrt{\omega^2 + v^2}} - 1 \tag{5.2}$$

where W is the encoding frequency, v is the through plane tag frequency at the imaging time, and ω is the in plane component of tag frequency at the imaging time. A strain of 19% corresponds to a tag frequency of 0.185cyc/mm.

A larger readout FOV was used for cine-SENC than cine-DENSE in order to improve the SNR of the images due to larger voxel/pixel sizes. By performing a bilinear interpolation the pixel sizes are artificially reduced to match those of the cine-DENSE data. It should be noted, however, that this does not improve the actual resolution of the data. At myocardial boundaries bilinear interpolation interpolates phase and magnitude data from both myocardial and non-myocardial signal which introduces errors. This problem can be limited by using conservative myocardial contours and ensuring that

cine-SENC voxels for which this would occur are not included in the myocardium.

A limitation of the SENC method in computing the through plane frequency is that frequencies above and below the two unencoding values saturate the measurement. This can be overcome in a number of ways, firstly by reducing the encoding frequency such that the frequency shift is reduced, however this reduces the sensitivity of the measure. Another option is to reduce the slice thickness which will increase the width of the frequency profile and thus allow the separation of the two unencoding frequencies to be increased. This results in an increase in the range of measurable frequencies at the cost of SNR. Finally, an extra unencoding frequency could be measured that will effectively double the frequency range without any loss in sensitivity or SNR at the cost of scan time or the phase reference image.

SENC estimates the through plane tagging frequency of myocardial tissue using a centre of mass estimate of the signal magnitude for two different unencoding frequencies. This centre of mass estimate requires a linear correction. This linear correction factor depends on the frequency profile of the slice and is therefore variable as this profile changes. For the results shown the magnitude of the complex signal was used in the centre of mass estimate whereas Osman *et al* (2001) used the real component of the complex signal. The difference between the magnitude and the real component of the signal is shown in Figure 5.1. Since the real component assumes negative values a wider range of frequencies can be measured. Figure 5.2 shows that using the real component does not alter the shape and width of the complex frequency profile in successive cine frames but only reduces its amplitude as is also observed in the magnitude profile. One disadvantage of using the real component of the profile is that since the phase of the myocardium is continually changing due to displacement and inhomogeneities, the real and imaginary contributions to the frequency profile are continually changing and the profile may at times lie entirely in the imaginary domain. At positions where the magnitude of the signal is low the phase quality of the image is also generally poor. As a result the magnitude of the signal rather than the real component was used to compute an estimate of the frequency peak.

It is evident in Figure 5.1 that two positive side lobes occur beside each of the first two minima for the frequency profile of the signal magnitude, so that the signal for unencoding frequencies that lie outside the profile can still be positive (unless they are zero). For such unencoding frequencies the COM estimate will incorrectly be computed at a value in between the

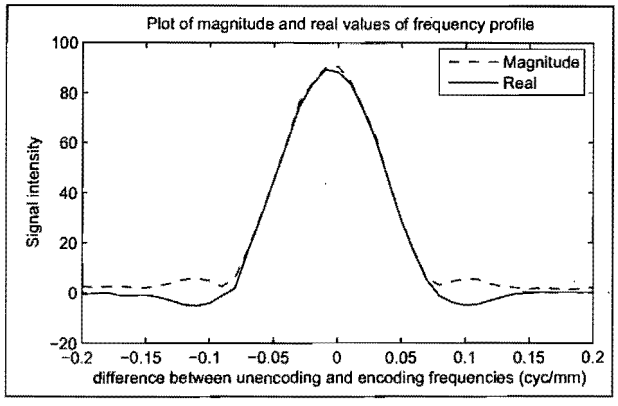

Figure 5.1: Frequency profile for the magnitude and real component of the signal for an 8mm slice encoded at 0.4cyc/mm.

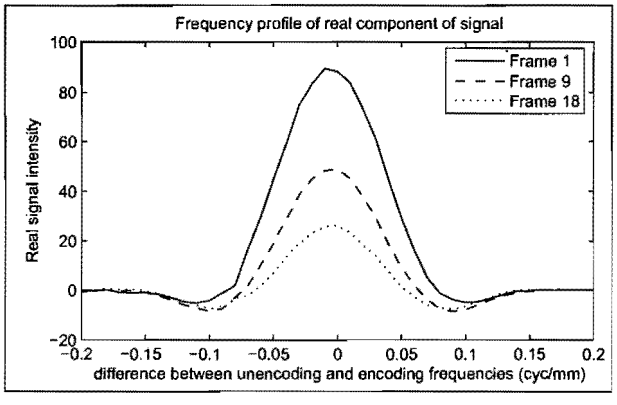

Figure 5.2: Frequency profile for the real component of the signal for frames 1, 9 and 18.

two unencoding frequencies as opposed to simply saturating at the encoding frequency nearer the actual tissue frequency as would occur when the real profile is used. This is not a serious problem as large tag frequencies are not expected.

The slice profile is clean and symmetric in the phantom, whereas in the myocardium this is not necessarily the case due to the fact that the imaging characteristics of the myocardium may change over the large 16mm slice. This will not affect the estimate of the through plane tag frequency that is based on the magnitude of the images.

It is evident from the differential displacement measurements that the cine-DENSE phase measurements are very noisy. This is attributed to a number of different reasons, amongst them firstly, the differences in the imaging method and acquisition time for the phase reference image compared to the encoded images. The phase reference image is a normal SPAMM image with zero tag encoding so that its phase arises from all three echoes (stimulated, T1 and complex conjugate echoes). Secondly, the low signal strength of the stimulated echo that decreases exponentially over time, and increasing phase noise due to spin-spin dephasing.

5.3 Strain calculation and display

The colour maps of the three-dimensional intramyocardial Lagrangian strains demonstrate distinct patterns for normal (radial, circumferential and longitudinal) Lagrangian strain. The smoothness and uniformity of the strain calculation for the circumferential and longitudinal strains demonstrate good robustness against noise. The average end systolic circumferential strains found in all the volunteers are in good agreement with the results of Moore *et al* (2000) as all the average strain values lying within two standard deviations of the mean end systolic circumferential strain reported. The calculated standard deviation of the circumferential strain (0.07 for volunteer 3) demonstrates that the noise levels are lower than the strain magnitude and lower than those predicted in the simulations.

The average longitudinal strain is less than the reported value ($p < 0.0017$). The reported value is of the order of -0.16 with a standard deviation of the order of 0.03 between volunteers (Moore *et al* 2000) whereas the average longitudinal strain measured in this study is -0.09. This low longitudinal

strain is likely to be as a result of an inappropriate choice of SENC COM linear error correction parameters. One set of linear correction parameters were optimised for all cine frames. It is evident from the phantom frequency slice profiles that parameters should be chosen and optimised individually for each cine frame.

The longitudinal strain is the least noisy measurement with each strain field demonstrating a standard deviation of 0.03 (except for volunteer 4 of 0.04) which is three times larger than the RMS error predicted by the kinematic measurement noise simulation. This is attributed to the kinematic noise in the SENC though plane frequency measure being under estimated. Despite this component of the tensor being the least noisy, it also has the smallest magnitude of the three normal strain components so that even this small noise contribution is significant.

The standard deviation of the radial strain at end systole is large, half the magnitude of the average radial strain reported by Bogaert and Rademakers (2001). This is evident in colour maps of radial strain where regions of the myocardium exhibit no strain and other regions have radial strains so large (> 0.4) that the colour map is saturated. The simulations predicted large errors for the radial strain. The average end-systolic radial strains all lie within one standard deviation of the mean reported by Moore *et al* (2000), however, they lie at the lower end of this range. The calculated standard deviation of radial strain in each strain field of the four volunteers matches the RMS error demonstrated in the simulations (they both demonstrate measures in the order of 0.2 strain).

The strain maps do not depict any distinct or circumferentially uniform transmural strain patterns as expected. This could be due to the fact that the myocardial contours were drawn particularly conservative in order to ensure that they contained only myocardium for all five acquisitions across breathholds. This applies to the two planes of cine-DENSE, where the lower DENSE plane that is closer to the apex will have a smaller radius and thus tighter contours. If these five sets of images are all contoured individually, sub-pixel resolution contour matching can be performed to account for in plane myocardial rotations and small changes in the shape of the myocardium. Less conservative contouring could then be applied.

In all four volunteers the longitudinal strain peaked two cine frames later in the posterior free wall (indicated with circles in Figure 5.3) than in the remainder of the myocardium and all other normal strain components (Figure

5.3). In volunteer four this delay occurred in a larger region and appeared as a general delay in the onset of longitudinal contraction for the affected region. No previously published data could be found that described this phenomenon, it could, however, be due to the nature of the motion in the myocardium.

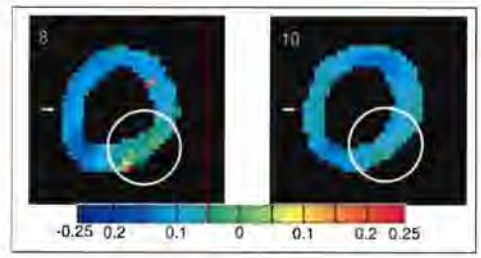

Figure 5.3: Longitudinal strain for frames 8 and 10 for volunteer 3. A circle highlights the area of delayed peak strain; the strain peaks for all segments except the highlighted region in frame 8.

The radial circumferential and longitudinal shear strains display temporal and spatial patterns indicating that these strains are not governed by noise. As there was no obvious continuity or pattern observed for the longitudinal shear strains between volunteers, their accuracy and general behaviour could not be determined from these measures.

The principal strain maps at end systole exhibit two characteristics for all volunteers. Firstly, the positive (third principal) strain is radially oriented within the image plane with average peak values in agreement with the findings of Moore *et al* (2000). Secondly, the first (most negative) principal strain spirals clockwise from the apex to the base when viewed from the base, as reported by Moore *et al* (2000). At positions where the first and second principal strains have similar magnitude their directions may be swapped due to the fact that they are sorted by magnitude. The continuity of the principal strain directions can be used as a measure of shear strain accuracy (shears in the imaging coordinate system)

The continuity, smoothness and expected patterns of the principal strains can be used to infer the accuracy of the complete strain tensor. The directions of the principal strains are not perfectly continuous due to inaccuracies in the calculation of the shear strains. It was shown previously in the section describing the simulations that the noise is most significant for these small strains. The fact that the principal strain directions do, however, correspond

to predicted patterns lend credibility to the shear strain measurements. It should be noted that the principal strains are less noisy than the radial and circumferential strain components and display smoother, more continuous colour maps.

The deforming cubes display in a single image the deformation gradient field. If a deformed cube is described by three orthogonal vectors joining its vertices, these vectors correspond to the three vectors of the deformation gradient so that one can observe directly how each imaging axis interacts with the other axes. Although this technique is essentially a glyph technique, it differs from the other techniques in that it is not aligned to the principal strain directions. As mentioned previously, the degree to which each of the three orthogonal faces deform to a diamond shape is an indication of the magnitude of the components of the shear strain. Shear strain is present when two vectors that were originally orthogonal (ie. aligned along the strain axes) deform in such a way that they are no longer orthogonal at the measurement time. When a face of the cube becomes diamond shaped two such axes are no longer orthogonal.

The thinness of the cubes in the through plane direction provides a measure of the linear longitudinal normal strain. If the deforming cubes (that are aligned to the imaging coordinate system) are aligned with the radial and circumferential directions, the face of the cubes in the image plane will become rectangular due to stretching in the radial direction and contraction in the circumferential direction. However, when the cubes are not aligned with the radial and circumferential axes they will become diagonally thicker and thinner in the radial and circumferential directions, respectively. In view of this, it is preferable to align the axes of the cubes to the radial, circumferential and longitudinal directions in order that the normal and shear strains can be clearly depicted. These cubes depict linear deformation (not squared as in the Lagrangian approach). An alternative approach is to deform spheres using the deformation gradient since spheres are not influenced by a particular coordinate system and would stretch in the directions of principal stretch and contract in the principal directions of contraction. These techniques are able to display an uncluttered representation of the deformation, with less obvious irregularities and discontinuities due to noise. The major drawback, however, of these methods is that the cubes (or spheres) initially have unit size and that the strain is depicted by the change in size of the cubes (or spheres). Thus it is not easy to gauge the strain magnitude using such a technique.

Superquadratic glyphs depict the relationships between the magnitudes of the principal strains by the sharpness of the corners between the principal strain directions. If two strain values have identical magnitudes (transversely isotropic) the shape becomes continuous (a circle) in the plane formed by these two principal strain directions. These features are clearly shown in the glyph images rendered. Due to the glyphs being scaled to the magnitude of the principal strain, the subtleties of the glyph corners are, however, outweighed by the distinct differences in the glyph lengths along the directions of principal strain. The third (most positive) principal strain tends to clutter the images by its large noisy magnitude, drawing attention to this component while disrupting the information depicted in the other two principal strains components. This visual clutter from the large magnitude of the positive radial strain can be reduced by converting the principal strains to linear strain values. This will have the effect of reducing the magnitude of the positive strain and increasing the magnitude of the negative strains, thus drawing less attention to the large and noisy positive (radially oriented) principal strain. Figure 5.4 demonstrates the effect of linearising the principal strain values.

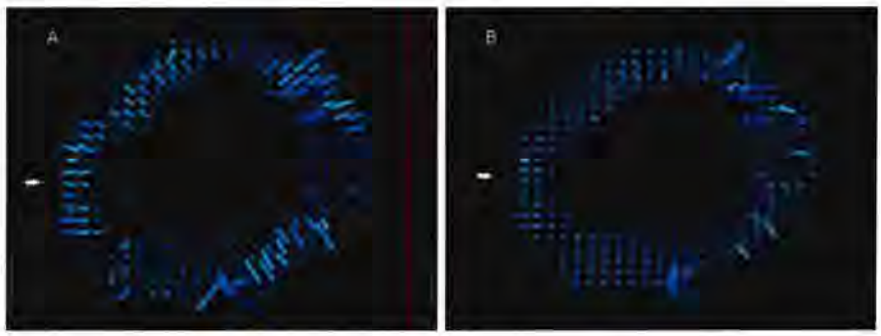

Figure 5.4: A. Glyph image of volunteer 3 without linearising the principal strains. B. Glyph image with the principal strains linearised.

The glyphs clearly depict the absence of strain at the start of the cardiac cycle (glyphs have practically no size), the increase in strain through the onset of systole (glyphs grow), and the return to low strain at mid diastole (glyphs get smaller again). The scattering of variable sized glyphs in the final frames of the cardiac cycle indicates the presence of increased noise. The strain magnitude is directly related to the size of the glyph and the magnitude of the first principal strain is mapped onto the colour of the glyph.

5.4 Trajectory based calculation of 2D and 3D strain

Two methods were presented to calculate strain using motion trajectories computed from cine-DENSE, one calculated 2D strain and the other 3D strain. The method presented for calculating 3D strain using cine-DENSE 3D motion trajectories suffered significant error in the longitudinal normal strain component yielding positive rather than negative strains. An error in the longitudinal strain is expected due to the slice positions being shifted between breathholds. This results in the differential displacement data being calculated at erroneous plane separations. This slice separation (or position) error will have a larger effect on planes that have a small separation. For the data presented the separation between the imaging planes was 2.8mm. If the error in the separation of the planes is as large as 2mm (as observed in the long axis volunteer images), it is easy to comprehend that this will have a dramatic effect on the calculated results. It should be noted that in the simulation a separation of 8mm between planes was used resulting in the simulation having significantly less error due to myocardial position variability. Positive longitudinal strain could have resulted from the lower imaging plane being located above the higher imaging plane at the imaging time due to respiration.

The calculation of Lagrangian strain from motion trajectories allows the strain to be calculated at any desired point in time so that an arbitrarily high temporal resolution is achievable. The underlying resolution is, however, limited to the temporal resolution of the image. Lagrangian strain computed in this way can also be displayed on a Lagrangian myocardial map. The advantage of this display is the ability to view the temporal evolution of the deformation of each myocardial voxel on the first frame over the measurement duration. This was demonstrated in Figures 4.21 and 4.22.

It is interesting to note that the radial strains computed in this way are smaller with the colour map having a reduced limit of 0.3. This could be due to a reduction in noise from temporal smoothing and due to the Lagrangian nature of the trajectories. In the non-trajectory based strain calculation noise has an exponential effect on positive strains due to the Eulerian nature of the measurement and its error. A small error causing $\overrightarrow{l_0}$ to tend to zero, as may occur for positive strains, will result in positive strains increasing more than the reduction in positive strain caused by the same error magnitude causing $\overrightarrow{l_0}$ to tend away from zero. Normal Lagrangian strain E_l in the direction of $\overrightarrow{l_0}$ is given by:

$$E_l = \frac{1}{2}\left[\left(\frac{|\overrightarrow{l_t}|}{|\overrightarrow{l_0}|}\right)^2 - 1\right] \tag{5.3}$$

In Figure 5.5 the normal Lagrangian strain in the direction of $\overrightarrow{l_0}$ is plotted as a function of the error in the differential displacement $|\overrightarrow{l_0}|$. Negative errors tend to inflate the strain measurement more than positive errors will decrease the strain by. The error introduced in the Lagrangian strain from a Lagrangian measure (i.e. DENSE motion trajectories) is introduced into the $\overrightarrow{l_t}$ component and will not have the same effect as it is not in the denominator of the above expression, thus for this radial strain the strain error will not be weighted by errors causing an increased strain.

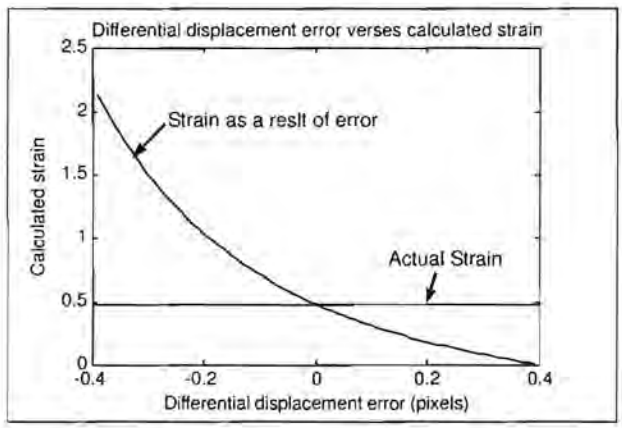

Figure 5.5: Plot of strain verses differential displacement error demonstrating the inflated effect on strain values resulting from negative errors.

Lastly, 2D strains were calculated using the DENSE motion trajectories. Strain time curves for the first and second principal strains for one segment of the myocardium were calculated for both 2D and 3D motion trajectory data. The first (negative) principal strain displayed a reduced magnitude when calculated from true 3D deformation data than when it was calculated from simplified 2D data. The effect is reversed for the second (positive) principal strain, ie. magnitude is increased when calculated from true 3D data. The reason for this is that the through plane motion is assumed to be uniform when the strain is calculated from 2D data. The third component of the vectors $\mathbf{V}'$ that are used in the formation of the deformation gradient F, are therefore assumed to be zero at the measurement time. This results in

an under estimate of the magnitude of $\mathbf{V}'$. Stretch (positive strain, ie. second principal strains) will therefore be under estimated, whereas shortening (negative strain, ie. first principal strains) will be over estimated.

5.5 General limitations and future recommendations

The first limitation of the proposed technique is that significant measurement noise is introduced as a result of both noise in the kinematic measurements and slice position variability between breathholds. The larger kinematic measurement noise arises particularly as a result of error introduced in the image phase. These errors increase over the cardiac cycle as the magnitude of the stimulated echo decreases. The slice position variability between breathholds has the most significant effect on the longitudinal shear strains, although the magnitude of this error has been reduced by separating the higher and lower DENSE imaging planes by 8mm.

The second limitation to this technique is that the strain is imaged over a very large slice thickness of 16mm, which may disguise pathology that does not span the entire slice. This large measurement slice also reduces the definition of the myocardial boundaries so that sub-endocardial and sub-epicardial strains cannot be clearly defined. Since this 16mm slice is an average of all the strains experienced within it, important or distinguishing strain patterns may go unnoticed if the slice does not experience the same strain patterns through its entire depth. The third limitation to the technique is the time required to image the entire 3D strain. Five separate breathholds are needed for each slice.

If this method was to be used to measure the full 3D strain tensor over the entire myocardium, only three extra breathholds will be required for each adjacent plane for which the strain will be computed. Essentially cine-DENSE data is acquired for a slice adjacent to either the lower or higher previous cine-DENSE imaging plane, with another cine-SENC acquisition spanning the new pair of adjacent planes, one being one of the previously imaged DENSE planes and the other the new adjacent slice. In this manner the adjacent planes of cine-DENSE data can be shared, thus reducing the total number of breathholds to image the entire myocardium from that if they were all imaged separately.

A possible way to address the problems associated with a 16mm measurement plane, the errors in the longitudinal shear strains, and the requirement of five breathholds to compute the 3D strain of one slice of the myocardium, is to acquire the cine-DENSE data for a single encoding direction for two adjacent slices either simultaneously or in the same breathhold. Reese *et al* (2002) proposed a method where they encoded two adjacent slices of myocardium in a single shot. Alternatively, this could be done by acquiring SPAMM cine-DENSE data for the two adjacent slices for encoding in a single direction which require only two phase reference and two encoded images (one for each slice) to be acquired in a single breathhold. If the temporal resolution of the method is reduced, it will be possible to accommodate this. By acquiring images for the two adjacent planes in this manner an 8mm cine-DENSE slice separation is not needed and can be reduced as the images will be acquired at the same time with a known slice separation, the cine-SENC acquisition can be optimized to allow a slice thickness less than 16mm.

An alternative method of measuring the full 3D strain over multiple breathholds is to use three non-coplanar cine-SENC measurements. If each cine-SENC acquisition was encoded in a direction offset by an angle from the normal to the imaging plane with in plane tag frequency components orientated at 0°, 120° and 240° in the imaging plane, the separation of multiple non-coplanar points can be understood and used in a strain measurement. Care should be taken to use encoding directions that have larger components through the image plane than in the image plane to minimize the intra voxel dephasing in the in plane direction. The method, however, would be sensitive to small errors in the measurement of tag plane orientation as there will not be a large angle between the three encoding directions, thus allowing small errors to have a large effect. Based on the errors of the CSPAMM cine-DENSE differential displacement measures, that have a higher accuracy than SENC, the required accuracy may not be achievable from the phase measures. The advantage of using such a technique is that the full tensor can be imaged in three breathholds, and if the cine-SENC is optimized for the best SNR, slice thicknesses less than 16mm can be imaged. This method will also not suffer from the errors associated with myocardial position variability between breathholds.

Chapter 6

Conclusion

This project described a method to measure the complete 3D strain tensor field in a single slice of myocardium over the cardiac cycle using a combination of cine-DENSE and cine-SENC measurement techniques. The development of a working strain encoded MRI sequence demonstrated its effectiveness in overcoming the problem of myocardial miss alignment across multiple breathholds and in reducing the total number of breathholds required as compared to what would be the case if such calculations were performed using DENSE alone.

Through the use of simulations it has been shown that the dominant source of error in these strain measurements originate from noise in the myocardial kinematic measurements. The visualisation of intramyocardial strains measured using this technique demonstrated consistent results in good agreement with expected measures.

The colour map visualisation demonstrated the time dependent variation of the radial, circumferential, and longitudinal normal and shear strains measured. The principal strain visualisation technique demonstrated the principal magnitudes and directions of myocardial deformation while the superquadratic glyph visualisation convention demonstrated the ability to view the entire tensor field in a single image. The deformation gradient visualisation using deforming cubes clearly and simply demonstrated the type of deformation present.

The calculation of strain from Lagrangian motion trajectories demonstrated the visualisation of strain on Lagrangian strain maps calculated at any desired time point over the imaged portion of the cardiac cycle. However, 3D

strain calculated from these cine-DENSE based trajectories in two adjacent planes did not provide accurate through plane strain.

In conclusion the ability to calculate 3D strain tensor fields in a singe slice of myocardium has been demonstrated.

Bibliography

Aletras AH. Ding S. Balaban RS and Wen H. (1999a). "DENSE: displacement encoding with stimulated echoes in cardiac functional MRI". *Journal of Magnetic Resonance.* Volume 137. Pages 247-252.

Aletras AH. Balaban RS. and Wen H. (1999b). "High-Resolution Strain Analysis of the Human Heart with Fast-DENSE". *Journal of Magnetic Resonance.* Volume 140(1). Pages 41-57.

Augenstein KF. and Young AA. (2001). "Finite Eliment Modeling for Three-Dimensional Motion Reconstruction and Analysis". In "Measurement of Cardiac Deformations from MRI: Physical and Mathematical Models". (Editors: Amini AA and Prince JL). Pages 37 - 58.

Axel L. and Dougherty L. (1989). "MR imaging of motion with spatial modulation of magnetisation". *Radiology.* Volume 171. Pages 841-845.

Bogaert J. and Rademakers F. (2001). "Regional nonuniformity of normal adult human left ventricle". *American journal of physiology. Heart and circulatory physiology.* Volume 280. pages H610-H620.

Bradshaw D. Groenewald P. Laubscher R. Nannan N. Nojilana B. Norman R. Pieterse D. and Schneider M. (2003) "Initial Burden of Disease Estimates for South Africa, 2000." *South African Medical Research Council*

Edvardsen T. Gerber BL. Garot J. Bluemke DA.

Lima JA. and Smiseth OA. (2002). "Quantitative assessment of intrinsic regional myocardial deformation by Doppler strain rate echocardiography in humans: validation against three-dimensional tagged magnetic resonance imaging." *Circulation* Volume 106(1). Pages 50-56.

Ennis DB. Kindlman G. Rodriguez I. Helm PA. and McVeigh ER. (2005). "Visualization of tensor fields using superquadric glyphs". *Magnetic Resonance in Medicine.* Volume 53(1). Pages 169-176.

Epstein FH. and Gilson WD. (2004). "Displacement-encoded cardiac MRI using cosine and sine modulation to eliminate (CANSEL) artifact-generating echoes". *Magnetic Resonance in Medicine.* Volume 52(4). Pages 774-781.

Fischer S. McKinnon G. Maier S. and Boesiger P. (1993). "Improved myocardial Tagging Contrast". *Magnetic Resonance in Medicine.* Volume 30. Pages 191-200.

Garot J. Lima J. Gerber B. Sampath S. Wu K. Bluemke D. Prince J. and Osman N. (2004). "Spatially Resolved Imaging of Myocardial Function with Strain-encoded MR: Comparison with Delayed Contrast-enhanced MR Imaging after Myocardial Infarction". *Radiology.* Volume 233. Pages 596-602.

Haacke EM. Brown RW. Thompson MR. Venkatesan R. (1999). "Magnetic resonance imaging. Physical Principles and Sequence Design". J. Wiley and Sons, New York, ISBN: 0-471-35128-8.

Hatle L. and Sutherland GR. (2000). "Regional myocardial function a new approach". *European Heart Journal.* Volume 21. Pages 1337 - 1357.

Kim D. Gilson WD. Kramer CM. and Epstein FH. (2004). "Myocardial Tissue Tracking with Two-dimensional Cine Displacement-encoded MR Imaging: Development and Initial Evaluation". *Radiology.* Volume 230. Pages 862-871.

Moore CC. Lugo-Olivieri CH. McVeigh ER. and

Zerhouni EA. (2000). "Three-dimensional systolic strain patterns in the normal human left ventricle: characterization with tagged MR imaging". *Radiology.* Volume 214(2). Pages 453-466.

Mosher TK. and Smith MB. (1990). "A DANTE tagging sequence for the evaluation of transitional sample motion". *Magnetic Resonance in Medicine.* Volume 15. Pages 334-339.

Nayler GL. Firmin DN. and Longmore DB. (1986). "Blood flow imaging by cine magnetic resonance". *Journal of computer assisted tomography.* Volume 10(5). Pages 715-722.

Netter FH. (1998). "Interactive Atlas of Human Anatomy". *ICON Learning Systems.* Version 2.0.

Osman NF. McVeigh ER. and Prince JL. (2000). "Imaging heart motion using harmonic phase MRI". *IEEE transactions on medical imaging.* Volume 19(3). Pages 186-202.

Osman NF. Sampath S. Atalar E. and Price J. (2001). "Imaging Longitudinal Cardiac Strain on Short-Axis Images Using Strain-Encoded MRI". *Magnetic Resonance in Medicine* . Volume 46. Pages 324-334.

Pan L. Prince JL. Lima JA. and Osman NF. (2005)."Fast tracking of cardiac motion using 3D-HARP". *IEEE transactions on biomedical Engineering.* Volume 52(8). Pages 1425-1435.

Parthasarathy V. and Prince JL. (2004). "Strain resolution from HARP-MRI". *In Proceedings of the 12th annual meeting of ISMRM, Kyoto, Japan, 2004 15-21 May*

Reese TG. Wedeen VJ. and Weisskoff RM. (1996). "Measuring Diffusion in the Presence of Material Strain". *Journal of magnetic resonance: B.* Volume 112(3). Pages 253-258.

Reese T. Feinberg D. Dou J. and Wedeen V.

(2002). "Phas Contrast MRI of Myocardial 3D strain by Encoding contiguous Slices in a Single Shot" *Magnetic Resonance in Medicine* . Volume 47. pages 665 - 676.

Sampath S, Derbyshire JA, Atalar E, Osman NF and Prince JL.(2003). "Real-time imaging of two-dimensional cardiac strain using a harmonic phase magnetic resonance imaging (HARP-MRI) pulse sequence". *Magnetic Resonance in Medicine.* Volume 50(1). Pages 154-163.

Spottiswoode BS. Zhong X. Meintjes EM., Mayosi BM. and Epstein FH. (2005a). "Phase Unwrapping for Absolute Cine-DENSE Myocardial Displacement Measurements using a 3D Guided Flood-Fill Algorithm." *Proceedings of 13th Annual Meeting of International Society for Magnetic Resonance in Medicine (ISMRM), Miami Beach, Florida, USA, 7-13 May 2005.*

Spottiswoode BS., Zhong X., Meintjes EM., Mayosi BM. and Epstein FH. (2005b). "Improved Myocardial Tissue Tracking and Strain Accuracy in Cine-DENSE using Temporal Fitting." *Proceedings of 13th Annual Meeting of International Society for Magnetic Resonance in Medicine (ISMRM), Miami Beach, Florida, USA, 7-13 May 2005.*

Stoylen A. Ingul CB. and Torp H. (2003). "Strain and strain rate parametric imaging. A new method for post processing to 3-/4-dimensional images from three standard apical planes. Preliminary data on feasibility, artefact and regional dyssynergy visualization". *Cardiovascular Ultrasound.* Volume 1. Pages 1 - 11.

Voigt J. and Flachskampf F. (2004). "Strain and strain rate". *Zeitschrift fr Kardiologie.* Volume 93. Pages 249 - 258.

Wunsche B. Lobb R. and Young A. (2004). "The Visualization of Myocardial Strain for the Improved Analysis of Cardiac Mechanics". *In Proceedings of the 2nd international conference on Computer graphics and interactive techniques in Australasia and South East Asia.* Pages 90-99.

Yoshida T. Mori M. Nimura Y. Hikita G. Taka Gishi S. Nakanishi K. and Satomura S. (1961). "Analysis of heart motion with ultrasonic Doppler method and its clinical application". *American Heart journal.* Volume 61. Pages 61-75.

Zerhouni EA, Parish DM, Rogers WJ, Yang A and Shapiro EP. (1988). "Human heart: tagging with MR imaging–a method for noninvasive assessment of myocardial motion". *Radiology.* Volume 169(1). Pages 59-63.

Zwanenburg J, Gtte M, Kuijer J, Heethaar R, van Rossum A and Marcus J. (2004). "Timing of cardiac contraction in humans mapped by high-temporal-resolution MRI tagging: early onset and late peak of shortening in lateral wall". *American journal of physiology. Heart and circulatory physiology.* Volume 286. Pages H1872 H1880.

Images Obtained from: 3D heart image, Internet URL:
http://www.joelertola.com/tutorials/heart/img/heart.jpg.